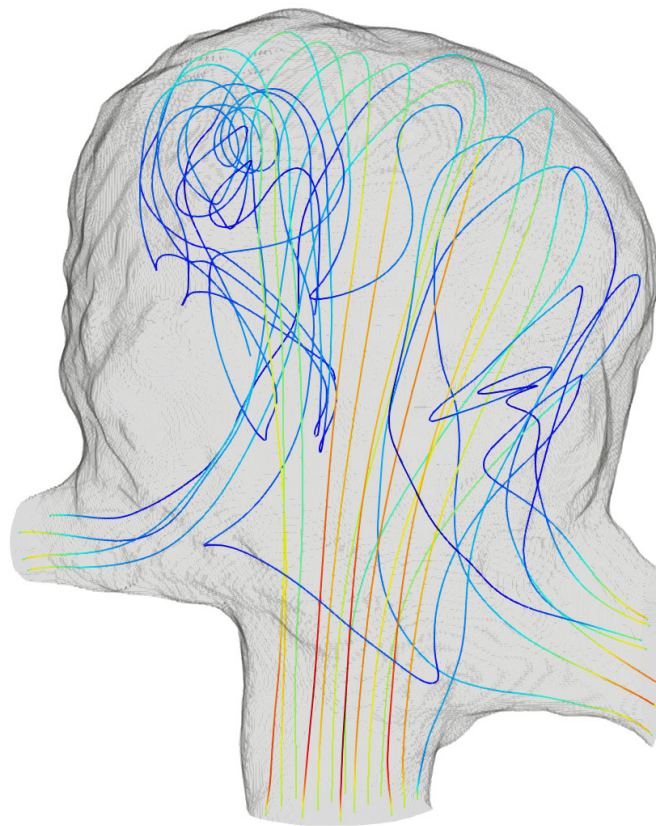


# COMPUTATIONAL ANALYSIS OF FLUID DYNAMICS IN INTRACRANIAL ANEURYSMS

DIEUWERTJE ALBLAS

*FEBRUARY 2021*



Faculty of Electrical Engineering, Mathematics and Computer Science (EEMCS)  
Master Thesis Applied Mathematics

Chair: Multiscale Modelling and Simulation  
University of Twente

*Assessment committee*  
Prof. Dr. Ir. B.J. Geurts (Supervisor)  
Dr. F.L. Schwenninger  
Dr. J.M. Wolterink



# Abstract

Successful treatment of so-called bifurcation aneurysms is a persisting challenge. Due to the complex geometries of such aneurysms, blood flow follows intricate paths inside the aneurysm sac, which need to be rectified for a successful treatment. In this study, we present a method that involves computational fluid dynamics, resulting in a multi-layered assessment, aiming to assist the neurosurgeon in finding suitable treatment options for a particular patient. We cover two central aspects: (1) how to obtain realistic, patient specific flow prediction and (2) how to translate the comprehensive information contained in the simulation results to a concise and clinically relevant form, incorporating the main characteristics of the flow.

Realistic flow simulations through aneurysm geometries rely on patient-specific medical image data and require numerical approximations. The resulting velocity fields under physiological conditions, acquired using OpenFOAM software, showed clear spatial convergence using on the order of 20-40 grid cells per diameter of the inflow vessel. To enhance the information contained in the flow fields, we propose a new assessment method in which we determine the dispersion of a numerical bolus during the pulsatile flow. Effects of potential treatment, as well as changes in the geometry configuration were captured and quantified by this method, giving confidence that this method is a first step towards numerical decision support for optimal treatment of intracranial aneurysms.

# Preface

Before you lies the report 'Computational Analysis of Fluid Dynamics in Intracranial Aneurysms'. It has been written by me, in order to obtain my master's degree in Applied Mathematics at the University of Twente. This project has taken place from April 2020, to January 2021. I will remember this period as a special one, that demanded a lot of flexibility from everyone involved. Physical meetings were not possible most of the time, and the majority of the research was conducted from the 'comfort of my own home'.

This project has been a unique opportunity for me to apply my mathematical skills on a medical related topic, something that I have always been interested in. The topic itself is quite involved, since the process of aneurysm development and rupture is influenced by many factors. For most of these factors, their exact contribution remains unknown, which is why mathematical modelling and simulation can provide new insights to help medical experts in forming their decisions. Special thanks in this process go out to my supervisor, Bernard Geurts. Our discussions always helped me get back on track and never failed to spark my enthusiasm. Also his optimism throughout the process really helped me get the best out of this project. I also want to thank Julia Mikhal, both for taking the time to prepare the geometries for simulation, as well as the friendly contact via e-mail and Skype. It is a pity we never got to meet in person. Moreover, I want to thank Jeroen Boogaarts, neurosurgeon at Radboud UMC in Nijmegen, for his cooperation. After our meetings, I felt encouraged to continue my research.

Upon finalizing this report, my time as a student at the University of Twente comes to an end. I can look back on five amazing years, accompanied by many new friends. In particular I want to thank Pascal, Mariya, Nico, David, Lotte, Maaïke and Steven for their friendship and all the fun times we had together. Also to my roommates: Rubz, Grilltie, Goobz, Rosa, Ap, Anne, Don and JP: thank you for forming a home for me over the previous years. Last but definitely not least, I want to thank my parents, brother and boyfriend for always being there for me and supporting me throughout my studies. Without all of you, my time as a student would not have been the same.



# Contents

<b>1</b>	<b>Introduction and clinical motivation</b>	<b>5</b>
<b>2</b>	<b>Mathematical model</b>	<b>7</b>
2.1	Pathology and treatment . . . . .	7
2.2	Geometry . . . . .	9
2.3	Navier-Stokes and boundary conditions . . . . .	11
<b>3</b>	<b>Flow prediction in intracranial aneurysms</b>	<b>15</b>
3.1	Immersed boundary method and OpenFOAM . . . . .	15
3.2	Steady flow in aneurysm geometries . . . . .	18
3.3	Pulsatile flow in aneurysm geometries . . . . .	23
3.4	Particle simulations . . . . .	27
<b>4</b>	<b>Towards numerical decision support for aneurysm treatment</b>	<b>33</b>
4.1	Existing methods . . . . .	33
4.2	Proposal of novel assessment method . . . . .	37
4.3	Case study: Portugal geometry . . . . .	40
4.4	Sensitivity . . . . .	48
4.5	Conceptual product . . . . .	53
<b>5</b>	<b>Assessment of PCOM aneurysm</b>	<b>55</b>
5.1	Numerical decision support for PCOM . . . . .	55
5.2	Interpretation PCOM report . . . . .	62
5.3	Sensitivity to alterations in PCOM geometry . . . . .	64
<b>6</b>	<b>Conclusion and outlook</b>	<b>71</b>
<b>A</b>	<b>Validation bolus algorithm analytical Poiseuille</b>	<b>79</b>
<b>B</b>	<b>Validation bolus algorithm numerical Poiseuille</b>	<b>81</b>

# Chapter 1

## Introduction and clinical motivation

Aneurysms are a commonly occurring medical condition, affecting an estimated 2-5% of the total population [57]. They concern a diseased part of a blood vessel. We concentrate on so-called intracranial aneurysms, i.e., aneurysms that form inside the brain. The most threatening complication of this condition is its rupture. Although the chances of rupture are relatively low [26], it often results in severe disability or even death [59]. Multiple options for aneurysm treatment are available. The objective of treatment is occlusion of the aneurysm, either accomplished by pinching the aneurysm neck from the outside, or inserting a metal piece of wire inside the artery, altering the flow to trigger formation of a blood clot. In so-called side-wall aneurysms, treatment is often successful [16], whereas in aneurysms located at junctions between different vessels, known as bifurcation aneurysms, this forms a persistent challenge to medical experts. Involvement of multiple arteries complicates the flow patterns inside the aneurysm geometry.

Together with the development of medical imaging, the field of computational fluid dynamics (CFD) has stepped up to the challenge of trying to predict the risk to a patient and the possible success of a particular treatment. The structures of the diseased vessel can, by use of computed tomography (CT) or magnetic resonance imaging (MRI), be represented to a scale sufficient for detailed fluid flow simulations. CFD on aneurysm structures has been accomplished in multiple studies by now [15, 31, 36, 39, 45], resulting in a large amount of data describing the velocity and pressure fields in the arterial structure. In the simulations in this study, boundary conditions representing the pulsatile behaviour of the heart were used, resulting in an additional temporal dimension of the velocity fields. For the neurosurgeon, it is currently impossible to derive a patient-specific treatment plan based on this extensive, raw data. Some hemodynamic parameters can be calculated, but these are insufficient to describe the complex patterns of the flow [55]. That means there is a remaining gap between the information delivered by CFD, and clear advice desired by the neurosurgeon. In this study, we present a novel method for extracting information from fluid dynamics, aiming to bridge this gap. We propose to present the findings in a multilevel, standardized report, containing information about features of the flow on multiple levels of detail. Ultimately, this type of report can serve the neurosurgeon to find an optimal treatment for a particular patient. This study presents a first detailed step toward this goal.

Figure 1.1 shows a roadmap that describes our opted idealized protocol for handling the patient and his or her medical data adopted from [45]. First, the patient visits the neurosurgeon, who orders an MRI. This MRI contains, besides the desired aneurysm structure, 3-dimensional image data of other tissue present inside the patient's head. Therefore, segmentation of the aneurysm geometry and additional smoothing of the raw MRI-data are required. In the next step, the segmented aneurysm needs to be prepared for CFD. This involves solving a set of partial differential equations, and demands a discrete representation of the vessel geometry, including the aneurysm. After the discretization of the aneurysm geometry, the CFD simulation will be performed. This results in velocity and pressure fields, depending on both space and time. In the final step, information from these fields is analyzed using a new method, introduced in this study. This post-processing results in a report, containing the main features of the flow, that the neurosurgeon can consult when devising a treatment strategy. This pathway is minimally strenuous for the patient: an optimal, patient-specific treatment plan has already been derived before he or she has been touched.

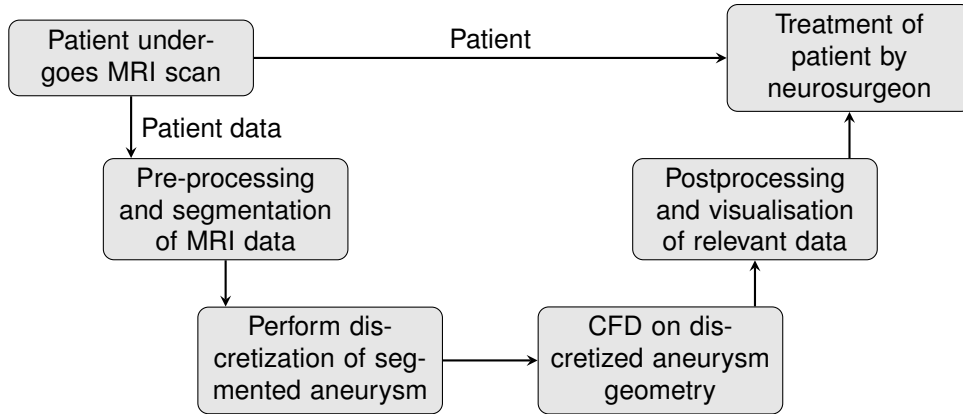


Figure 1.1: Roadmap describing the desired method of treatment of a patient, including our newly proposed post-processing analysis.

The use of CFD in this field of research involves many challenges. The first one being the choice of an adequate spatial and temporal resolution, representing features of the flow dynamics to a level of desired detail. Increasing the grid resolution results in a more accurate representation of the real, continuous geometry, but introduces rather high computational costs. Finding a well-established compromise between these two aspects requires careful consideration which we address in this study, specifying general guidelines for the spatial grid. Another challenge is retrieving information from the enormous amount of data resulting from the fluid simulations, that is relevant to the neurosurgeon. In this study we propose a first particular reporting of CFD findings that can effectively support the neurosurgeon in making clinical decisions. Based on our experience with various assessment methods, we propose a hybrid reporting in which both qualitative and quantitative information about the flow, stresses and load on the aneurysm are combined.

This study has been divided into six chapters, the first one being this introductory part. Chapter 2 gives an overview of the clinical aspects, such as the treatment methods available, as well as the necessary steps to obtain a mathematical model of this problem. Realistic simulation of flow through the geometries is discussed in chapter 3. This concerns handling the mathematical problem as defined in chapter 2 numerically. Also the effects of grid resolution on both steady and pulsatile flow will be considered here. Furthermore, the algorithm developed to model a numerical angiography, forming an important part of our newly proposed numerical decision support, is introduced and analyzed in this chapter. The motivation and procedure behind the assessment of the fluid simulations are topic of chapter 4. Also the effect of a possible treatment on the outcome of this method will be discussed here. Our new post-processing method will be applied on a bifurcation aneurysm, showing a template of the information delivered to the neurosurgeon. This thesis ends with a conclusion and outlook on further research, which together form chapter 6.

# Chapter 2

## Mathematical model

In this chapter, the mathematical model forming the basis of this study will be introduced. First, the pathology and possible treatments are discussed in section 2.1. Subsequently, the procedure for the extraction and definition of the patient-specific flow domain will be presented in section 2.2. Finally, in section 2.3 the governing equations and boundary conditions will be presented.

### 2.1 Pathology and treatment

Intracranial saccular aneurysms are dilations in the artery, associated with a weakening of the arterial wall. They are a common phenomenon, occurring among 2-5% of the population [57]. Frequently, such aneurysms occur in arterial bifurcations, where the blood flow suddenly changes directions. Figure 2.1 shows the circle of Willis, an anatomical structure in the brain where aneurysms are frequently seen. Women have a higher chance of developing an aneurysm than men; 75% of the patients is female [12]. Intracranial aneurysms occur more frequently among elderly people. Moreover, genetics play a role in the development of an aneurysm, but also controllable factors such as smoking, drug usage and alcohol are believed to influence the development of aneurysms [12, 59].

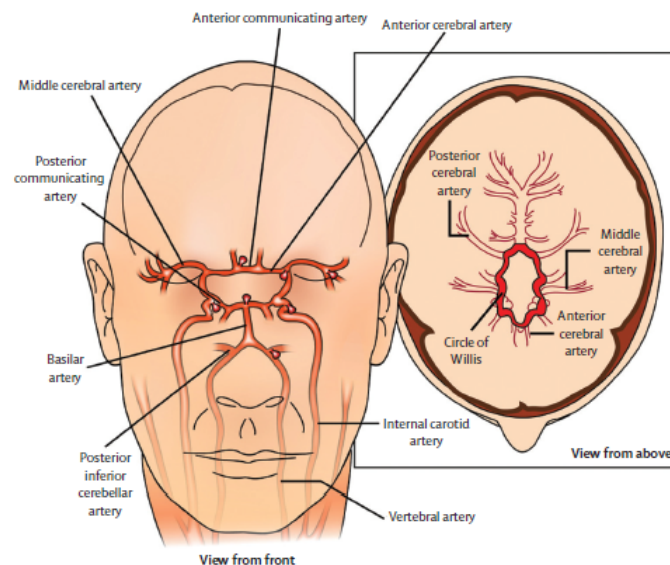


Figure 2.1: Circle of Willis, where intracranial aneurysms may occur [59].

Many theories exist on the pathogenesis of aneurysms. It is considered a complex interplay between the pulsatile hemodynamic forces inside the vessel, and flow-sensitive mechanisms in the endothelial cells in the vessel wall which together drive the so-called remodelling of the aneurysm over time. A hemodynamic parameter that is believed to have a strong connection to aneurysm development is wall shear stress (WSS) [48]. The effect of this force on aneurysm development

is not entirely clear. Areas of low WSS are observed to precede aneurysmal pathogenesis [32], but also high WSS can trigger aneurysmal development [48].

The most severe complication of an aneurysm is its rupture. The short-term mortality rate among patients with a ruptured aneurysm range from 35% to 50%. Half of the survivors are left with severe, long term disability [57]. Therefore, rupture is a complication that needs to be avoided. Fortunately, aneurysms can be treated by a number of procedures, ranging from surgical clipping to more recent endovascular treatment. These treatment options are depicted in figure 2.2.

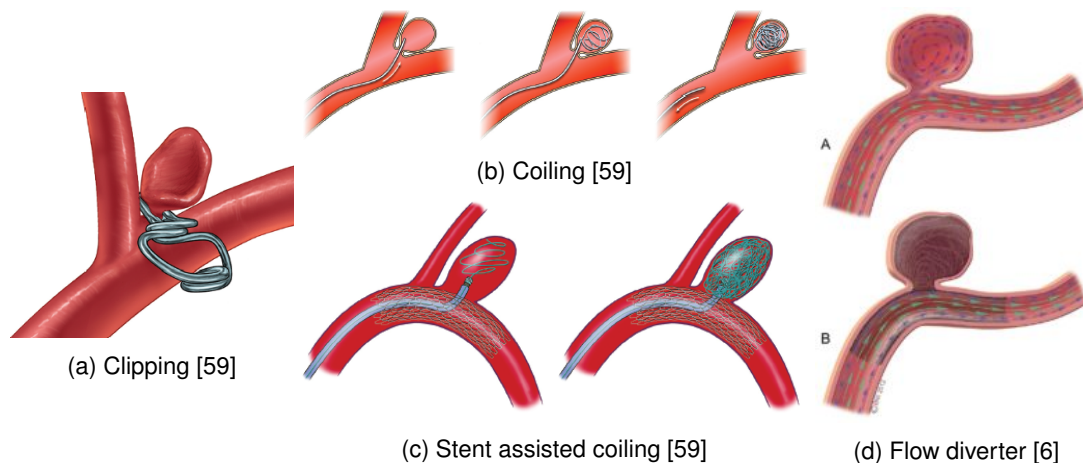


Figure 2.2: Different treatment methods of a saccular aneurysm.

The treatment that was first introduced is surgical clipping. This involves opening of the skull, in order to access the diseased artery and put a metal clip on it, as shown in figure 2.2a. Because the aneurysm is pinched, blood can no longer enter the aneurysm which significantly reduces stresses on the arterial wall. This is the only invasive treatment in the list of options, and is therefore physically more demanding than the others. For decades, this has been the most executed treatment, until it became clear that endovascular treatments such as coiling have a significantly reduced risk of mortality [38].

In endovascular treatment, a metal ‘stent’ or ‘coil’ is inserted from inside an artery located in the groin and employed at the diseased part of artery in the brain, making the procedure non-invasive. The objective is to manipulate the flow in such a way that an occluding thrombus can form in the aneurysm sac [42]. The first introduced endovascular technique was coiling. This method is shown in figure 2.2b. In this procedure, a long wire is inserted inside the aneurysm. The metal wire inside the aneurysm slows down the blood flow locally, which causes a blood clot to form. This method is not suitable for aneurysms that have become too large or have a wide neck [59]. In some of these complex cases stent-assisted coiling, as shown in figure 2.2c is successful. Since this procedure is more complex than regular coiling, it can also introduce other complications, such as in-stent stenosis [54].

The most modern form of endovascular treatment involves the insertion of a flow diverter, as shown in figure 2.2d. Such a flow-diverting stent consists of many thin wires, woven together to a cylindrical and flexible piece of pipe. Various flow diverters are available, varying in the number of wires, wire diameter and porosity. Often used are the Surpass by Stryker Neurovascular and the Pipeline Embolization Device by ev3/Covidien, which have a reported aneurysm occlusion rate of respectively 75% and 80% 6 months post-treatment [7]. Inserting such devices in a blood vessel modifies the flow pattern, in such a way that the blood inside the aneurysm is slowed down and a thrombus can form. This treatment may introduce a possible complication when employed at a

bifurcation aneurysm. This type of aneurysm is situated at the junction between an artery and its side branch. In some cases, treatment with a flow diverter can cause occlusion or narrowing of the bifurcating vessel, which decreases the capacity of this side-branch [41].

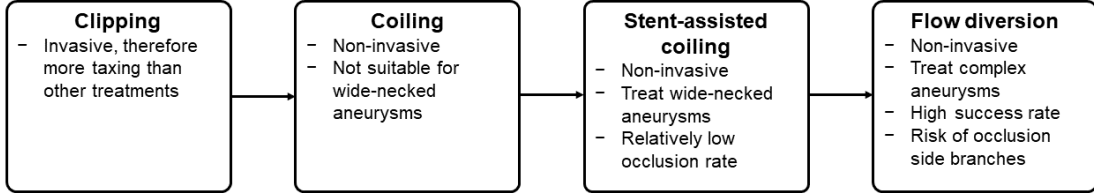


Figure 2.3: Overview of intracranial aneurysm treatment options

In figure 2.3 a chronological overview of various aneurysm treatment options is given. The endovascular methods are non-invasive to the brain and allow a more and more detailed intervention at the diseased area. These treatments are not always successful. On a small population ( $N = 21$ ), it has been shown [16] that a flow diverter is most successful in treating straight sidewall aneurysms, while it may have difficulties with bent sidewalls and bifurcation aneurysms. Because of the complexity of the flow and the geometry, it is currently impossible to see immediately after treatment whether it has been successful, i.e., whether long-term stable occlusion will occur. It can take up to a couple of months for the aneurysm to be completely occluded. The occlusion of the aneurysm is assessed at follow-up examinations of the patient, that are done a few weeks up to a few months after treatment. These complex and currently challenging cases are of special interest in this study.

Aneurysms located in the posterior communicating artery are a commonly seen example of a bifurcation aneurysm [19]. This artery can take many anatomical configurations, involving connection of the PCOM to the ICA, as well as different ratios between the diameters of these two vessels [21]. It appears that the success rate of treatment deteriorates with a so-called fetal type configuration, where the PCOM has a larger diameter than the ICA. Patients with this arterial configuration often require additional treatment [56]. This can be explained by the relatively high residual flow through the PCOM, which results in insufficient delay of blood flow inside the aneurysm. The influence of different anatomical configurations on the flow field will be researched in section 5.3.

## 2.2 Geometry

To make a mathematical model of the flow in an aneurysm, a realistic geometry of the aneurysm is required. The first step is to obtain medical imaging data of the patient. Currently, magnetic resonance angiography (MRA) is the preferred technique over catheter angiography, since it is non-invasive and does not involve ionizing radiation [30]. Using MRA, one is able to visualise tissue and vessel structures inside the skull. The outcome of this scan is a DICOM file: a 3D image representation consisting of so-called voxels. Voxel sizes can vary, in [36] the reported voxel size was approximately 0.1 mm. Each voxel has a certain intensity based on the type of tissue it represents, this translates to a specific grey scale value in the image. The majority of this 3D image contains redundant information in case one only wants to reconstruct the part containing the aneurysm. Therefore, this data needs to be segmented, which can be done by choosing grey scale thresholds. Determining these thresholds is not trivial; taking the upper and lower threshold too closely together results in loss of information about the region of interest, and choosing them too far apart results in data containing noise and artefacts. The resulting segmentation of the aneurysm geometry is often quite rough, and requires an additional smoothing step and possibly

additional manual reconstruction steps in case the imagery represents a structure with holes and unrealistic features. The procedure from raw medical image data to aneurysm geometry adopted here is described in more detail by Ong in [45].

After segmentation and smoothing of the raw medical data, one obtains geometries such as displayed in figure 2.4, showing three arteries with aneurysms. The aneurysm in figure 2.4a is obtained from [17] and is a lot smoother than the other two geometries shown. This geometry represents a side-wall aneurysm, whereas the other two are bifurcation aneurysms. The data for the bifurcation aneurysms was kindly provided by Julia Mikhal [36]. We will discuss the geometry in figure 2.4c in more detail in the remainder of this section, as treatment of this type of aneurysm presents a main challenge to current neurosurgeons.

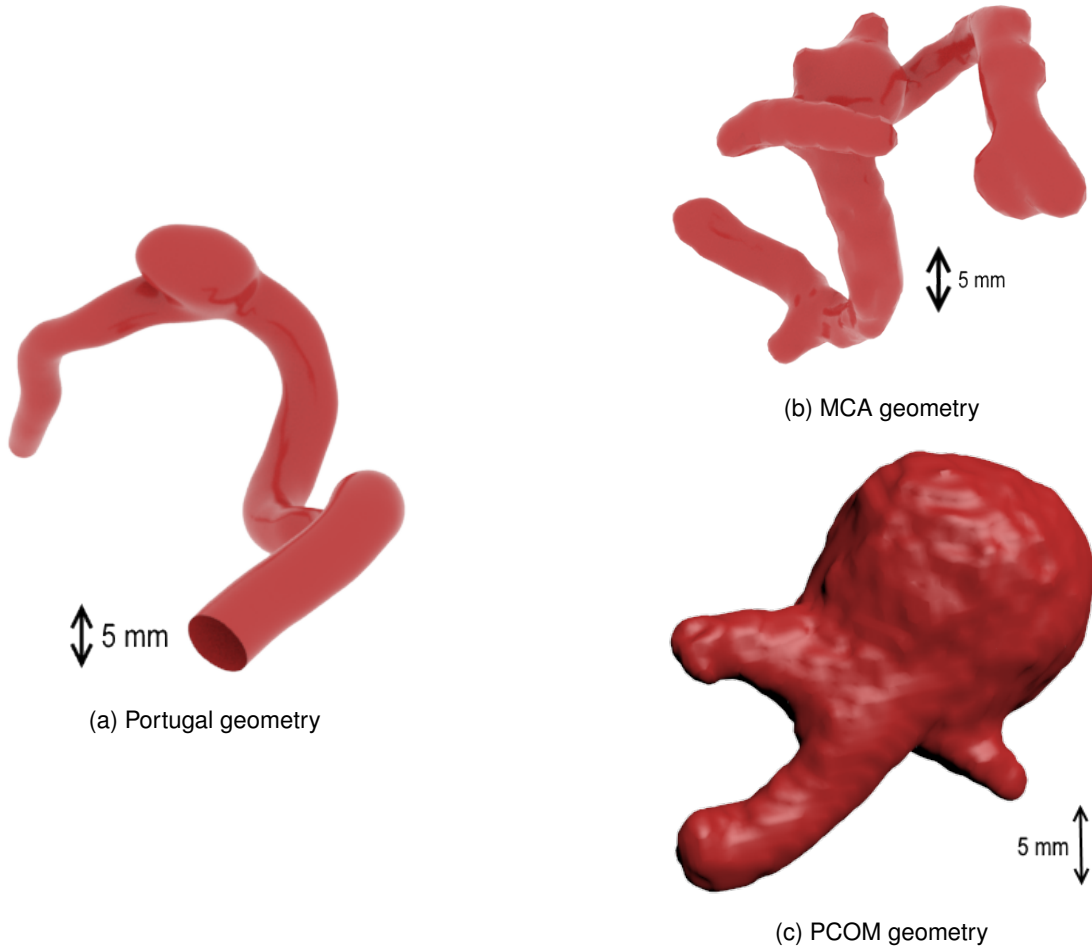


Figure 2.4: Segmentation and smoothing of three different aneurysm geometries used in this thesis. In (a) we show the 'Portugal' geometry [17], in (b) an MCA geometry is depicted with a characteristic shape and in (c) a PCOM geometry is shown with strong flow in both bifurcating vessel branches.

The aneurysm in figure 2.4c is a bifurcation aneurysm situated at the junction between the internal carotid artery (ICA) and the posterior communicating artery (PCOM). It has a diameter of 16mm, which classifies as a large aneurysm [3]. The boundary of this particular geometry consists of four subdomains, on which different boundary conditions will be imposed. These boundary conditions are described in more detail in section 2.3. The inlet forms the first subdo-

main of the geometry boundary, in this case the ICA at the bottom. Blood enters the geometry via this vessel, some part continues through the aneurysm sac and eventually departs through either of the two outlets. The larger vessel on the left is the continuation of the ICA, the smaller artery on the right is the PCOM artery bifurcating from the ICA. The last subdomain of the boundary of this geometry is the vessel wall. A schematic overview of the boundaries of this aneurysm, as well as its location are depicted in figure 2.5.

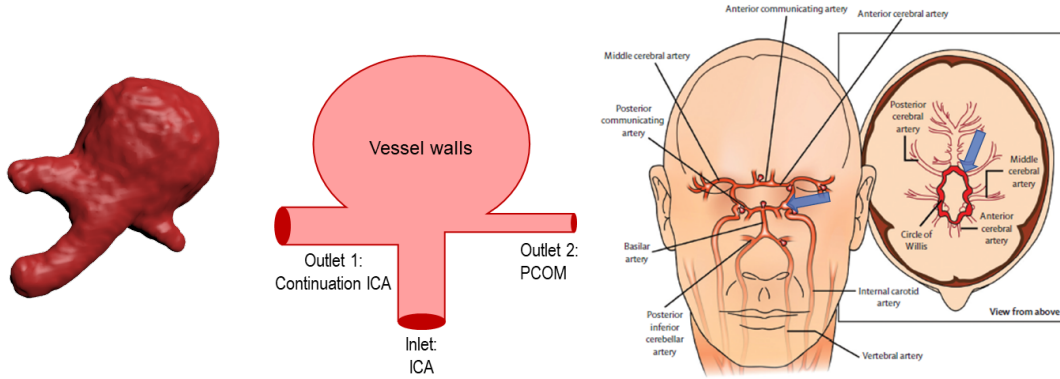


Figure 2.5: Smooth representation of the PCOM aneurysm, together with a schematic overview of the subdomains of its boundary. Location of this aneurysm inside the human brain is shown in the rightmost image.

In the model used in this study, the vessel walls are assumed to be rigid. Movement of the vessel wall is influenced by many factors, for example: flow velocity, wall shear stress, contraction of surrounding muscles, but also concentration of calcium ions in the blood can influence elasticity [9]. It was shown experimentally by Oubel et al. in [46] that the movement of the vessel walls in intracranial aneurysms throughout the cardiac cycle is small compared to the vessel diameter and the size of the aneurysm sac. Hence, the main features of the flow in an aneurysm are expected to be captured well when assuming rigid geometries. In cases where motion of the geometry is required as well, additional information about the patient is required which express deformability and elasticity of the surrounding tissue.

## 2.3 Navier-Stokes and boundary conditions

In the computational model, blood is modelled as an incompressible, Newtonian fluid, implying a constant viscosity and density. Non-Newtonian aspects of blood flow are of considerable influence when the structures within the geometry become sufficiently small. This is the case when the diameter of the blood vessel is of a size comparable to the particles inside the blood ( $\pm 10 \mu\text{m}$ ), for example when blood flow in capillaries is considered [9]. We consider flow in the main structures in the circle of Willis, characterized by typical vessel diameters of about 5 mm. In these cases, the size of the geometries is large compared to the size of the particles contained in the blood, and non-Newtonian influences of the particles in the blood are small. This is also confirmed in the study performed by Morales et al. in [39], where flow fields obtained from both non-Newtonian and Newtonian models were compared. Our decision for a Newtonian flow model is in accordance with previous studies on computational fluid dynamics in cerebral aneurysms, for example by Castro et al. [14] and Mikhal [36].

The flow in a domain is driven by an imposed (time-dependent) mass flow rate. This corresponds to a (time-dependent) pressure gradient, and its behaviour is described by the Navier-Stokes



equations:

$$\begin{aligned}\frac{\partial \vec{u}}{\partial t} + \vec{u} \cdot \nabla \vec{u} &= -\nabla P + \nu \nabla^2 \vec{u} + \vec{f} \\ \nabla \cdot \vec{u} &= 0\end{aligned}\tag{2.1}$$

The first equation is called the momentum equation and describes the conservation of momentum through the coupling between the velocity and the pressure. The second equation is also known as the continuity equation, which ensures conservation of mass in an incompressible flow field. In these equations,  $\vec{u}$  represents the velocity field with components in the  $x, y$  and  $z$  directions. Moreover,  $P$  stands for the kinematic pressure defined as  $P = p/\rho$  where  $p$  is the physical pressure and  $\rho$  is the mass density of the fluid,  $\nu = \mu/\rho$  is the kinematic viscosity in terms of the molecular viscosity  $\mu$  and the mass density. Finally,  $\vec{f}$  represents an external forcing term.

In this study, we use the external forcing term  $\vec{f}$  to represent an immersed boundary that describes the complex shape  $\Omega_F$  of the vessel geometry, within a regular-shaped enclosing domain  $\Omega$ . The part  $\Omega \setminus \Omega_F = \Omega_S$  is defined to be solid. The division of a two-dimensional domain into non-overlapping fluid and solid subdomains, can also be seen in figure 2.6. A masking function  $H(x)$  is introduced to represent this partition, which is defined as follows:

$$H(x) = \begin{cases} 0 & x \in \Omega_F \\ 1 & x \in \Omega_S \end{cases}\tag{2.2}$$

Together with a relaxation time parameter  $\epsilon$ , this can be combined in a penalisation term for nonzero fluid flow outside  $\Omega_F$ :  $\vec{f} = -\frac{1}{\epsilon} H \vec{u}$ . This means that the Navier-Stokes equations have no external term inside  $\Omega_F$ , and  $\vec{u}$  is the solution to these equations. Outside the domain, the penalisation term comes into play. Since the vessel wall is non-permeable, we take  $\epsilon \ll 1$ . Then, if  $x \in \Omega_S$ , equation 2.1 implies  $\frac{\partial \vec{u}}{\partial t} = -\frac{1}{\epsilon} \vec{u}$  in case the velocity would be non-zero. This has as solution  $\vec{u} \sim e^{-\frac{t}{\epsilon}}$ , showing that  $\vec{u}$  goes exponentially to zero outside the fluid domain at an extremely high rate whenever the velocity would be non-zero anywhere in the solid. This penalisation term ensures that the fluid velocity is very close to zero outside the fluid domain. More information on the accuracy and a few examples featuring the immersed boundary method can be found in [53]. A more detailed review of volume penalization methods including domains with moving boundaries, is given in [37].

The aneurysm geometry presented here is a small section of the cardiovascular system, for which we wish to acquire the flow dynamics. Separating this structure from the remaining cardiovascular system is a necessary step to keep computational costs reasonable. By imposing suitable boundary conditions for pressure and velocity on the inlet, outlet and walls of this geometry, the flow inside the aneurysm can be approximated well. On the walls, no-slip boundary conditions are imposed, reflecting that the fluid adapts to the velocity of the walls and can not penetrate the walls. A time-dependent mass flow was imposed in combination with a uniform velocity field at the inlet to mimic a beating heart. Finally, a zero-gradient boundary condition normal to the outlets is adopted to create a smooth connection to the rest of the circulation. This completes the boundary conditions on fluid-solid interfaces for the velocity. Boundary conditions on the pressure term in the Navier-Stokes equations have been subject of a lot of discussion in the field of CFD and mathematics [50]. Simulations of fluid flow under the boundary conditions  $\frac{\partial p}{\partial n} = 0$  have been considered by Vreman in [58]. The condition  $\frac{\partial p}{\partial n} = 0$  on the walls represents walls as being impermeable. On the inlet and outlet, we impose homogeneous Neumann and Dirichlet boundary conditions respectively, in agreement with [45].

The pulsatile profile specified for the velocity at the inflow represents the beating of the patient's heart. The adopted time-dependence of the corresponding mass-flow rate in the internal carotid

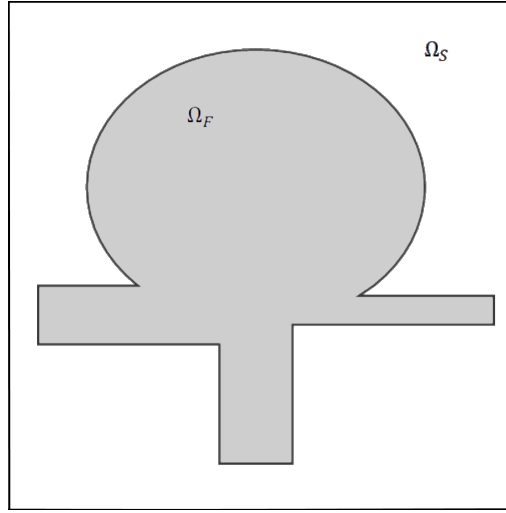


Figure 2.6: Division of domain  $\Omega$  into fluid and solid subdomain,  $\Omega_F$  and  $\Omega_S$  respectively.

artery is shown in figure 2.7 cf. [36]. It shows the flow rate through the inlet of the vessel as a function of time. This mass-flow rate profile is imposed as a uniform velocity field at the inlet of the geometry, by dividing the mass-flow rate by the area of the inflow vessel. A single cardiac cycle takes 0.8 seconds in our model, and goes through two stages: systole and diastole. These profiles can be measured at high temporal resolution using the noninvasive Transcranial Doppler Ultrasound technique [40]. The particular profile seen in figure 2.7 was an average of the cardiac profile measured for multiple healthy volunteers, reported in [36]. For aneurysms located elsewhere in the brain or for a specific patient, the imposed external flow rate should be measured separately, to obtain a realistic boundary condition. Alternatively, 1D models of the circulation in the entire human body can serve as point of reference for the imposed mass-flow rate as well [28].

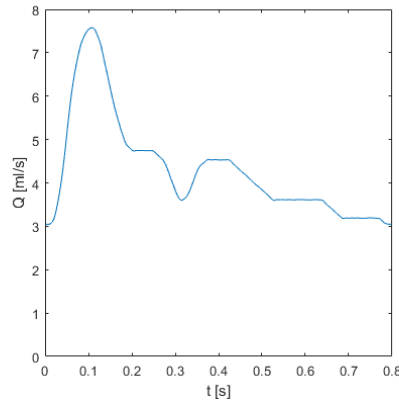


Figure 2.7: Volume flow rate (in ml/s) through the inlet of the PCOM aneurysm cf. Figure 2.4c, throughout one cardiac cycle.

The pulsatile inlet boundary conditions are imposed as a time-dependent uniform flow field. This is not entirely realistic, as developed flow, e.g., through a pipe has a shape that is closer to a parabolic profile, with a maximum velocity in the middle of the pipe reminiscent of Poiseuille flow. The block profile is specified such that it represents the average value of the actual profile. A selection of inlet velocity profiles have been simulated in [31], it appeared that the resulting flow

fields have minimal variation further downstream of the numerical inflow location. In the configuration available for this research, this room for development of the flow is quite restricted. Hence, the block profile is an approximate representation used to study the flow downstream in the aneurysm region. This illustrates that future studies should incorporate a somewhat larger section of the domain upstream of the aneurysm to improve the approximation. The computational overhead for this extension of the flow domain is quite modest because the immersed boundary method enables to represent this very effectively.

The character of the flow, i.e., laminar, transitional or turbulent, is determined by the Reynolds number ( $Re$ ). The Reynolds number can be calculated using a reference length  $L_r$ , reference velocity  $U_r$ , and a reference kinematic viscosity  $\nu_r$ . It is defined as follows:

$$Re = \frac{U_r L_r}{\nu_r}. \quad (2.3)$$

The Reynolds number for the PCOM geometry shown in figure 2.4c was estimated as follows. The radius of the inflow vessel (ICA) was used as reference length, which is  $L_r = 0.25$  cm. The reference velocity is taken as the maximum velocity attained in the pulsatile flow, which occurs at  $t = 0.11$  s and equals  $U_r = 38.6$  cm/s. The kinematic viscosity of blood equals  $\nu_r = 3.25 \cdot 10^{-6}$  m<sup>2</sup>/s and was used as the reference viscosity. Therefore, the Reynolds number at maximum velocity is estimated as 292. On average, the velocity in this vessel equals 22 cm/s. If this would be used as reference, one obtains a Reynolds number of 170. This means that the flow is laminar, and can show unsteady behaviour in response to the unsteady pulsatile flow forcing at the inflow.

The entrance length for full development of the flow depends on both the Reynolds number and the diameter of the vessel. For laminar flow, the entrance length can be calculated. For the PCOM geometry, it is estimated to be 5 cm. The internal carotid artery in the PCOM geometry as shown in Figure 2.4c appears to be shorter than the calculated entry length. That means the flow is not fully developed inside the aneurysm. There are multiple ways to deal with this issue. One option was explored by Mikhal, who extended an aneurysm geometry periodically with a connector, and compared this to the aneurysm with the original geometry. No major differences were detected in the resulting fluid dynamics inside the aneurysm in case the ‘connector-length’ was varied on the scale of the entrance length [36]. So, extending the inlet of the geometry to the entry length with the method introduced in Mikhal could be an improvement of the current method. Another option would be to leave a longer part of the inflow vessel attached to the geometry during segmentation.

The mathematical model is now specified and the precise domain, boundary conditions, governing equations and pulsatile flow profile are determined. This is the basis for the discrete computational model that is implemented in OpenFOAM. This is subject of the next chapter.

## Chapter 3

# Flow prediction in intracranial aneurysms

In this chapter, the numerical methods used for simulation of blood flow through the general vessel geometries are covered. Section 3.1 treats the discretization of the immersed boundary method introduced in section 2.3. This section also includes a brief description of the software that was used for the simulations. Section 3.2 shows steady flow simulations for two different bifurcation aneurysms at varying grid resolutions. Simulations on these geometries with pulsatile boundary conditions are subject of section 3.3. For visualising the Lagrangian aspects of the fluid flows, the motion of a cloud of passive particles was simulated, modelling a so-called ‘bolus’ administered to a patient. The algorithm that has been developed specifically for this purpose will be presented in section 3.4.

### 3.1 Immersed boundary method and OpenFOAM

In this section we first sketch the main characteristics of the translation of the immersed boundary (or volume penalisation) method to a discrete model. Subsequently, we describe upper- and lower bounding solutions that can be obtained to quantify the sensitivity of the flow to uncertainties in the domain definition. Finally, the use of OpenFOAM [1, 2] for simulation of pulsatile blood flow is discussed.

Figure 3.1 shows the transition from a continuous masking function to a discrete one. For clarity, a two dimensional domain has been considered. The fluid domain is submerged in a Cartesian grid, with a finite number of cells. The value the masking function takes on this grid is determined per grid cell, which is treated as either fluid or solid. The discrete function  $H(x_{ij})$  is defined in the grid point  $x_{ij}$  as follows:

$$H(x_{ij}) = \begin{cases} 0 & x_{ij} \in \Omega_F \\ 1 & x_{ij} \in \Omega_S \end{cases} \quad (3.1)$$

Determining which  $x_{ij}$  are in  $\Omega_F$  requires additional care around the boundaries of the fluid domain. Multiple, mutually consistent ways of handling the masking function around fluid-solid interfaces are covered by Mikhal in [36]. In a two-dimensional domain, three strategies of defining the boundaries of the fluid domain were distinguished: basic, inner and outer. In the basic strategy, the cell center defines the property of the entire cell, i.e., if at the center  $x_{ij}$  of a grid cell the domain is fluid or solid then this property is also adopted for the entire grid cell. The inner and outer strategies rely on additional information of the corners of the cells. In the inner strategy, a cell belongs to the fluid domain if all four corners are in  $\Omega_F$ . For the outer strategy, it is sufficient when at least one corner belongs to the fluid domain for the entire cell to be treated as part of the fluid domain. The differences are depicted in figure 3.2. In [36], this method was extended to three-dimensional grid cells. In principle, nine different strategies, and consequently nine slightly different geometries can result from this extension. It was shown that the velocity and pressure fields resulting from the basic strategy are bounded by those of the inner and outer

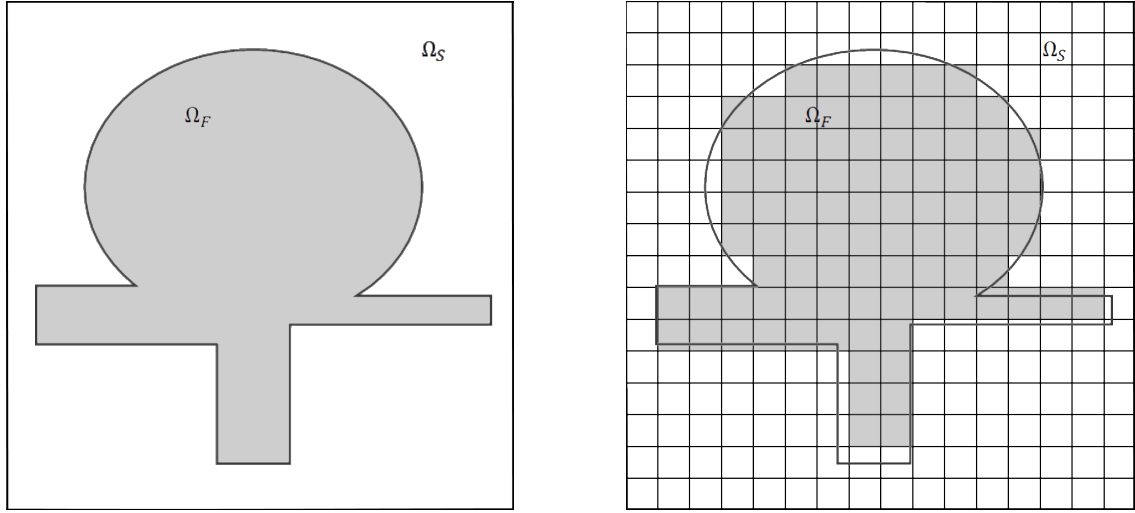


Figure 3.1: Continuous and discrete masking function.

strategies thereby giving a systematic way to investigate the sensitivity of fluid flow predictions on slight uncertainties in the definition of the flow domain. The masking functions used in this study are based on the basic strategy.

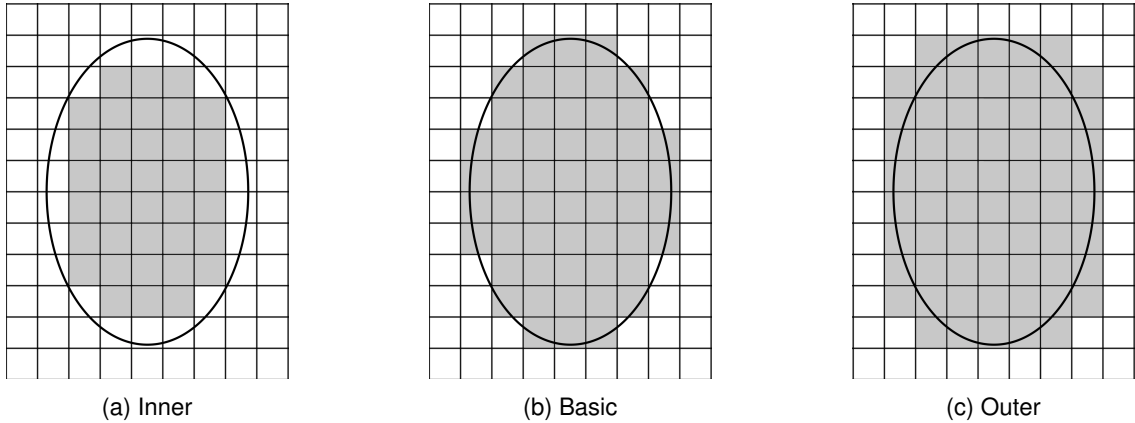


Figure 3.2: Different strategies for defining the masking function in two dimensions: the case of an ellips is illustrated here.

In figure 3.1 it can be seen that the shapes of the discrete and continuous masking functions are alike, but not equal. The discrete masking function converges to the continuous masking function when the grid cell size  $\Delta x \rightarrow 0$ . Decreasing the grid cell size will result in a more realistic geometry, but also yield high computational costs for the flow simulation. In these simulations, the data is three dimensional in space, and time-dependent because of the pulsatile conditions. To retain numerically stable simulations, doubling the spatial resolution in each direction requires doubling of the temporal resolution as well. As a consequence, the computational costs become 16 times as high with each doubling of the resolution. This highlights an important challenge in this study: simulations should be realistic, but also computational time needs to be limited to manageable proportions. To compare grid resolutions of different geometries, we will measure the number of grid cells per diameter of a characteristic blood vessel nearby. This represents the number of grid cells on the diameter of the inlet vessel.

Masking functions as used in the immersed boundary method are not the only way of discretizing the complex domain of an aneurysm geometry. Body-fitted grids are also used for fluid simulations, for example in [42]. The advantage of these body-fitted grids is that the cells can be arched, and follow the presumed fluid-solid interfaces more closely. A major disadvantage is that construction of a body-fitted grid is considerably more user-intensive than a masking function. Moreover, in case of highly complex domains associated with the introduction of a flow-diverting device, the gridding may even be unsuccessful and lead to grids that do not yield accurate local solutions. An example of an intricate geometry of a flow diverter is the Surpass flow diverter by Stryker [4], shown in figure 3.3. Furthermore, immersed boundary grids are preferred over body-fitted grids when assessing the effect of intervention. In fact, the geometry of the flow domain is not available with great accuracy and at very high resolution - segmentation issues will add to this uncertainty. Upper- and lower bounding solutions can be used to estimate this uncertainty, which is not well possible with a body-fitted gridding.

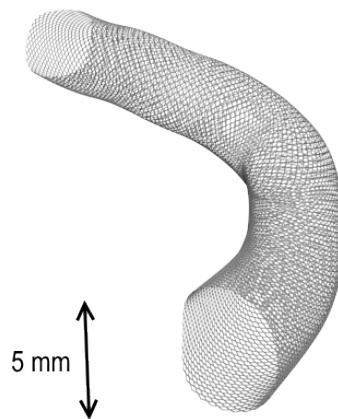


Figure 3.3: Surpass Evolve flow diverter by Stryker [4]

The boundary conditions as described in section 2.3 are imposed on the discrete underlying grid and solved in the publicly available OpenFOAM software [2]. It contains many solvers, for numerical solutions of numerous physical problems, such as flow past an airfoil, or multiphase flow. In this work, the solver `pisoFoam` will be used for laminar, incompressible flow of a Newtonian fluid. More information on the different solvers, as well as usage of OpenFOAM can be found in [1].

Each simulation in OpenFOAM is stored in a separate directory, referred to as a case. A case consists of three subdirectories: `0`, `constant` and `system`. The files that define the geometry of the fluid domain are contained in the `constant` folder. These files also introduce a partition of the boundary; boundary conditions are imposed on each separate part of the boundary. The actual boundary and initial conditions are contained in the `0` folder. The `system` directory contains the `controlDict` file, which defines the desired solver, the size of the time steps, start time and end time. The time-discretization schemes are specified in the file `fvSchemes`, which is also in the `system` directory.

The Navier-Stokes equations are solved using an implementation of the PISO algorithm available in OpenFOAM. The PISO algorithm, short for *Pressure Implicit with Splitting of Operators*, was first introduced by Issa in 1986 [22], as an extension of the so-called SIMPLE algorithm that was introduced by Caretto et al. 13 years prior [13]. Both methods rely on pressure correction, an iterative method for solving the Navier-Stokes equations. The idea of this pressure correction is

as follows. The momentum and continuity equations of incompressible flow are given by:

$$\begin{aligned}\frac{\partial \vec{u}}{\partial t} + \vec{u} \cdot \nabla \vec{u} &= -\nabla P + \mu \nabla^2 \vec{u} + \vec{f} \\ \nabla \cdot \vec{u} &= 0.\end{aligned}\tag{3.2}$$

Note that these are, in our specific problem, four equations with four unknowns, since the momentum equation consists of an  $x$ ,  $y$  and  $z$  component. The continuity equation, however, acts rather as a constraint than as an additional equation. That means that only solutions of the momentum equations with a divergence-free velocity field are valid solutions of the incompressible Navier-Stokes equations. The first step of these pressure correction methods consists of discretizing the momentum equations, which is done using the finite volume method. The nonlinear convection term is handled using an iterative method [43]. The momentum predictor solves the momentum equation using the pressure gradient from the previous time step [23]. The resulting velocity field does not satisfy the continuity equation. This is corrected for by two corrector steps, derived from the continuity constraint: the first one is implicit, correcting the pressure field and the second one is an explicit correction of the velocity, using the freshly updated pressure field. Since these actions introduce terms relying on both pressure and velocity, which are updated throughout the algorithm, this predicting and correcting is an iterative process until the velocity and pressure both converge within a predefined tolerance.

The main difference between SIMPLE and PISO is that the SIMPLE algorithm was originally intended for incompressible, steady flow, and uses underrelaxations ensuring stability of the simulations. The PISO algorithm was intended for incompressible, unsteady flow and does not need underrelaxations for stability [43]. Since in this type of flow the non-linear coupling is much less important than the pressure-velocity coupling, the momentum predictor step is only gone through once; the nonlinear term can be frozen for a number of pressure-correcting iterations [23]. However, this is only a valid assumption for small time-steps [43]. In the SIMPLE algorithm, intended for steady flow and involving much larger time-steps, the non-linear coupling is assumed to be stronger than the pressure-velocity coupling and hence the momentum predictor step needs to be repeated in each correction loop, slowing down the convergence rate. In this study, we deal with unsteady flow, since the pulsatile behaviour of the heart is used as a boundary condition. Therefore, the PISO algorithm is preferred over the SIMPLE algorithm. More details on both algorithms can be found in [1, 22, 23, 43].

To reduce computational time, OpenFOAM has an option to run on multiple CPU's. The simulations in this thesis have been executed in parallel on 80 CPU's, on the Cartesius and Serendipity supercomputers located in Amsterdam and Enschede respectively.

## 3.2 Steady flow in aneurysm geometries

The numerical methods described in section 3.1 were used to calculate the flow field in the aneurysm geometries given in figures 2.4b and 2.4c. In this section, these flow fields will be analyzed. Specifically, we visualize the flow that develops for steady conditions and investigate the sensitivity to variations in the spatial resolution. This will be done for two bifurcation aneurysms. First, we address a so-called PCOM aneurysm. Afterwards we present an MCA case.

### PCOM

The masking functions at four different resolutions for the PCOM geometry are shown in figure 3.4. Inflow at the bottom is directed in the positive  $x$ -direction. An average velocity of 22 cm/s at the inlet of this aneurysm best resembles the natural situation for steady flow [61] and was

imposed as a block profile. In section 2.3, the Reynolds number was estimated at 170, which corresponds to laminar flow inside this geometry.

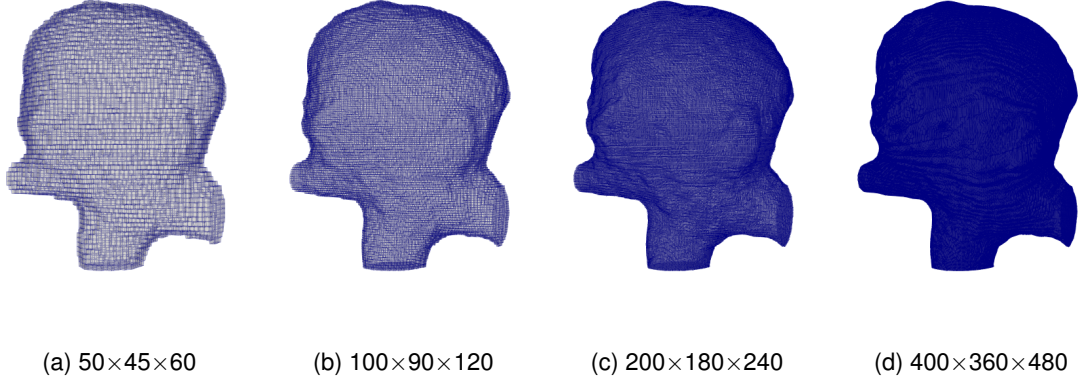


Figure 3.4: Geometry of PCOM aneurysm at different grid resolutions. The geometries have respectively 12, 24, 48 and 96 grid cells per diameter of the inflow vessel.

A first impression of the flow can be seen in figure 3.5. These figures show steady state streamlines, with different underlying grid resolutions. The streamlines at each of the four resolutions show similar behaviour. Most streamlines go inside the aneurysm lumen. There the velocity decreases, and many complex flow patterns are revealed. After passing through the vortex inside the aneurysm, blood flows out through either of the bifurcating blood vessels; the continuation of the ICA or the PCOM. Upon closer inspection, there are subtle differences in the shape of the vortex under varying resolutions, but there were no major differences in the magnitude of the velocity. This gives confidence in the adequacy of the spatial resolution in relation to the structures in the flow field.

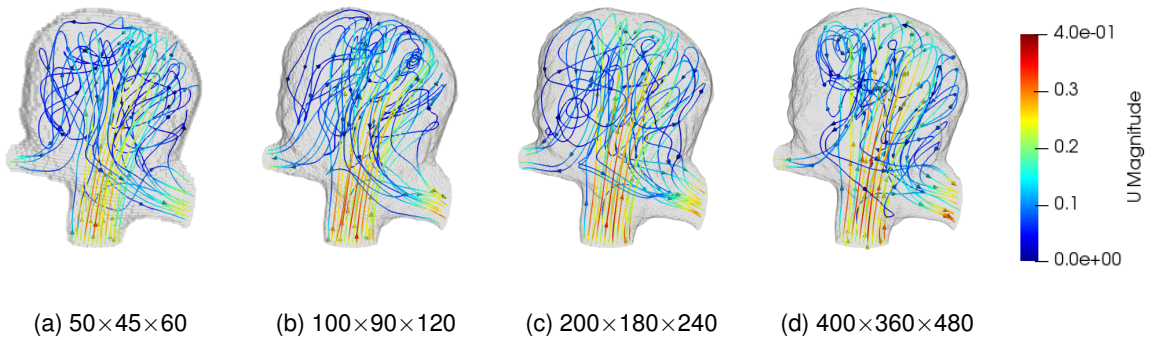


Figure 3.5: Streamlines at steady state for the different grid resolutions. Colors indicate the magnitude of the velocity along the streamline.

In figure 3.6, the magnitude of the velocity along a cross section of the PCOM aneurysm is shown. Again, the figures of the four different resolutions look alike. All four of them show a jet flowing out the ICA into the aneurysm. In literature, this is referred to as an impinging jet, which is common in aneurysms [15]. Although the magnitude of the velocity near the inlet is comparable for the four resolutions, the velocity of the jet decreases faster in the two coarsest resolutions. Additionally,



the direction of the jet varies among the different resolutions. For the  $100 \times 90 \times 120$  resolution, the end of the jet 'curls' to the front of the geometry, as opposed to the remaining three resolutions. Furthermore, this particular resolution has a detached 'tail' in the back of the aneurysm lumen. Besides these small variations in the topology of the flow field, magnitudes of the velocity are within the same range, further underpinning the spatial resolution used in these simulations.

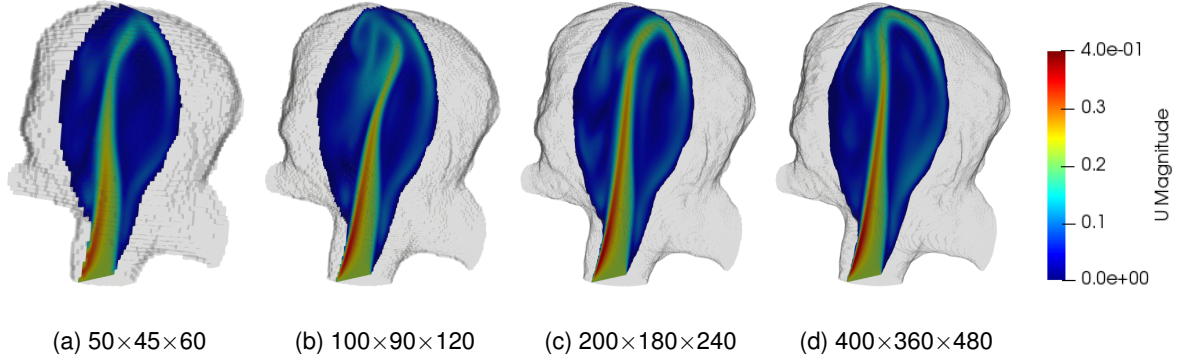


Figure 3.6: Cross section of the velocity field in the  $x$  direction at different grid resolutions.

Figure 3.7 displays the velocity fields normal to a cross-section inside the aneurysm at the different resolutions. These images provide more details on the flow pattern within the aneurysm sac. In the streamlines, presence of a vortex in the aneurysm sac was evidenced. This vortex can also be noted in the cross sections, which contains a patch of flow in positive  $x$ -direction, and a surrounding area in negative  $x$ -direction. The positively directed flow has a slightly higher magnitude at higher resolutions. This is confirmed by the cross sections in figure 3.6, where the magnitude of the impinging jet increased with increasing of the resolution.

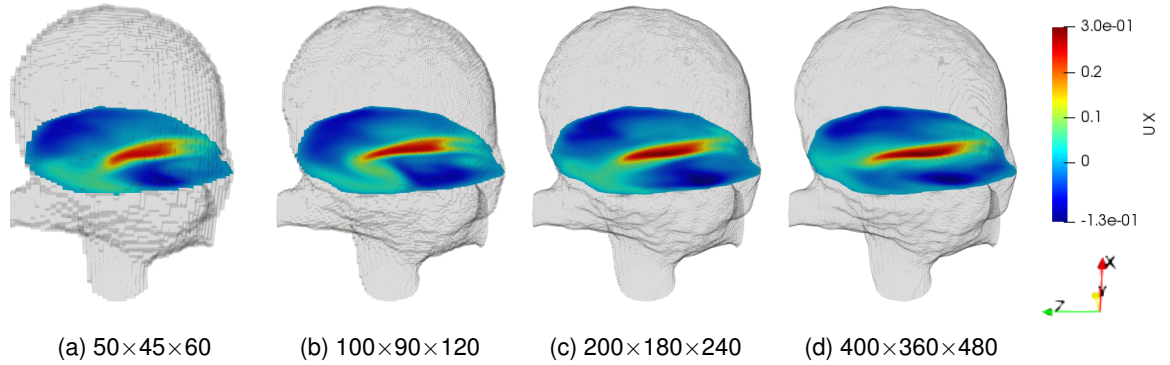


Figure 3.7: Cross section of the velocity field in  $x$ -direction in the aneurysm sac.

Up to now, resolution study of the PCOM geometry has been based on qualitative features of the flow field. This gives a first idea of the errors associated with the numerical method. More quantitative features should be monitored as well. These offer a measurable difference between the flow fields. Quantitative measures considered in this analysis are kinetic energy and average velocity. Kinetic energy is defined as  $\frac{1}{2} \sqrt{U_x^2 + U_y^2 + U_z^2}$ . The mean velocity is defined as the magnitude of the velocity averaged over the entire geometry. These quantities are global measures of the simulation. Both have been computed for all intermediate time steps throughout the

simulations, from  $t = 0.05$  s up until the well-developed state at  $t = 3$  s.

The evolution of kinetic energy and average velocity over time can be seen in figure 3.8. The kinetic energy and velocity have a similar range for all resolutions. Although the inflow condition of the geometries is stable, both quantities show non-periodic fluctuating behaviour after  $t = 0.2$  s. Apart from the coarsest resolution, the graphs fluctuate around almost the same constant level. Based on these graphs, it is not possible to strictly determine the order of convergence although general convergence is well appreciated. The averages of both quantities from the three highest resolutions between  $t = 0.2$  s and  $t = 3$  s are very close together. However, they are not strictly increasing. Therefore, the strict order of convergence remains unclear with this way of measuring.

The fluctuating behaviour of the flow illustrates the transient behaviour at the current Reynolds number. Because of the low viscosity of blood, the inflow jet in the aneurysm is quite complex and does not settle into a steady flow. To investigate this further, we considered increasing the viscosity. It appeared that an increase in the viscosity of the fluid stabilised the otherwise oscillatory quantities. The kinetic energy and average velocity stabilised for the duration of the simulation at approximately  $Re = 100$ . This illustrates the onset of transient behaviour beyond a critical Reynolds number, a feature that is well-known in fluid mechanics. Our computational model correctly captures this.

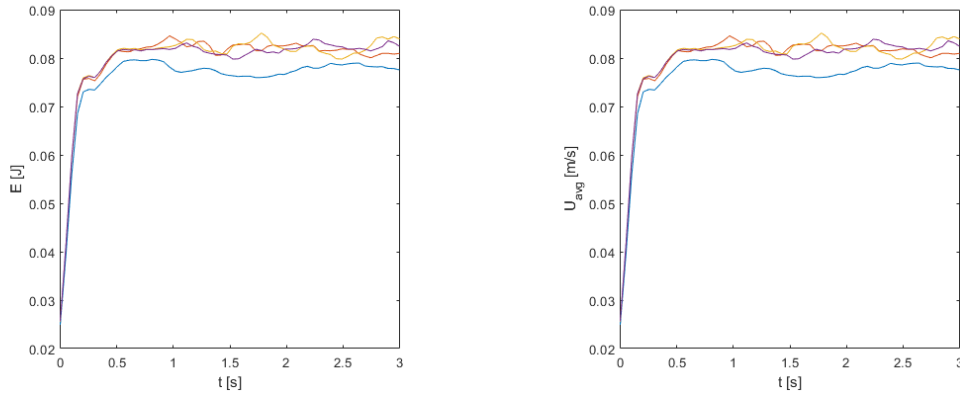


Figure 3.8: Average kinetic energy and average velocity for different resolutions of the PCOM geometry. Blue:  $50 \times 45 \times 60$ , orange:  $100 \times 90 \times 120$ , yellow:  $200 \times 180 \times 240$  and purple:  $400 \times 360 \times 480$ .

## MCA

For the MCA aneurysm, simulations have been done on three different underlying grid resolutions. The masking functions at the three different resolutions are shown in figure 3.9. These geometries have 15, 30 and 60 grid cells per diameter of the inflow vessel respectively. Similar to the PCOM case, steady flow has been imposed at the inlet. Since this aneurysm is located in the middle cerebral artery, realistic velocity of the flow is chosen as 0.30 m/s [61]. This flow was directed in the positive  $x$ -direction.

A first impression of the flow inside this geometry is shown in terms of the streamlines in figure 3.10. The streamlines that develop in this geometry at each resolution appear quite similar, as are the magnitudes of the velocity. The flow pattern is highly complex with re-circulations at various scales. This is qualitatively similar to the PCOM case and appears characteristic for laminar flow in aneurysms associated with bifurcating vessels. Subtle differences are present in the details

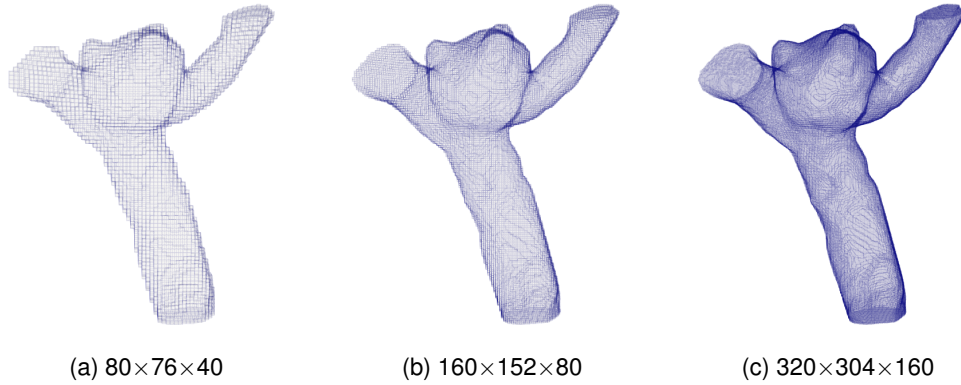


Figure 3.9: Different resolutions of the MCA aneurysm geometry, with respectively 15, 30 and 60 grid cells per diameter of the inflow vessel.

of these figures that are related to differences in the spatial resolutions that were adopted. To identify these variations, local flow patterns should be examined.

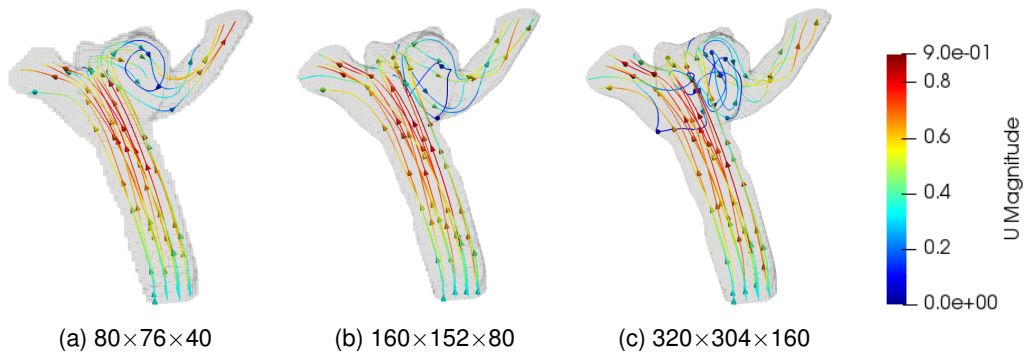


Figure 3.10: Streamlines in the steady state for increasing grid resolutions. Colours indicate the magnitude of the velocity along the streamline.

Figure 3.11 shows the  $y$ -component of the flow velocity in a cross-section inside the aneurysm. While the magnitudes of the velocity are in the same range, showing good similarity between the results obtained at the different resolutions, a patch of flow in the negative  $y$ -direction becomes visible in this cross section in the center of the aneurysm when using the two higher resolutions. This corresponds to a vortex that slightly changes shape as the underlying grid resolution increases. Overall, these and other 3D visualisations of the flow show that the dominant features are captured well on each of the three grids. Relevant differences are displayed in specific local details - quantifying the implications, if any, of such differences for clinical practice, remains an important challenge, which requires close collaboration with medical specialists and a study of many more patients.

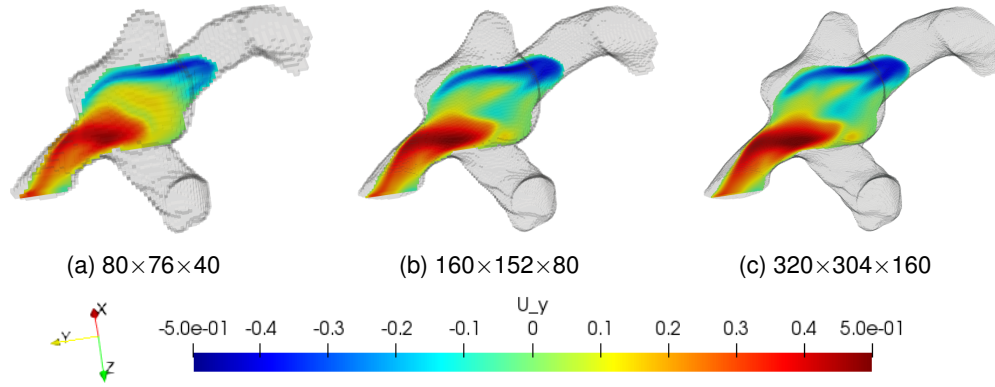


Figure 3.11:  $y$ -component of the flow velocity inside the aneurysm, for different underlying grid resolutions.

A number of qualitative and quantitative features of constant blood flow at varying grid resolutions has been studied for two aneurysm geometries. Qualitatively, the flow patterns are alike for all resolutions considered, showing only subtle differences in their shapes expressed in some very localized features. The simulations presented in this section are not realistic, since they concern steady blood flow. Realistic simulations are acquired when imposing a time-dependent boundary condition at the inlet, i.e. the pulsating heart given in figure 2.7. These simulations will be analyzed in the next section.

### 3.3 Pulsatile flow in aneurysm geometries

In the previous section, steady flow was simulated through the two bifurcating aneurysm geometries at increasing underlying resolution. For further analysis of the fluid dynamics inside the aneurysms, flow fields resulting from pulsatile conditions are used. The time-dependent mass flow rate was shown in figure 2.7. This particular profile was used for the PCOM geometry. Inlet conditions were imposed as a velocity based on the mass-flow rate by division by the area of the inflow vessel. For analysis of the PCOM aneurysm, the flow will be assessed at four characteristic moments in the cardiac cycle: peak systole, end systole, peak diastole and end of diastole, as shown in figure 3.12.

#### PCOM

The pulsatile profile, i.e., in figure 3.12, has been used as a boundary condition in flow simulation through the PCOM geometry, for the duration of multiple cardiac cycles. The steady flow simulation from the previous section served as an initial condition. Cross sections of the flow inside the aneurysm sac for the different resolutions are depicted in figure 3.13. These figures show the evolution of the inflow jet at different moments in time for pulsatile flow. This extends the earlier steady jet as depicted in figure 3.6. At peak systole ( $t_1$ ), the jet attains its maximum velocity. A relatively high velocity is attained near the wall in the resolutions  $100 \times 90 \times 120$  and  $200 \times 180 \times 240$ . During the remaining part of the cardiac cycle, the velocity of the inflow decreases and correspondingly, the velocity of the jet is lower compared to peak systole. A local maximum in the velocity is seen at peak diastole at time  $t_3$ .

The magnitudes of the velocities for the different resolutions of the PCOM geometry are similar at each moment in time. Also the qualitative features of the impinging jets are similar for the different resolutions showing that each of these resolutions is suitable for a general flow assessment. As with the steady flow simulations, the coarsest grid, however, is not able to capture the more

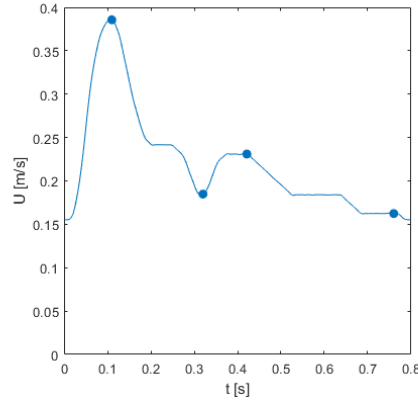


Figure 3.12: Pulsatile profile of the cardiac cycle, with indication of characteristic moments, from left to right:  $t_1 = 0.11$  s,  $t_2 = 0.32$  s,  $t_3 = 0.42$  s,  $t_4 = 0.76$  s. Representing respectively peak systole, end systole, peak diastole and end of diastole.

detailed patterns in the flow dynamics. For example, the shape of the jet at  $t_3$  is longer for the  $100 \times 90 \times 120$  and  $200 \times 180 \times 240$  resolutions, but appears shorter and weaker for the  $50 \times 45 \times 60$  resolution. Further analysis of possible clinical implications of such small-scale features is highly necessary to understand which spatial resolution is needed to reliably support medical diagnosis.

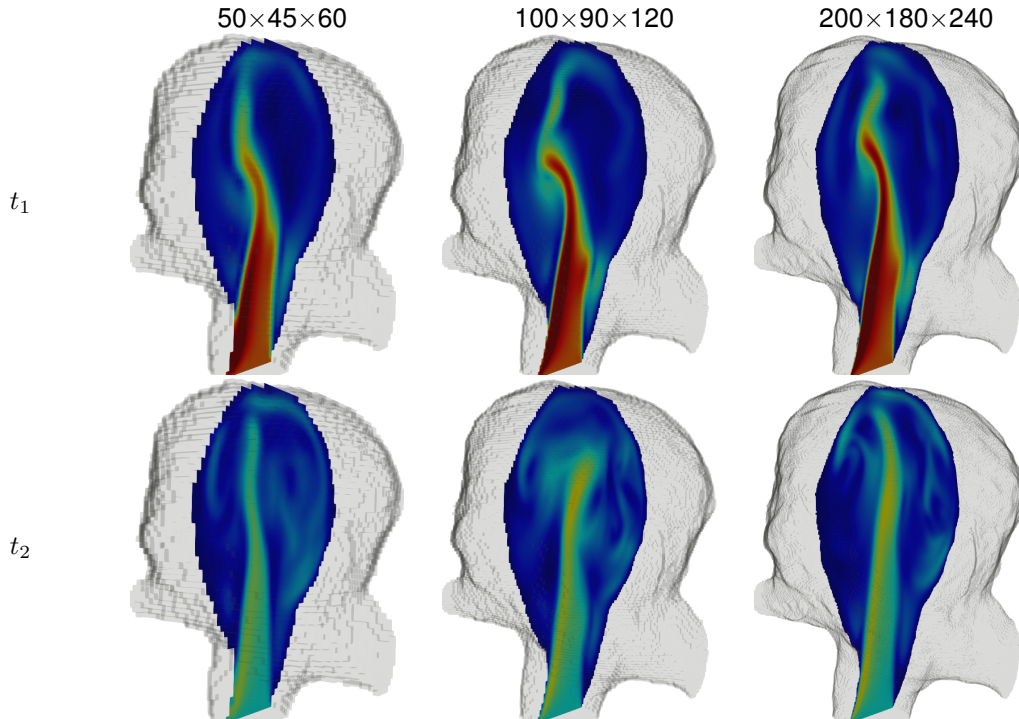


Figure 3.13: Pulsatile flow at different moments in the cardiac cycle for varying resolutions of the PCOM geometry, at  $z = 0.0084$  m. The magnitude of the velocity is shown at  $t_1 = 0.11$  s,  $t_2 = 0.32$  s,  $t_3 = 0.42$  s,  $t_4 = 0.76$  s, representing respectively peak systole, end systole, peak diastole and end of diastole. (Continues on next page)



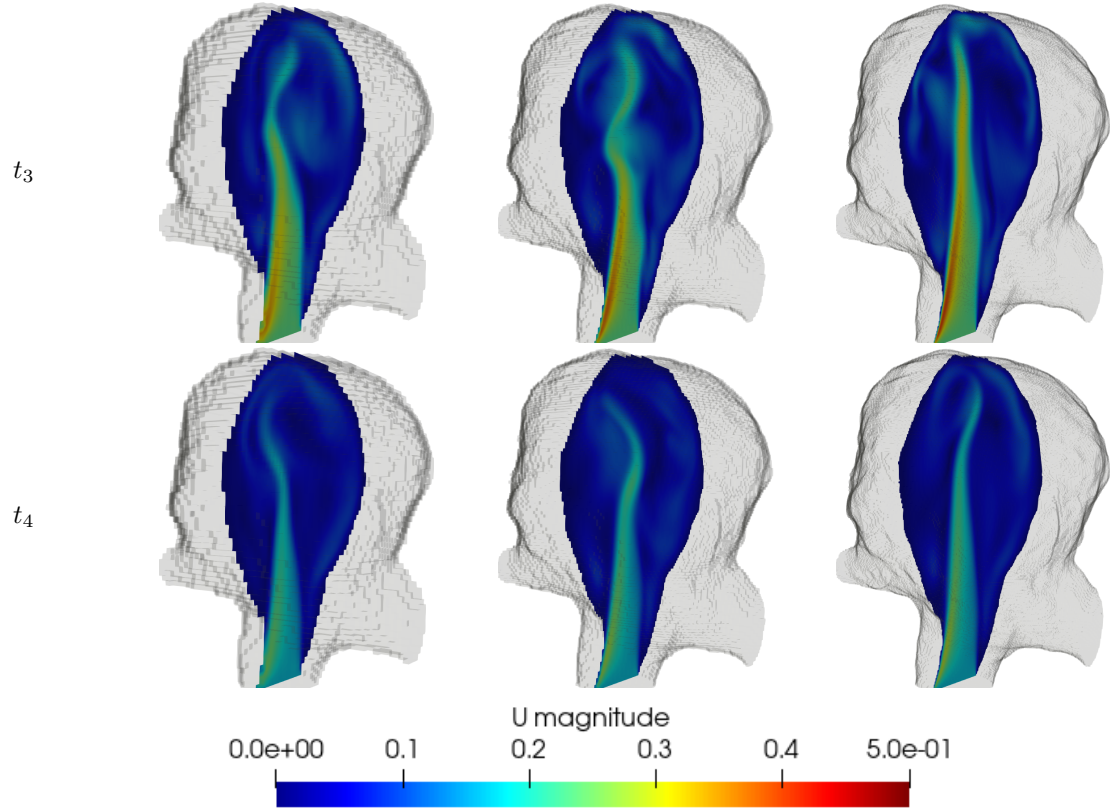


Figure 3.13: Pulsatile flow at different moments in the cardiac cycle for varying resolutions of the PCOM geometry, at  $z = 0.0084$  m. The magnitude of the velocity is shown at  $t_1 = 0.11$  s,  $t_2 = 0.32$  s,  $t_3 = 0.42$  s,  $t_4 = 0.76$  s, representing respectively peak systole, end systole, peak diastole and end of diastole.

Similar to the steady simulations of the PCOM aneurysm, the kinetic energy has been determined for the different resolutions of the pulsatile simulation. The plot in figure 3.14 shows the development of this quantity over the course of two cardiac cycles. The two cardiac cycles considered here are the second and third complete cycles in the simulation, where the steady state flow of previous section was used as an initial condition. Therefore, effects of stable initial conditions are no longer present here. Note that, unlike the plots for the steady simulation in figure 3.8, the quantities do not fluctuate aperiodically but show a clear imprint of the cardiac cycle. The energy of the two finest resolutions remain at a closer distance than the coarsest resolution. This implies that the resolution of 24 grid cells per diameter, i.e., at  $100 \times 90 \times 120$  resolution, gives a decent impression of the flow pattern globally. This would be good news for the computational costs since this resolution comes at a smaller cost than the finer resolution. In fact, the typical wall clock time per cardiac cycle at the  $200 \times 180 \times 240$  resolution is about 5 hours, while at the coarsened resolution this time reduces to roughly 30 minutes. Simulation of pulsatile blood flow through the PCOM geometry with a resolution of  $50 \times 45 \times 60$  grid cells takes approximately 2.5 minutes per cardiac cycle. While this is a considerable decrease in computational time, this resolution might not be able to capture the details of the flow field sufficiently and therefore requires additional research.

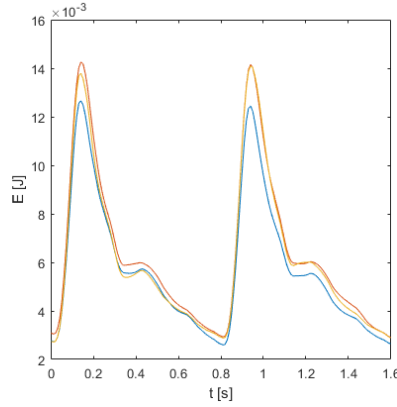


Figure 3.14: Average kinetic energy in the PCOM geometry for two cardiac cycles in different grid resolutions. Blue:  $50 \times 45 \times 60$ , orange:  $100 \times 90 \times 120$  and yellow:  $200 \times 180 \times 240$ .

### MCA

A pulsatile simulation has been done for the MCA geometry as well. The inlet condition shown in figure 3.12 was rescaled to an observed mass flow rate in the middle cerebral artery [61]. In fact, the mass flow rate as used in the PCOM geometry was multiplied by a factor 1.36 to reflect the MCA conditions more precisely. The steady state velocity field presented in section 3.2. To avoid influence from the stable initial conditions, the flow fields from the second completed cardiac cycle are analyzed. The  $x$ -component of the velocity in a number of locations in varying resolutions of the MCA geometry are given in figure 3.15. At locations 1 and 2, which are located ahead of the aneurysm, the inflow pulsatile profile is easily recognized. Moreover, the velocity profiles are close for the different resolutions. This is also true for location 3: even though it is located inside the aneurysm sac, the local velocity profile still follows the initial profile, with a slightly smaller magnitude. Locations 4 and 5 are inside the aneurysm sac, where the flow shows complex patterns. More variation is seen in the velocity profiles for different resolutions at these two locations, which is consistent with the higher local derivatives of the velocity components in this area. In places with more delicate localized flow patterns, the profiles show more variation among the resolutions. As we proceed through the flow domain, simulation errors appear to accumulate, leading to some variation of the predictions also just downstream of the aneurysm. This is illustrated with location 7, where the plots show a lot of variation. In fact, the streamlines passing the bifurcating vessel near point 7, move along the complex flow field inside the aneurysm just prior to passing near point 7. Discretization errors also have an influence near this area, before the flow can return to the more typical pulsatile flow in a healthy vessel further downstream. Finally, it should be noted that the profiles of the coarsest resolution deviate from the two finer resolutions in all seven locations. The yellow and orange lines stay closely together almost everywhere, implying similar local flow patterns for these two resolutions. The blue line follows the course of the other two lines at a distance. This further confirms the observation from the previous section: the coarsest resolution results in a decent flow field, but detailed patterns are only revealed at the higher resolutions. More specifically, we notice that the middle and highest resolution correspond to 30 and 60 grid cells per diameter of the inflow vessel, which complies closely to what was observed earlier in the PCOM case.

Based on the computational analysis in this subsection, it can be concluded that variation of the grid resolution in both geometries has no drastic consequences for the resulting flow fields for the resolutions considered. Coarse resolutions, with 12-15 grid cells per diameter of the inflow vessel, result in quite accurate flow fields in terms of dominant flow structures and magnitude of solution components. Revealing more of the local details in the flow patterns comes at a high

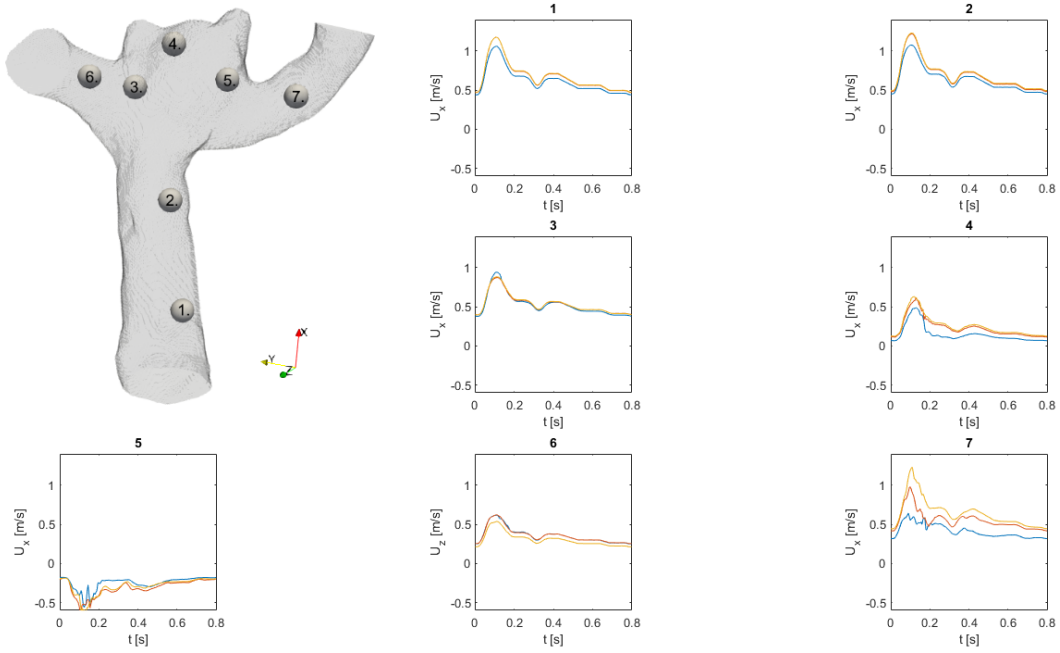


Figure 3.15: Flow profiles in streamwise direction for the duration of one cardiac cycle (0.8 s), at given locations using different resolutions of the MCA geometry. **Blue:**  $80 \times 76 \times 40$ , **orange:**  $160 \times 152 \times 80$  and **yellow:**  $320 \times 320 \times 160$ , for the second complete cardiac cycle.

computational cost, as it requires a higher underlying grid resolution. We observed that increasing the resolution twice and four times in each direction implied an increase in simulation time by a factor of 11 and 117, respectively. The assessment of the smaller details in the flow will depend considerably on the method used for this assessment. Many current methods are expected to be insensitive to the finer local flow features - we quantify this in more detail in the next chapter. However, as aneurysm risk is considered to accumulate from subtle features over long periods of time, also highly sensitive measures characterising also the local features of the flow are needed. A new approach in this direction involves the capturing of a bolus of 'contrast' inside the flow. This method was developed here to allow not only a qualitative flow representation but also to assess critical parameters such as which parts of the domain are affected most by the flow and what is a typical residence time over which such effects can accumulate. The details of the numerical method for analyzing time-dependent flow fields in this way will be presented in the next section.

### 3.4 Particle simulations

In this section, a method for Lagrangian particle tracking through the time-dependent flow fields in the aneurysm geometry will be presented. A bolus is a medical term used for a particle cloud, frequently used in medical imaging methods involving a contrast agent. The dispersion of the simulated bolus is based on the flow field resulting from the numerical simulations described in section 3.3. Performing such simulation is motivated by one of the main goals of this study: developing CFD to advise the neurosurgeon on a suitable treatment plan for a particular patient. The simulated bolus is similar to a magnetic radio angiography, which is performed by the neurosurgeon before and after treatment. The dynamics of the contrast fluid in the real patient gives an impression of the alterations in the flow resulting from the treatment - this information is among



the very few direct assessment methods available to the surgeon to quantify the effectiveness of the procedure. A main drawback of this assessment is that the patient undergoes treatment first. In challenging cases, however, it is not known in advance whether treatment will be successful. Analysis of the virtual bolus can therefore be an important addition to the tool-set available to the surgeon and should indicate whether a particular treatment, i.e., particular flow-diverting device, particular flexibility of the device, particular location, etc., suits a particular patient. This virtual bolus analysis enables the neurosurgeon to infer the effect of the opted treatment before execution.

The virtual bolus can be used to visualize flow fields with temporal dependence. This is the case in the flow fields considered in this study, which involve pulsatile boundary conditions. In addition to a three-dimensional flow field defined on a three-dimensional space, a temporal dependence is included, which makes it very difficult to analyze and distinguish global and local patterns. Since the particles follow the flow field that depends on both space and time, they connect the spatial and temporal dependencies.

The particles in this model are assumed to be non-interacting and massless, which implies their movement is not influenced by inertia. The displacement of an arbitrary particle is described by the following first order differential equation:

$$\frac{d\vec{x}}{dt} = \vec{U}(\vec{x}(t), t), \quad (3.3)$$

where  $\vec{x}$  represents the location of the particle in 3D space, and  $\vec{U}$  is the local velocity at  $\vec{x}$  at time  $t$ . In the algorithm, this equation is solved using an Euler forward scheme:

$$\vec{x}_{n+1} = \vec{x}_n + \Delta t \cdot \vec{U}_n(\vec{x}_n) \quad (3.4)$$

in which  $\vec{U}_n(\vec{x}_n)$  is the local velocity at location  $\vec{x}_n$  at the  $n^{\text{th}}$  time step. The size of the time steps,  $\Delta t$ , depends on the CFL condition, which requires  $\frac{\vec{U} \Delta t}{\Delta x} < 1$ . This condition ensures that information does not move faster through the grid than we can calculate - in this case meaning that particles can move the length of a single cell per time step at maximum. Since the velocity field is time-dependent, the time step is chosen to be time-dependent as well. After each update of the underlying velocity field, the maximum  $\Delta t$  permitted by the CFL condition is determined. This favours computational efficiency, since at times the velocity field has smaller magnitudes, we can now take larger time-steps.

At the beginning of the bolus simulation, particles are randomly sampled at the inlet. Determining their local velocity  $\vec{U}_0(\vec{x}_0)$  is nontrivial. In the numerical simulations, flow velocity is solved at the centers of each grid cell. The velocities of particles at an arbitrary point can be determined by interpolation methods of varying order. In this study, we consider piecewise constant and trilinear spatial interpolation. These interpolations are of order 0 and 1 respectively. Higher order interpolation methods were not considered, since those can induce problems near the walls because they do not preserve the sign of the solution after interpolation. The differences between the two interpolation methods for the algorithm are investigated in more detail in appendix B for flow through a straight pipe. It appears that trilinear interpolation is more robust against grid resolution and different types of discretization than piecewise constant interpolation. Algorithmic details of the bolus simulation will be covered next.

Nonzero velocities near the solid-fluid interfaces of the geometry occur frequently in the immersed boundary method [18], which can result in particles crossing the solid-fluid interface. This is a physically inexplicable scenario. A first algorithm has been implemented, that uses the explicit scheme to calculate the particle trajectories. Pseudo-code of this algorithm is shown below. Particles that are outside the fluid domain are removed from the bolus and the simulation continues with the remaining particles. Note that the removed particles also include particles that departed

the geometry via an outlet. This is the only physically acceptable way for a particle to end up outside  $\Omega_F$ .

---

**Algorithm 1** Basic particle simulation

---

```

1: Initialize cloud
2: while time < end time do
3:   Import up-to-date velocity field  $\vec{U}_n$ 
4:   Determine  $\Delta t$ 
5:   cloud new = cloud +  $\Delta t \cdot \vec{U}_n(\textit{cloud})$ 
6:   for particle  $\in$  cloud new do
7:     if particle  $\notin \Omega_F$  then:
8:       Remove particle from cloud
9:     else
10:      Determine new local velocity of particle
11:    end if
12:  end for
13:  Save locations, index and velocity of each particle
14:  cloud = cloud new
15:  time = time +  $\Delta t$ 
16: end while

```

---

This algorithm was tested on the aneurysm geometries shown in figure 2.4. The number of particles disappearing through the wall was rather high, with numerical losses of up to 20%. One could wonder why so many particles get so close to the wall. Often, a so called impinging jet is present in an aneurysm [15]. Particles are carried along such a jet, approach the wall and eventually may cross it as a result of numerical discretization errors. To resolve this issue, the basic algorithm was improved such that the number of particles that leave  $\Omega_F$  via the wall is kept at a minimum.

Handling the particles near the solid-fluid interface of an immersed boundary geometry is also addressed by Ghazaryan et al. in [18]. This study features interpolation of the flow field in boundary cells to resolve the nonzero velocity problem near the wall. This ensures particles cannot reach the solid-fluid interface. In our method, the underlying velocity field will remain unchanged. That means that particles can still reach the boundary of the fluid domain where we allow them to collide with the wall. We treat these collisions as elastic to retain some of the physics of near wall motion of particles. The main aspects are discussed next.

The main workflow of the improved algorithm is shown in figure 3.16. A major improvement of this algorithm is that particles are, in principle, only removed from the bolus if they leave the geometry via an outlet. If the updated particle trajectory incorrectly crossed a solid-fluid interface because of numerical error, the updated position is subsequently corrected. Checking whether a particle has crossed this interface is a two-step process. First, from the location of the particle, the corresponding grid cell is determined. All grid-cells and corresponding values of the masking function are stored in a three-dimensional matrix, from which we can see if the particle remained inside the fluid domain. If this is not the case, the wall collision function corrects the position of the particle, by reflecting its movement in the direction normal to the wall the particle just ran into, for the remainder of the time-step. The corrected newly determined position of the particle should be located in  $\Omega_F$  and the particle remains part of the bolus. Through testing, one exception was found for which this algorithm dysfunctions; a particle collides with a wall of a different cell after correction of its position, within the same time-step. This can be mostly prevented by decreasing the CFL number to 0.25-0.5, allowing only small movement of the particles in each time-step. This does increase the computational time, however the computational time of the particle simu-

lations is in the order of minutes and therefore small compared to the time required for the flow simulations. Doing so, it was observed that 0-0.5% of particles could not be corrected after a wall collision, and therefore disappeared from the bolus. This is a great improvement compared to the first implementation; this small fraction minimally affects the main dynamics of the bolus.

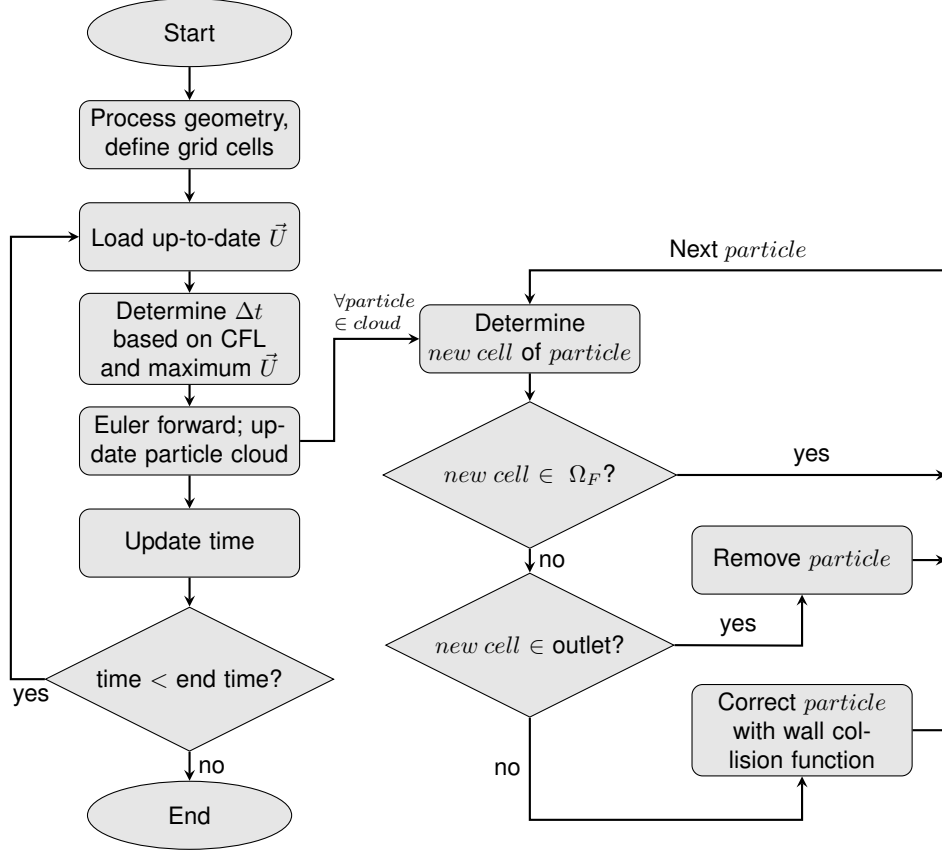


Figure 3.16: Flow chart of the particle tracer algorithm with wall collisions, for time-dependent particle simulations. This algorithm works as post-processing of a CFD simulation and was implemented in Matlab.

The improved algorithm has been used for simulating a bolus through the MCA geometry. The resulting bolus at a few chosen moments in time, showing the main features of the dispersion of this bolus can be seen in figure 3.17. As described, initial conditions of the bolus are a uniformly distributed ‘slice’ of particles at the beginning of the inflow vessel, as seen at  $t_1 = 0$  s. At the moment of entering the aneurysm ( $t_2 = 0.032$  s), the particles are mainly present in the left half of the aneurysm sac. It also becomes clear that the main vortex inside the aneurysm is directed clockwise. At  $t_3 = 0.045$  s, some particles have already left the geometry via the left vessel, while no particles are present in the right curved vessel. In fact, particles leave via the right bifurcating vessel only after having visited the aneurysm sac first. This becomes evident when looking at the bolus at  $t_4 = 0.06$  s. Most particles are then present at the right curved vessel. These particles have been expelled by the pulsatile changes in the vortex inside the aneurysm and depart via the vessel on the right. Finally, some particles did not arrive at the aneurysm sac yet, but move very slowly through the inlet vessel. All of these particles are located initially very near the vessel wall, where local velocity is low due to the no-slip condition imposed there.

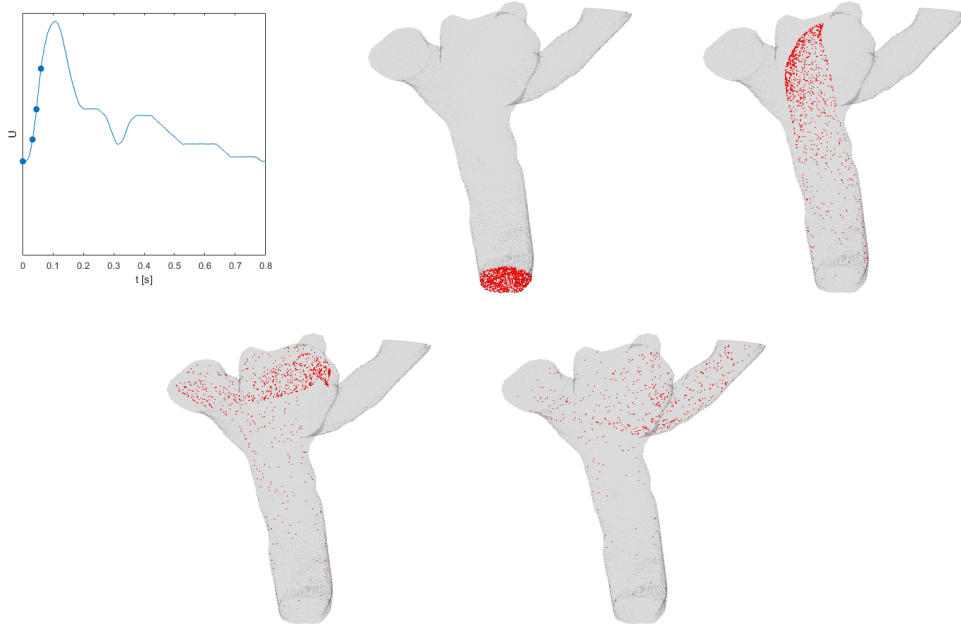


Figure 3.17: Snapshots of the virtual bolus at moments in the cardiac cycle indicated in the plot in the top left ( $t_1 = 0$  s,  $t_2 = 0.032$  s,  $t_3 = 0.045$  s,  $t_4 = 0.06$  s).

The bolus as defined in this section will play an important role in the process of extracting useful information for decision support from the CFD simulations of the aneurysm. This approach will be motivated and described in detail in section 4.2. For this method, it is required that all particles that are generated at the inlet, correctly reach the aneurysm neck. Due to the no-slip conditions on the vessel walls, particles can get stuck nearby which can lead to rather large variations in the residence times of the particles in the flow domain. A test case with steady Poiseuille flow formed a very educational test case, since this case has an analytical solution. Validation of this algorithm was done using the analytical solution, this is covered in more detail in appendix A. Main findings were that if particles are placed at a small distance from the wall, residence times of particles inside the geometry show smaller variation.

A second test case was done in a realistic aneurysm geometry, the inflow vessel of the Portugal geometry, i.e., figure 2.4a. The bolus was simulated in pulsatile flow conditions. This has been done for two resolutions of the Portugal geometry: 50 and 25 grid cells per diameter of the inflow vessel. A cloud of uniformly distributed particles was released at the inlet at  $t = 0$  s, and their positions were determined for the course of one cardiac cycle (0.8 s). A cross-section of the vessel prior to the aneurysm opening was taken as a reference section, as shown in figure 3.18. The particles passing this reference section as a function of time will be of interest in this test case. Local velocity of the particles have been determined using piecewise constant and trilinear interpolation, to see the effect of the different interpolation methods on a realistic vessel geometry. The geometry considered here does not contain any bifurcations, hence 100% of the particles released at the inlet, should eventually pass the reference section. The fraction of particles passing this section as a function of time for the four simulations is shown in figure 3.18. The biggest impact of different interpolation methods is seen in the grid with the lower resolution. In the simulation with piecewise constant interpolation, 93.8% of particles passed the reference section at  $t = 0.8$  s. In the simulation with trilinear interpolation, this amounts to 99.4%. As opposed to the Poiseuille case, the shapes of the curves in figure 3.18 do not show evident numerical artefacts, as seen in figure B.2 in appendix B. This is related to the fact that particles

move through regions of different local velocity in the course of time, instead of staying in a well-defined circle of constant velocity throughout the entire simulation, as in the Poiseuille case. The effect of the different interpolation methods is even less obvious in the simulations with higher resolution. The improvement of trilinear interpolation over piecewise constant interpolation was slightly more than 2%-point in this case.

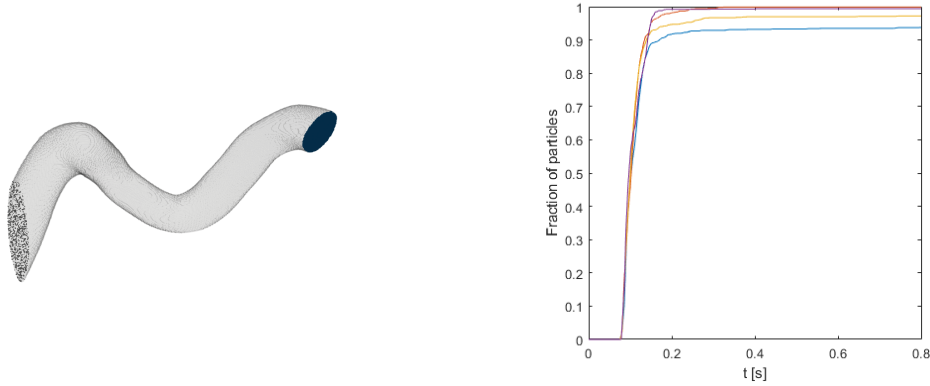


Figure 3.18: Left: serpentine piece of blood vessel. Particles are released at the inlet and eventually cross the [reference section](#) shown on the right. Right: Fraction of particles passing the reference section as a function of time for one cardiac cycle. [Blue](#): 25 grid cells per diameter, [piecewise constant interpolation](#), [purple](#): 25 grid cells per diameter, [trilinear interpolation](#), [yellow](#): 50 grid cells per diameter, [piecewise constant interpolation](#) and [orange](#): 50 grid cells per diameter, [trilinear interpolation](#).

From the test cases, we can conclude that trilinear interpolation decreases the variance in Lagrangian particle tracking between different grid resolutions. However, this comes at a price. In the current implementations, piecewise constant Lagrangian particle tracking for a single cardiac cycle can be done in roughly 5-10 minutes, whereas trilinear interpolation takes more than an hour. In fluid simulations done at high resolutions, the benefit of trilinear over piecewise constant interpolation is rather small, and might not be worth the extra computational time. It was decided to use the piecewise constant interpolation for the Lagrangian particle tracking for the remainder of this study, since the flow in realistic geometries does not lead to the Poiseuille type artefacts for piecewise constant interpolation.

In this chapter it was described how blood flow dynamics through an aneurysm geometry can be simulated under realistic conditions. Also, the quality of these flow simulations at different grid resolutions has been investigated. It was found that a typical resolution of 24-30 grid cells per diameter of the inlet vessel was adequate to represent the main flow features. In cases where small-scale details are relevant, higher resolutions (and costs) are needed, motivating even resolutions of up to 48-60 grid cells per diameter at a 10-16 times higher computational cost. An algorithm for Lagrangian particle tracking of a so-called bolus was introduced, and also assessed for a pair of test cases. These two simulations result in a large amount of data: a three dimensional velocity field, with temporal component, and an enormous collection of particle locations over time. In the next chapter a proposal is given how useful information for decision support can be extracted from this data.

## Chapter 4

# Towards numerical decision support for aneurysm treatment

In previous chapters, the pathway from patient data to computational fluid dynamics was described. This pathway leads to time-dependent, three-dimensional velocity fields and a large amount of data describing the dispersion of the bolus through the aneurysm geometry. To assist the neurosurgeon in finding a suitable treatment for a particular patient, relevant information should be extracted from these fields and the virtual bolus. Ideally, one wants to reduce the amount of information to the bare essentials relevant for medical decisions regarding possible treatment. In this process one should not reduce too vigorously and aim for just a few characteristic numbers, often referred to as ‘indices’ or ‘grades’ in the literature [20, 25, 44, 47]. This may be an oversimplification that does not describe the complexity of the problem in sufficient detail. Likewise, it also does not help a surgeon if no significant data-reduction is achieved. This illustrates a trade-off that needs careful consideration: only relevant information should be concisely presented. Moreover, a degree of uncertainty is implicit in the CFD predictions, which needs to be quantified as well. Finding a proper balance between these considerations will involve a process of interactions between medical experts and mathematical modellers. We can begin to shape this process now that the pathway from patient data to CFD predictions can be made in considerable detail and generality using the methods outlined in previous chapters. A first proposal is specified in this chapter and applied to a side-wall aneurysm, as well as to a case of a more challenging bifurcation aneurysm in the next chapter.

The notion of relevant information will be motivated by referring to existing assessment methods for aneurysms, which is subject of section 4.1. Implementation of these methods based on the outcomes of CFD simulations will be covered in section 4.2. In section 4.3, this newly proposed analysis method will be applied to the Portugal geometry, i.e., the geometry given in figure 2.4a. Moreover, the effect of a possible treatment will be shown in this section. This chapter will be concluded by assessment of robustness and reproducibility of the proposed method in section 4.4.

### 4.1 Existing methods

Many proposals for the assessment of aneurysms are currently available. We distinguish qualitative and quantitative methods. Qualitative methods are scores based on visual classification of an MRA of the aneurysm and therefore more used in clinical settings. The quantitative grading scales are based on CFD simulations and therefore mainly used by mathematical modellers and fluid mechanics specialists. These approaches include quantities that are believed to influence the vessel wall, such as wall shear stress. Many other quantitative metrics are based on this wall shear stress. The main issue with the quantitative metrics, is that they do not provide information that is directly useful yet for the neurosurgeon, e.g., because the clinical relevance of a specific metric is not beyond doubt. In this section, we will motivate which assessment methods provide helpful information for assessment of the CFD simulations, emphasizing the relevance of a hybrid assessment in which both qualitative evaluation of the CFD data as well as more precise quan-

titative measures are combined. We believe that this combination is required to do justice to the complexity of individual cases and to explicitly include the medical expert in the analysis.

Over the years, many grading scales intended for use in clinical practice were proposed. One of the first published grading scales for measuring the effect of surgery was the Raymond-Roy score [51]. The grade is determined based on an angiography, performed by the neurosurgeon after treatment to assess its effect on flow dynamics. The Raymond-Roy scale is a simple three-point grading scale, that indicates the so-called degree of filling of the aneurysm. In the medical world, this measure is loosely defined and indicates the dispersion of the contrast fluid inside the aneurysm sac. In the Raymond-Roy scale, three different levels of degree of filling are distinguished: no contrast fluid inside the aneurysm sac, a small amount of contrast fluid in the neck of the aneurysm or complete filling of the aneurysm sac by the contrast agent. In terms of flow dynamics, it can be interpreted as some part of the fluid following the course of the parent vessel, and the remaining part taking a detour through the aneurysm sac. This score was used when performing treatment by clipping or coiling, which should, for a successful outcome of the treatment, decrease the degree of filling. However, with the rise of flow diverting treatment, it became inadequate, since it is not uncommon to have a residual flow inside the aneurysm sac immediately after a flow diverter has been deployed successfully [44]. Therefore, O'Kelly et al. proposed the OKM scale, an extension of the Raymond-Roy scale, meant to be more suitable for assessment of flow diverting treatment. Besides the degree of filling, another feature referred to as the degree of stasis is measured. This is another loosely defined quantity in the medical world, representing deceleration of the flow inside the aneurysm sac compared to the blood inside the parent vessel. The OKM scale awards three different scores for the degree of stasis, depending on the location of contrast agent that followed the parent vessel while contrast fluid remains present in the aneurysm sac. Together with the degree of filling, this measure accounts for the score awarded by the OKM scale, and is illustrated by figure 4.1. In terms of fluid dynamics, this measure can be thought of as the residence time of the fraction of blood flow staying inside the aneurysm sac. The measures related to degree of filling and degree of stasis will be defined in terms of the virtual bolus in section 4.2.

Apart from the OKM scale, various other aspects of the angiography can be taken into account to establish a possible grade. A few examples are: narrowing of the parent artery [25], shape of the occluded part of the aneurysm [20], but also general aspects such as presence of a side branch, age of the patient and size of the aneurysm [47]. The determined grades should reflect the chances of a successful intervention, or risk of possible rupture. This matter was examined by Raper et al. in [49]. For multiple grading scales it was shown that there was no significant correlation between the score after treatment and the success of the treatment. This confirms that occlusion of aneurysms is a very involved process, depending on many factors which cannot be captured by a score based on an angiography alone. Moreover, basing a grade on angiographic data introduces intra- and inter observer variability. This appears to be an issue for a number of the proposed scales [33]. An assessment method that is informative, automated and which takes a range of aspects of the underlying fluid dynamics into account should be developed in order to resolve these issues.

Quantitative measures are based on parameters that characterize the flow and forces involving the vessel wall, that forms the load bearing structure of the aneurysm geometry. These quantities are based on the outcomes of numerical simulations, hence they leave no room for inter observer variability and can be made genuinely objective. This type of measures is closely connected to fluid-mechanical aspects of the flow that develops in the vessel geometry. We review some of these proposals next.

Wall shear stress (WSS) is a hemodynamic parameter, believed to influence the state of endothelial cells in the vessel walls directly [55]. It is a measure for the hemodynamic force on the vessel walls, exerted by the viscosity of the blood flowing past it. Since blood is considered a Newtonian











OKM SCALE FOR FLOW DIVERSION			
	1 Arterial	2 Capillary	3 Venous
A Total filling			
B Subtotal filling			
C Entry remnant			
D No filling			
<div style="display: flex; justify-content: space-between; align-items: center;"> <span>Angiogram run start</span> <span>Angiogram run complete</span> </div>			

Figure 4.1: Matrix representing the OKM grading scale, different degrees of filling are shown in the rows and are awarded with a score of A,B,C or D. Degree of stasis is illustrated in the different columns and obtains a score of 1, 2 or 3 [44].

and incompressible fluid, the wall shear stress of flow along a wall is directly proportional to the viscosity and the gradient of the velocity in the direction normal to the wall. In this study, the wall shear stress was determined using OpenFOAM [2], where it is defined as follows:

$$\vec{\tau}(\vec{x}, t) = \mu (\mathbf{R} \cdot \vec{n}) = \mu \left( \frac{1}{2} (\nabla \vec{u} + \nabla \vec{u}^T) \cdot \vec{n} \right) \quad (4.1)$$

where the dependence of  $\vec{u}$  on  $\vec{x}$  and  $t$  is omitted for clarity. The matrix  $\mathbf{R}$  is the symmetric shear tensor, that is constructed from  $\nabla \vec{u}$ , the Jacobian of  $\vec{u}$ . Furthermore,  $\mu$  is the dynamic viscosity, and  $\vec{n}$  is the local unit normal vector, perpendicular to the wall. Shear stress is given in Pa, the commonly used unit for pressure.

Direct clinical consequences of wall shear stress on aneurysm growth and rupture remain much disputed. Both high and low wall shear stress have been related to rupture [55]. Wall shear stress was determined for a number of aneurysms by Jou et al. in [24]. It was shown that the maximum wall shear stresses of ruptured and unruptured aneurysms were of similar order. A significant difference was seen in low wall shear area of the aneurysm in case of rupture. This measure is defined as the fraction of the aneurysm area with a wall shear stress lower than 10% compared to the mean stress in the parent artery [24]. This difference was also evident in [60], where parameters indicating rupture were examined. This example illustrates that the development of fluid-mechanical insights into measures that may have clinical relevance requires careful statistical analysis of many patient-specific cases, i.e., a close collaboration between the mathematical modelling efforts and the clinical context.



Based on the wall shear stress, there are many derived quantities that can be calculated. For example the wall shear stress gradient, that represents the spatial derivative of the wall shear stress was suggested in [34]. In the study of Xiang et al., it appeared that this quantity failed to distinguish ruptured from unruptured aneurysms [60].

The wall shear stress does not specifically reflect the pulsatile character of the flow and possible directional dynamics during a cardiac cycle. In order to account for this aspect, the oscillatory shear index (OSI) was first introduced by Ku et al. [29]. When simulating pulsatile flow through an artery, it appeared that in some places, the direction of the wall shear stress changed throughout a cardiac cycle. This phenomenon is measured by the OSI, which is defined as [32]:

$$\text{OSI}(\vec{x}) = \frac{1}{2} \left( 1 - \frac{\left| \int_0^T \vec{\tau}(\vec{x}, t) dt \right|}{\int_0^T |\vec{\tau}(\vec{x}, t)| dt} \right) \quad (4.2)$$

As becomes clear from this definition, OSI ranges between 0 and 0.5. It is defined at each location on the vessel wall;  $\vec{\tau}(\vec{x}, t)$  represents the WSS in a specific location at a given time. OSI represents the shear stress acting on the vascular wall due to WSS in directions other than the time-averaged WSS. An OSI of 0 at a given location implies that the WSS points in the same direction throughout the cardiac cycle, whereas an OSI of 0.5 indicates a lot of change in direction of the WSS. Note that, in contrast to the WSS, the OSI is integrated over some interval of time. In this study, we integrate over the duration of one cardiac cycle to determine the OSI, meaning that the OSI is not a time-dependent metric.

It is accepted that endothelial cells are not only sensitive to the magnitude of the wall shear stress, but also in fluctuations in the direction over time [32]. Hemodynamic forces acting on the vessel wall and changes thereof contribute to a process we refer to as remodelling. It is a constant interplay between changes in hemodynamics, and responses of endothelial cells lining the vessel walls, reshaping the blood vessel and trying to restore balance and return hemodynamic forces to their normal levels [34]. At some point, this process stabilizes, or reaches a point where the vessel walls can no longer bear the stresses and the aneurysm ruptures. A combination of low wall shear stress and high OSI was observed at the exact rupture site, for a patient-specific case where rupture occurred during an angiography [62]. Low wall shear stress was also observed in areas with large displacements of the vessel wall in [10]. In [60], OSI was also considered as an indicative measure for aneurysm rupture. It turned out that the ruptured aneurysms had larger OSI values than the unruptured aneurysms in this study.

Besides quantitative measures based on CFD, some qualitative metrics based on CFD simulations were explored by Cebal et al. in [15]. This study considered different types of flow configuration, based on complexity as well as different types of the wall impinging jet, and related them to the risk of rupture. It was found that, in particular, a small area of the wall being impinged by the jet is related to an increased rupture risk.

A few well-known quantitative hemodynamic parameters have been introduced. From previous studies, it appears that some of them are linked statistically to aneurysm rupture and could also be of some use for assessment of the geometries in this study [60]. The link between these parameters and clinical practice is, however, still largely missing, since precise threshold values are lacking and may even differ per patient. On the other hand, we mentioned some qualitative grading scales based on angiographic data. In several studies it was found that these are likely to be too simplified to give meaningful information of the flow dynamics or, ultimately, the clinical decision process. A combination of the two could well lead to a useful tool for advising the neurosurgeon, before executing an opted treatment. We consider such a hybrid approach in more

detail in the next section.

## 4.2 Proposal of novel assessment method

In the previous sections, currently available assessment methods have been described. The qualitative grading scales as described in section 4.1 have shown no significant correlation between successful intervention and score [49]. From this, we can conclude that thrombus formation inside the aneurysm sac is a very involved process that cannot be captured by a single or double axis score and therefore demands more delicate assessment. The procedure of this assessment that we propose here involves a more elaborate report rather than a single score and will be discussed in this section. The scores involved are not limited to the quantitative measures covered in the previous section. Some scores are based on the particle simulation through the aneurysm, introduced in section 3.4. Following this procedure, a detailed and nuanced impression of the patient's situation can be obtained to support the neurosurgeon.

CFD comes with a large amount of data, from which relevant information still needs to be extracted. A suitable assessment method is clear, complete and accessible for the neurosurgeon. To attain such an objective, part of the analysis is based on the virtual bolus. This represents an angiography, frequently performed by neurosurgeons. In contrast to angiographies, the virtual bolus can be analyzed quantitatively in detail. This results in very precise measures of the bolus, and therefore also of the flow dynamics inside the aneurysm. This virtual bolus assessment option was motivated by some of the concepts that suggested the OKM scale discussed in section 4.1. By making the bolus analysis quantitative based on CFD a new assessment option may be arrived at. Altogether, the scores based on analysis of this virtual bolus can be well interpreted by neurosurgeons, are more precise and have minimal human-caused variance compared to the grading methods described earlier. The procedure of analysing the virtual bolus is described in the remainder of this section and complements other quantitative measures such as WSS and OSI.

In the particle simulation, as described in section 3.4, a number of uniformly distributed particles is released simultaneously at the inlet of the geometry. Throughout the simulation, the locations and velocities of each particle are saved at each time step. Using the data of the particle locations over time, information about the dispersion of the particle cloud is extracted which can be translated into widely adopted factors such as the filling of the aneurysm sac and the degree of stasis. Other factors, such as shape of inflow jet are expected to also play a role in thrombus formation, but these are hard to extract from the locations of particles and are hence represented by other components of the assessment. Therefore, the analysis of the virtual bolus relies on numerically equivalent measures of the degree of stasis and the filling of the aneurysm.

As explained in section 4.1, the aneurysm sac can be perceived as an addition to the parent vessel. Part of the blood flowing through the parent vessel takes the 'detour' via the aneurysm sac, while the remaining part continues through the parent vessel, never entering the aneurysm. We will measure the fraction of the flow entering the aneurysm sac in terms of the virtual bolus, quantifying the main flow dynamics inside the vessel geometry. The percentage of particles visiting the aneurysm sac as a function of time can be viewed as a measure for the *degree of filling*. In fact, we will consider the division of the particles over different sections of the geometry as a function of time, giving a classification of the particles according to their locations. The sections divide the actual geometry into a few characteristic compartments, which are defined using a fixed protocol that we introduce later in this section. We distinguish instantaneous and cumulative visitation fractions of the virtual bolus for a section  $\Omega^*$  of the vessel geometry  $\Omega_F$ :

- **Instantaneous visitation fraction:** fraction of particles visiting  $\Omega^*$  at time  $t$ :

$$\text{Instantaneous}_{\Omega^*}(t) = \frac{1}{N} \sum_{i=1}^N f(\vec{x}_i(t)), \quad (4.3)$$

$$\text{where } f(\vec{x}_i(t)) = \begin{cases} 0 & \text{if } \vec{x}_i(t) \notin \Omega^* \\ 1 & \text{if } \vec{x}_i(t) \in \Omega^* \end{cases}$$

In which  $N$  is the number of particles in the bolus, and  $\vec{x}_i(t)$  is the location of particle  $i$  at time  $t$ .

- **Cumulative visitation fraction:** fraction of particles that have visited  $\Omega^*$  up until time  $t$ :

$$\text{Cumulative}_{\Omega^*}(t) = \frac{1}{N} \sum_{i=1}^N g(\vec{x}_i(t)), \quad (4.4)$$

$$\text{where } g(\vec{x}_i(t)) = \begin{cases} 0 & \text{if } \forall t^* \leq t : f(\vec{x}_i(t^*)) = 0 \\ 1 & \text{if } \exists t^* \leq t : f(\vec{x}_i(t^*)) = 1 \end{cases}$$

Note that by this definition, the cumulative visitation rate is an increasing function, since the functions  $g(x_i(t))$  is either a step function for particles that visited  $\Omega^*$ , or the zero function for particles that did not visit  $\Omega^*$  during the bolus simulation.

Next to the degree of filling, the *degree of stasis* is an important measure. Since in the aneurysms considered up until now, we observed a vortex inside the aneurysm sac with a low velocity compared to the flow in the parent vessel, blood passing the aneurysm sac undergoes a delay while residing there relative to the fraction of blood that passed without entering the aneurysm sac. We measure this delay in terms of the residence time:

- **Residence time:** average amount of time particles visiting section  $\Omega^*$  remain there:

$$\text{Residence time}_{\Omega^*} = \frac{\sum_{i=1}^N \int_0^T f(\vec{x}_i(t)) dt}{\sum_{i=1}^N g(\vec{x}_i(T))} \quad (4.5)$$

Where  $T$  is the total duration of the simulation, lasting one or several heart beats, depending on the flow rate of particles through the geometry.

Dividing the vessel geometry into separate sections should be handled using a fixed protocol. In this study we define this protocol for two classes of aneurysms, i.e., side-wall and bifurcation, shown schematically in figure 4.2. The partition reflects the main topology of the vessel structure, and distinguishes the inlet, connecting piece of parent vessel, aneurysm and outlet(s). The side-wall aneurysm has one outlet, forming a separate section, whereas the bifurcation aneurysm has two outlets, each forming a separate section. This procedure is shown for the Portugal and PCOM geometries in figure 4.3.

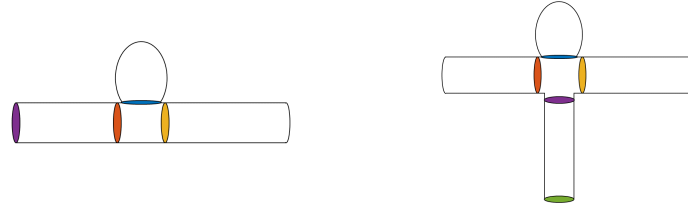


Figure 4.2: Protocol for division of a side-wall (left) and bifurcation aneurysm (right), dividing the geometry into inlet, connecting vessel, aneurysm and outlet(s).

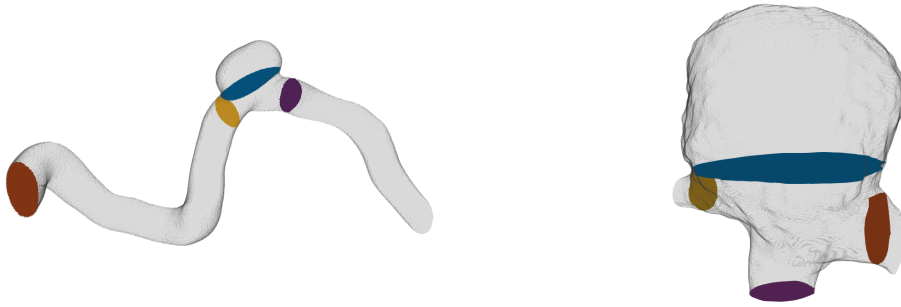


Figure 4.3: Division of the Portugal (left) and PCOM (right) geometries into separate sections, following the fixed protocol.

The instantaneous and cumulative visitation fractions as defined in equations 4.3 and 4.4 are determined for all sections considered, and used as a representation of the dispersion of the virtual bolus through the aneurysm geometry. This representation forms a precise, well defined measure which can replace for the degree of filling concept used intuitively in the medical world. The residence time is determined for the aneurysm section of the geometry. We consider this measure a numerical quantification for the degree of stasis as defined in the OKM scale. The residence time is particularly useful for quantification of the effectiveness of a possible treatment method, as we will see in section 4.3.

Simulation of the virtual bolus through the aneurysm geometry forms an accurate representation of the main flow characteristics. The majority of the particles released at the inlet, moves through the geometry, following the time-dependent velocity fields, and finally departs the vessel within a limited amount of time. A small fraction of particles might get stuck close to a vessel wall for extended periods of time due to the no-slip conditions imposed there. This affects a small portion of a real bolus of contrast fluid as well, but is not perceptible, and therefore not accounted for in grading scales relying on visual interpretation of the angiography. The effect of this is observed in the quantities defined for the numerical bolus, for example in the instantaneous visitation rates of the separate sections. Since our method is aimed at representing the main flow characteristics, reckoning this effect might be redundant. It can therefore be considered to place the particles at a small distance from the wall initially.

In this section, we introduced three different quantities based on the numerical bolus, that represent the main characteristics of the flow. In the next section, we determine these measures for the Portugal geometry, and assess the effects of employment of a flow diverting stent in this aneurysm.

### 4.3 Case study: Portugal geometry

In this section, the proposed assessment method will be used to quantify the effect of placing an eCLIPs stent in the Portugal geometry from figure 2.4a. An eCLIPs is a stent produced by Evasc [5]. This stent has a rib-like structure, and a non-circumferential design. Because of this design, it fits inside most blood vessels. Another property of the eCLIPs is that it does not block bifurcating vessels close to the aneurysm. The stent and how it is inserted in a blood vessel can be seen in figure 4.4. The purpose of this stent lies in stent-assisted coiling in wide-necked aneurysms. The porosity of this stent is very high, approximately 70% in the part covering the aneurysm neck [5]. Also, the wires in this stent are thick compared to the wires in conventional flow diverters. The wires of the eCLIPs are 0.06 mm, which is twice the thickness of wires in a typical flow diverter [45]. Moreover, the wires in flow diverters are braided in a helix-like shape. Even though the porosity of the eCLIPs is similar to those of typical flow diverters, which is in the range of 60-76% [8], the size of the pores is much larger. Therefore, the eCLIPs is not a suitable flow diverter on its own, but it will cause some changes in the flow field inside the Portugal geometry. This case will be used to illustrate the effectiveness of the assessment method introduced in section 4.2 in terms of quantifying differences in the flow field.

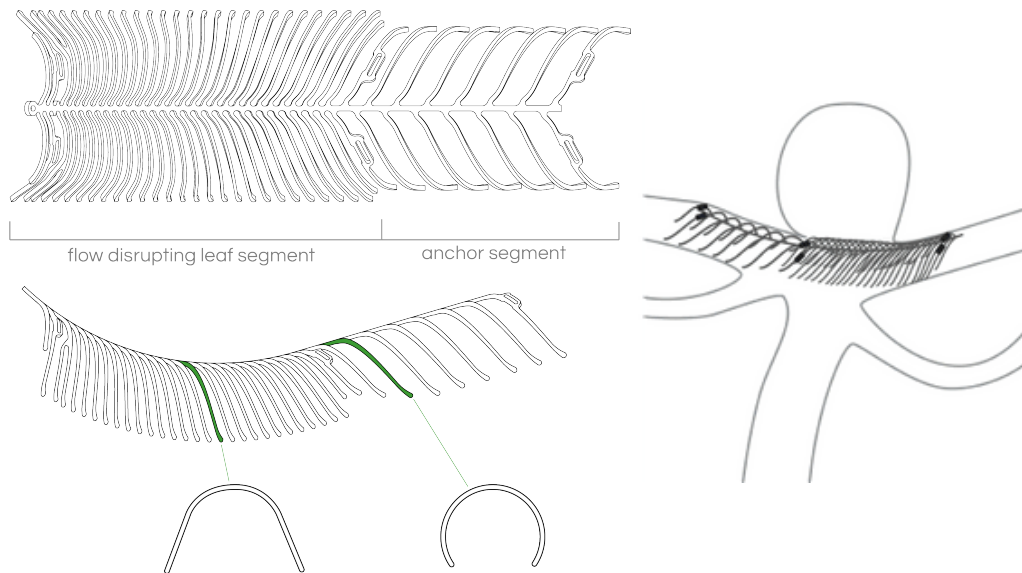


Figure 4.4: eCLIPs used for endovascular treatment of aneurysms [5].

To assess the effect of the eCLIPs on the flow inside the artery and aneurysm, two geometries were available. The geometries can be seen in figure 4.5; one of them features an eCLIPs, and the other does not. Both geometries have a resolution of  $352 \times 288 \times 256$  grid cells, which accounts for 50 grid cells per diameter of the inflow vessel on average. Compared to the two coarser resolutions of the PCOM and MCA aneurysms shown in section 3.2, this is a high resolution. Inserting the eCLIPs inside the geometry, introduces a relatively small length scale inside the geometry. The 'ribs' of the eCLIPs have a thickness of 0.06 mm, which is considerably smaller than the diameter of the Portugal diameter of 5.5 mm. The number of grid cells per wire diameter is less than one, implying this resolution is insufficient for resolving the structure of the eCLIPs entirely, as can also be seen in figure 4.5c. However, results from [45] show that this has a rather small impact on the overall flow field in the whole domain.

Both geometries shown in figure 4.5 have been simulated with pulsatile flow, with an average velocity of 20 cm/s. For successful simulation of pulsatile flow, first steady flow at this velocity

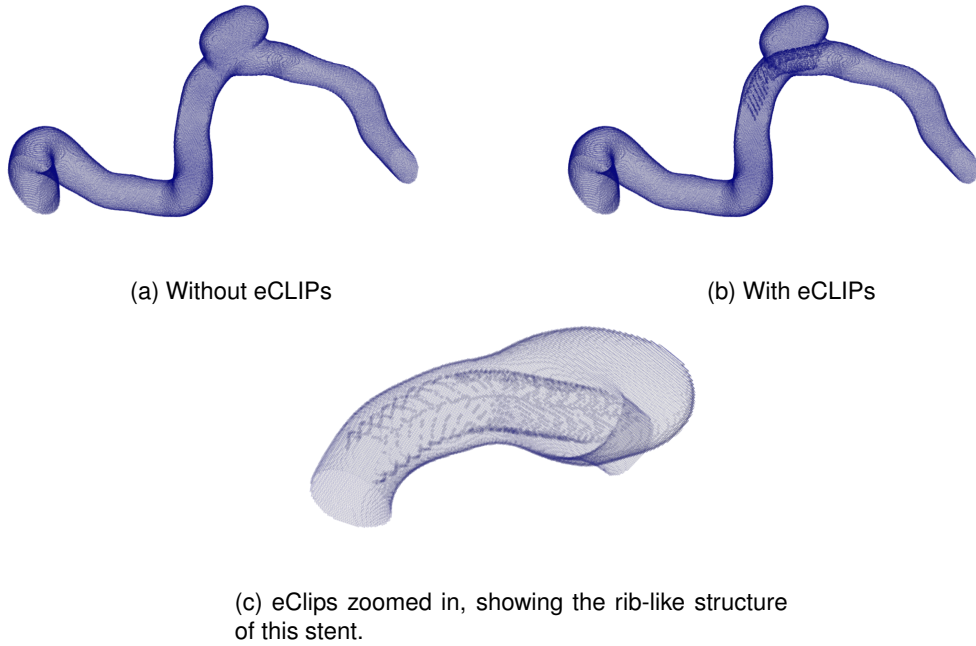


Figure 4.5: Immersed boundary geometries of the Portugal aneurysm

has been simulated through this geometry for the duration of 3 seconds. The acquired steady state flow was used as an initial condition for the pulsatile flow conditions. To get a first idea of the impact of the stent, the average velocity over one cardiac cycle in the neighbourhood of the aneurysm is given in figure 4.6. This image was acquired from the second complete cardiac cycle in the flow simulation, so the influence of the steady initial conditions is minimal. Both figures result from simulation with a resolution of 50 grid cells per diameter of the inflow vessel. From this figure it becomes clear that there are some subtle differences caused by the eCLIPs in the structure of the velocity field. The magnitude of the velocity remains roughly the same for both configurations. It can be seen that the flow tends to follow the course of the blood vessel more closely in the geometry with the eCLIPs indicating some flow-diversion induced by this device on its own. Nevertheless, there is still a significant amount of blood flowing inside the aneurysm, reflecting the large pore size of this stent. The position of the inflow jet has changed as well due to the eCLIPs. In the geometry without the eCLIPs, the inflow jet is located closely right of the left vessel wall inside the aneurysm. In the treated case, it is located slightly more to the right and no longer follows the left side of the wall inside the aneurysm - instead, we observe the mean jet to be located in the middle of the domain with its shape fragmented by the wires of the stent.

The time-averaged velocity field showed considerable changes caused by inserting the eCLIPs. These changes are also reflected in the time-specific velocity fields shown in figure 4.7. At  $t_1 = 0.11$  s and  $t_3 = 0.42$  s, these changes appear more evident than in figure 4.6. Fragmentation and relocation of the inflow jet are very clearly seen here, and to smaller extent at  $t_2 = 0.32$  s and  $t_4 = 0.76$  s. In the time-averaged velocity fields, the flow field inside the piece of vessel located after the aneurysm sac changed slightly with insertion of the eCLIPs. In the time-specific fields, the flow fields are more distinct in this part of the geometry. For example at  $t_3$ , both the shape and magnitude of the stream have changed locally. We conclude that major changes in the flow field caused by the eCLIPs can be shown in the time-averaged flow field, but could be misleading; big differences could be cancelled out over time. We therefore recommend to consider the time-specific velocity fields as well, to get a better grasp on the actual changes made by the flow diverter.

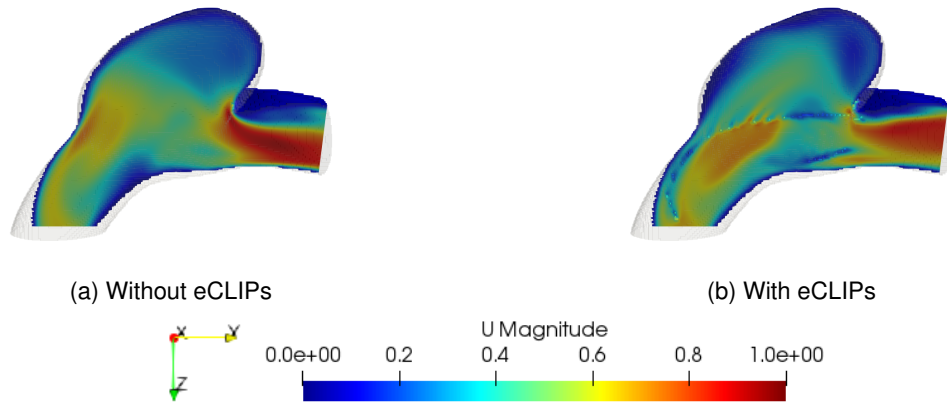


Figure 4.6: Average velocity over one cardiac cycle in the Portugal geometry showing a cross section at  $x = 0.023$  m, inside and around the aneurysm sac.

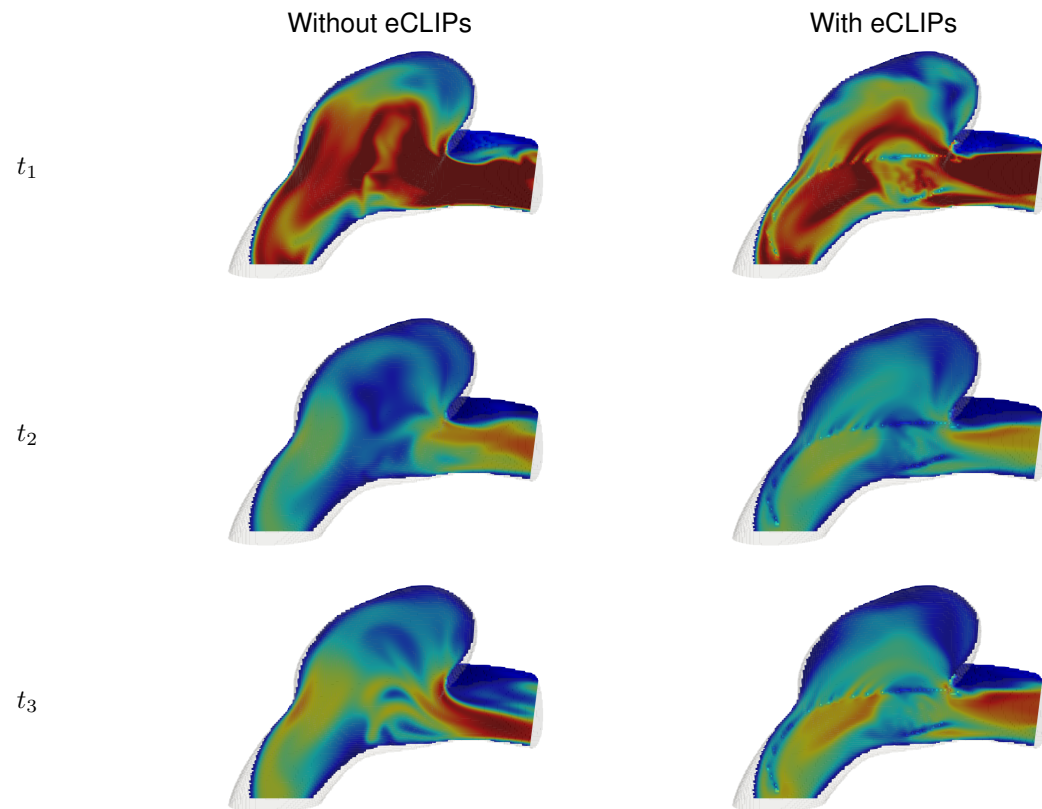


Figure 4.7: Time specific velocity fields of the Portugal geometry showing a cross section at  $x = 0.023$  m, around the aneurysm sac. The magnitude is shown at  $t_1 = 0.11$  s,  $t_2 = 0.32$  s,  $t_3 = 0.42$  s,  $t_4 = 0.76$  s, representing respectively peak systole, end systole, peak diastole and end of diastole. (continues on next page)

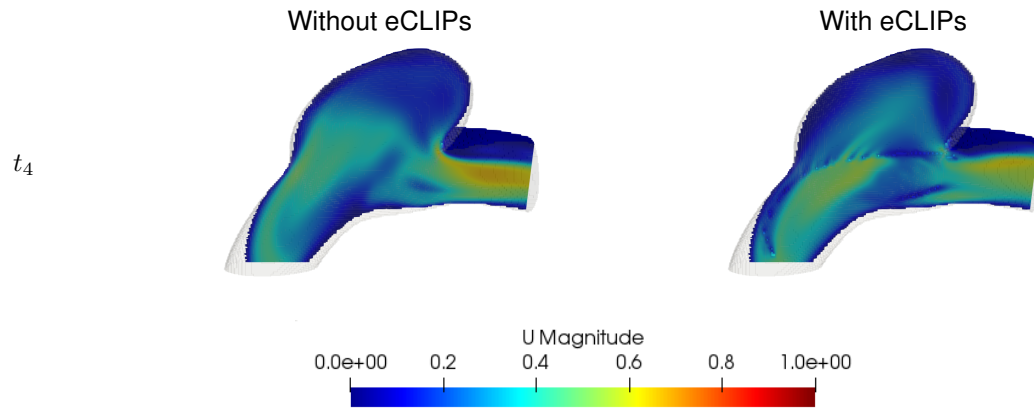


Figure 4.7: Time specific velocity fields of the Portugal geometry showing a cross section at  $x = 0.023$  m, around the aneurysm sac. The magnitude is shown at  $t_1 = 0.11$  s,  $t_2 = 0.32$  s,  $t_3 = 0.42$  s,  $t_4 = 0.76$  s, representing respectively peak systole, end systole, peak diastole and end of diastole.

The time-averaged wall shear stress was computed for the Portugal geometry. The results are shown in figure 4.8. The differences are subtle. With insertion of an eCLIPs, the wall shear stress decreases around the aneurysm. This is most obvious on the vessel wall directly below the aneurysm neck. This section shows an average wall shear stress of around 20 Pa without the eCLIPs, which was reduced to zero almost entirely with insertion of an eCLIPs. Also in the crease of the aneurysm neck the wall shear stress has decreased considerably.

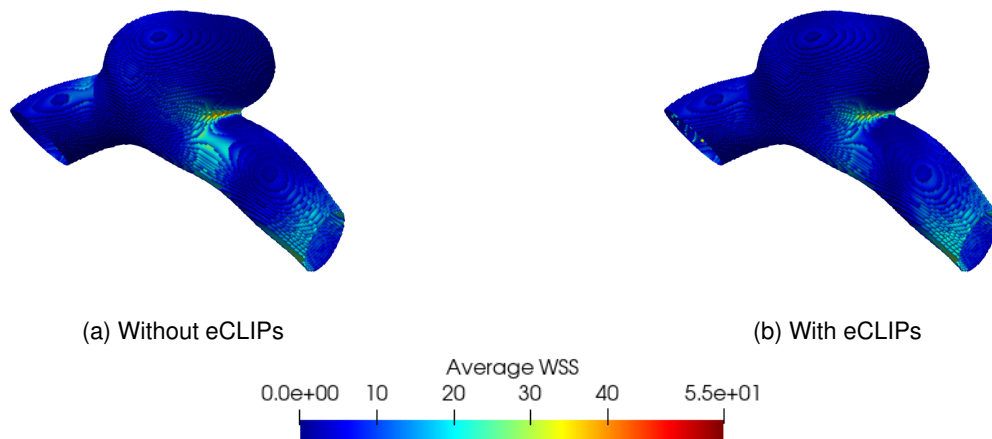


Figure 4.8: Average wall shear stress over one cardiac cycle in the Portugal geometry.

To see how well the effect of the eCLIPs stent is reflected in the averaged wall shear stress, the wall shear stress at peak systole is shown in figure 4.9, for the configurations with and without the eCLIPs. Overall, the wall shear stress takes on much higher values than the averaged shear stress, but this is only for an instant. The effects of the eCLIPs are similar to what was shown in the averaged plots; especially in the piece of vessel to the right of the aneurysm, insertion of the



eCLIPs has lowered the wall shear stress considerably. Smaller changes in the wall shear stress are now also observed on the aneurysm sac, this could not be perceived from the averaged field. This is similar to what was concluded for the averaged and instantaneous velocity fields: bigger changes in the field are captured by the averaged fields, but for more subtle effects, the instantaneous fields should be consulted.

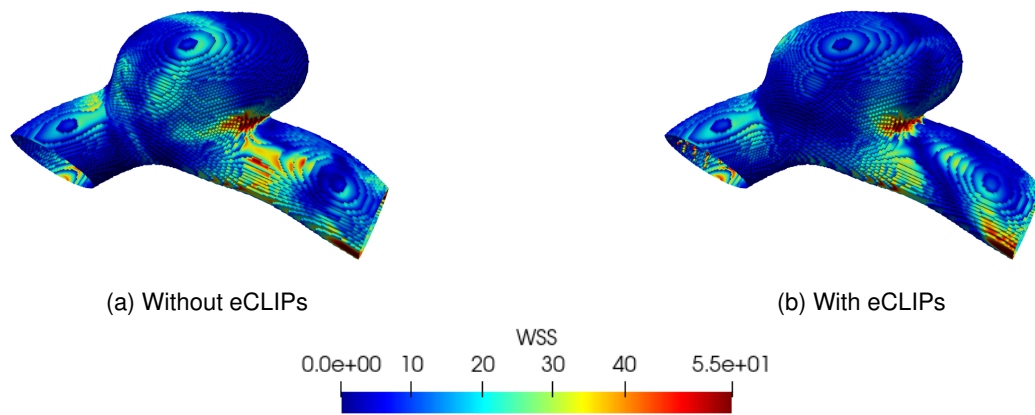


Figure 4.9: Wall shear stress at peak systole ( $t_1 = 0.11$  s).

The differences in the OSI with or without the eCLIPs are very evident, as becomes clear when comparing figures 4.10a and 4.10b where the OSI is displayed. Both on the aneurysm wall and around the aneurysm neck, the OSI has decreased significantly with insertion of an eCLIPs. This results in a lowered risk of rupture of the aneurysm according to key literature on OSI [32]. Therefore, the eCLIPs accomplishes to some extent the objectives of flow diverting treatment.

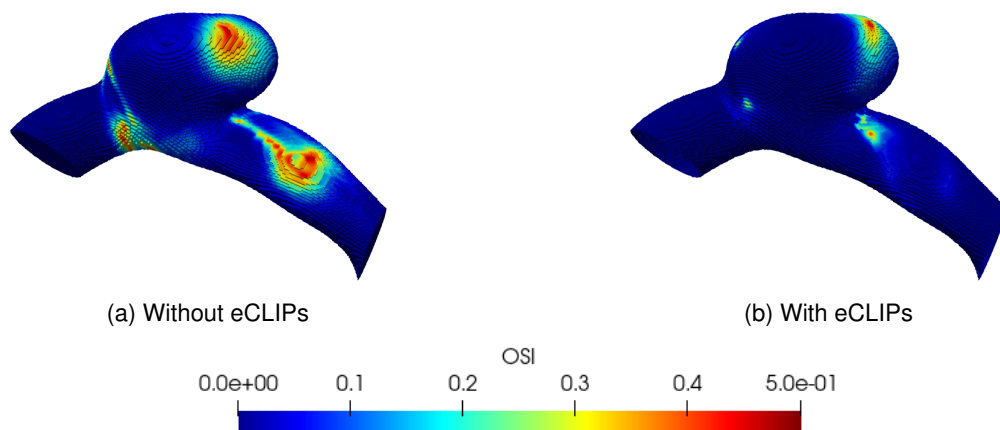


Figure 4.10: OSI over a single cardiac cycle in a treated and an untreated Portugal geometry.

From the velocity, WSS and OSI the modification of the flow due to the placement of an eCLIPs is well illustrated. We next consider how the placement of an eCLIPs affects the dispersion of a cloud of particles as presented by our virtual bolus visualisation. In particular, this may further quantify parameters that have a direct relevance on the likelihood of a stable thrombus forming,

such as aneurysm filling factor and residence time. The remainder of this section will address how the modifications in the blood flow due to the placement of an eCLIPs are reflected by the assessment method covered in section 4.2. First, a particle simulation has been done for both geometries. For these simulations, the improved algorithm as defined in section 3.4 was used. The bolus has been simulated for the duration of a single cardiac cycle. A snapshot of the bolus at the moment of entering the aneurysm is shown in figure 4.11. This also illustrates the subtle difference that was seen in the velocity fields in figure 4.6. Particles still enter the aneurysm in the treated geometry, but they tend to follow the course of the blood vessel better. The particles in the untreated geometry penetrate further into the aneurysm than in the treated case and appear to be organized more in an impinging jet.

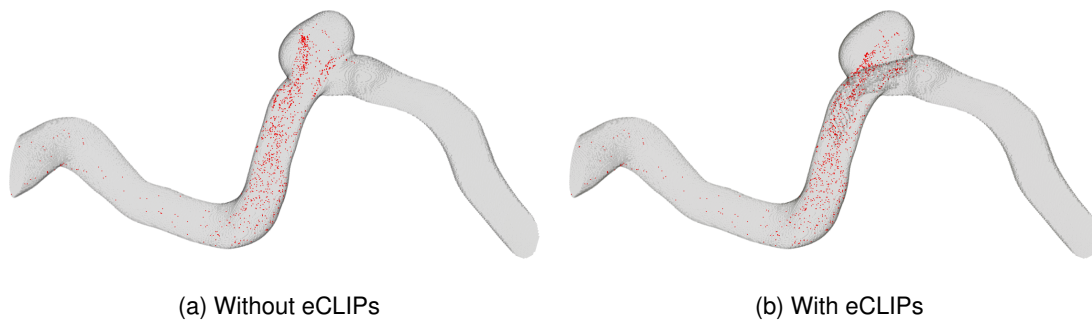


Figure 4.11: Bolus at the moment of entering the aneurysm ( $t = 0.08$  s).

To analyze the locations of the particles at different times in the bolus simulation, the Portugal geometry has been divided into different sections. The partition of the geometry can be seen in figure 4.12. The sections divide the geometry in a way that makes sense topologically, as already described in chapter 4.2. The separate sections are (with color labelling): **inlet**, **vessel attached to aneurysm**, **aneurysm** and the **blood vessel after aneurysm**. Note that the aneurysm has been distinguished from the remaining part of the vessel by a plane. Since the particles move around inside the aneurysm, the exact boundary of this section is not essential for examining whether or not particles have visited this part of the geometry. Hence, a plane that distinguishes the aneurysm from the remaining vessel is adequate for this study.

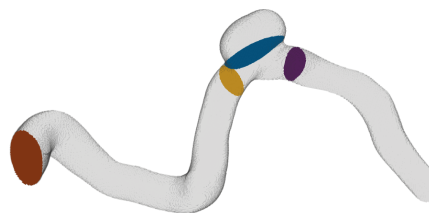


Figure 4.12: Partition of the Portugal geometry for analysis of the particle simulations enabling to track particles and classify these accordingly in different groups.

The so-called cumulative plots of the particles over the simulations can be seen in figure 4.13. These plots show which fractions of particles have visited a particular part of the geometry during the bolus simulation. Note that these fractions do not sum up to one: this measure keeps track of whether a particle has visited some part of the domain at any time during the simulation. For both geometries, all particles have visited the inlet section instantly. This makes sense: all particles

are released as a uniformly distributed slice at the inlet. The first particles reach the part of the vessel attached to the aneurysm at the same time. When looking at the number of particles that have visited the aneurysm, the difference between the geometry with and without the eCLIPs is obvious. In the untreated geometry, 83% of the particles visit the aneurysm at some instant during the bolus simulation. In the treated case, this reduces to 58.2%, showing the flow-diversion induced by the eCLIPs.

In figure 4.13 the cumulative fraction of particles that went through the outlet and through the connecting part of the vessel does not entirely add up to one. This is because some of the particles move very slowly through the geometry and some of them have not completed their journey through the entire domain within one cardiac cycle. This has also been mentioned in section 4.2, and is caused by particles beginning very closely to a wall implying a very low velocity. By decreasing the area of the initial particle cloud and allowing no particles in the immediate vicinity of the walls, this could be avoided. Since this only affects 2% of particles, it was decided to keep the originally constructed particle cloud.

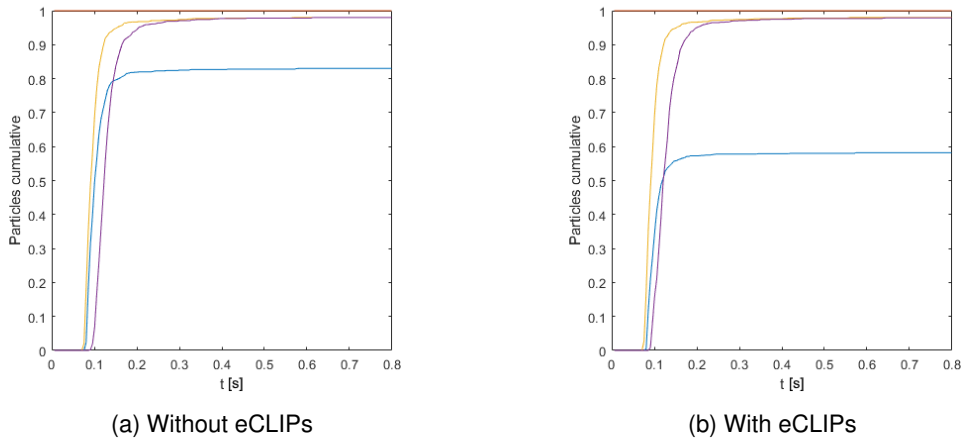


Figure 4.13: Cumulative plots throughout the bolus simulation of the Portugal geometry as defined in figure 4.12. In these plots the fraction of particles that has passed at any instant one of the distinguishing four planes is tracked: **inlet**, **vessel toward aneurysm**, **aneurysm sac** and **vessel after aneurysm sac**.

The live locations of the particles throughout the particle simulation can be seen in figure 4.14. In contrast to the cumulative plots, these plots sum up to one at each instant, since they represent the fraction of particles present in each part at any moment in time. The difference between the untreated and the treated geometry is less obvious than in the cumulative plots. The plots for the aneurysm section are slightly different. The maxima of this section for the treated case and the untreated case are respectively 30.9% and 36.5%. This illustrates the partial flow diversion induced by the eCLIPs, avoiding a fraction of the particles from entering the aneurysm sac at all.

The difference between the cumulative fractions of the treated and untreated geometry is further illustrated by the residence times of the particles inside the aneurysm. The particles that actually visited the aneurysm at some point in time, stayed there for 0.021 seconds on average in the geometry without the eCLIPs, and for 0.028 seconds in the geometry with the eCLIPs. This means that, on average, the particles stay inside the aneurysm for 33% longer which may contribute to the process of thrombus formation that may follow placement of the eCLIPs. It appears that the particles inside the aneurysm are to a somewhat larger extent the same particles in the treated case, while in the untreated case, more of them are replaced with other particles. The significance of this difference in residence times between the treated and untreated configuration are

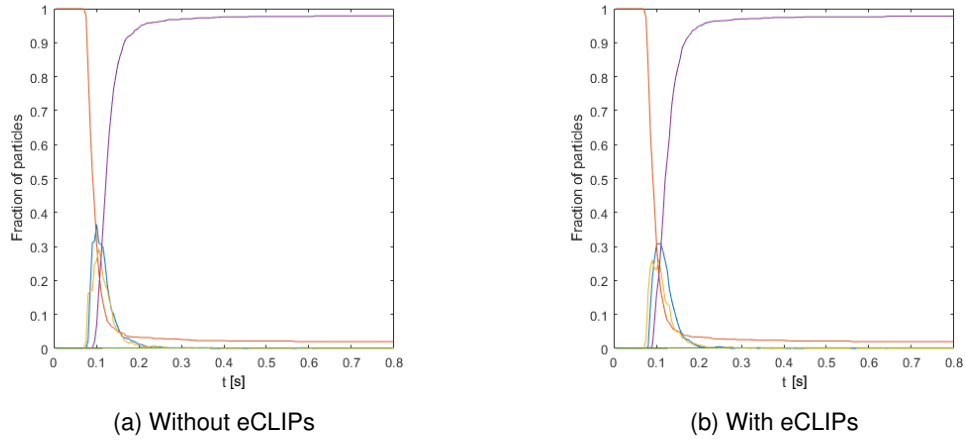


Figure 4.14: Live locations of particles throughout the particle simulation: **inlet**, **vessel toward aneurysm**, **aneurysm sac** and **vessel after aneurysm sac**.

further explored in section 4.4.

To illustrate the need for a particle tracking algorithm that handles wall collisions, as described in section 3.4, the bolus simulations have been done using the basic algorithm as well. In these simulations, particles that ran into a fluid/solid interface disappeared from the simulation. Especially in the case with eCLIPs, this resulted in the loss of almost 50% of the particles, as can be seen in figures 4.15 and 4.16. The fraction of particles that got lost during the simulation are given by the **green** line in figure 4.16. In figure 4.15 this is the fraction of particles that does not reach the outlet of the geometry. In the simulation without eCLIPs, around 10% of particles gets lost during the simulation. Because of this big discrepancy, the significance of changing from the basic algorithm to the improved algorithm are clearly underpinned.

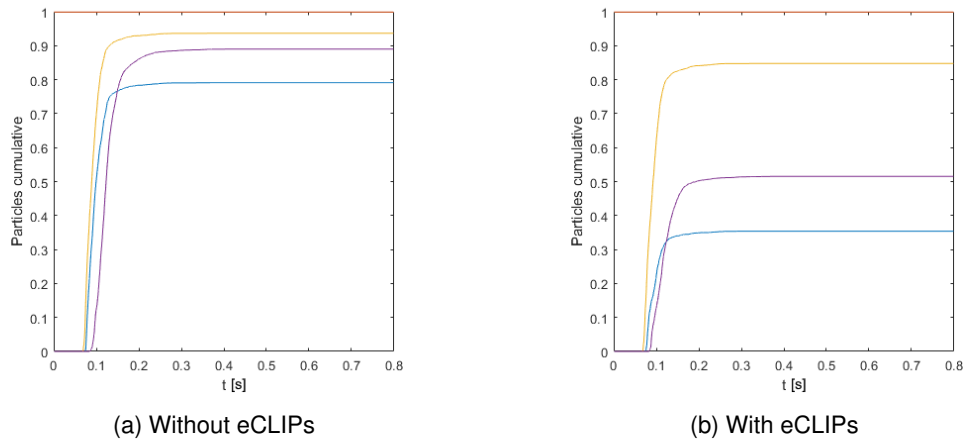


Figure 4.15: Cumulative plots of particles obtained using the basic algorithm in which a significant fraction of the particles gets lost numerically due to collisions with any solid wall.

In this section, the effect of inserting an eCLIPs stent inside the Portugal aneurysm geometry has been investigated. Besides it was examined to what extent this effect was evident from the assessment method that was proposed in section 4.2. Concluding from the previously presented results, particularly the instantaneous plots illustrate the flow-diverting properties of the stent even

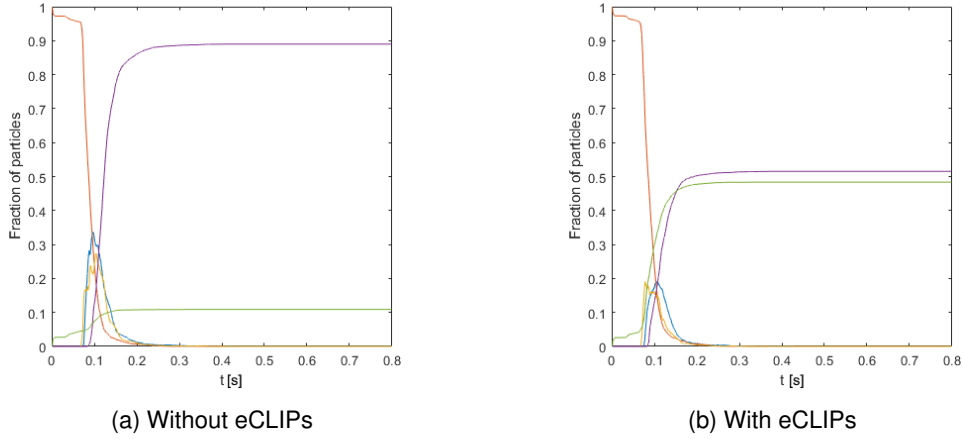


Figure 4.16: Live locations of particles using the basic algorithm in which a significant number of particles gets lost numerically by collisions with any solid wall - this fraction is represented by the green curve.

qualitatively, while the effect in the cumulative plots and the residence times of particles inside the aneurysm sac provide further quantitative support. The goals of a flow diverter are to decrease the blood flow that goes into the aneurysm, and also stagnate the flow inside the aneurysm, such that a thrombus is more likely to develop there. We see that these goals are met by the eCLIPs: a significantly smaller fraction of particles visits the aneurysm, and also they stay there for a longer time. This contribution can be clearly identified from our proposed assessment method based on the virtual bolus.

## 4.4 Sensitivity

In this section, the robustness of the proposed assessment method will be quantified. Even though our approach has been automated, it still heavily depends on human-made decisions. The impact of these decisions on the outcome of the grading method will be researched. First of them is the resolution of the grid that is used for the fluid simulations. In section 3.3 it was already shown that the velocity fields vary slightly for different grid resolutions. In this section, we will investigate how strongly these small variations are reflected in our proposed assessment method. Furthermore, the number of particles in the virtual bolus is of importance. Simulating an insufficient amount of particles causes variation in the particle cloud, and therefore possibly in the outcome of the assessment. Finally, the partition of the geometry into different sections is a crucial part of the proposed assessment. This is done manually, leaving room for inter-observer variability. Small influences of the factors described above would give us confidence in the usefulness of our post-processing protocol, as well as in the assessment of the virtual treatment using this method.

The impact of grid resolution on the outcomes of the post-processing have been examined using a grid with half the resolution of the grid used in section 4.3. Due to stability constraints, the simulations on both grids have been done with an average inlet velocity of 16 cm/s, instead of 20 cm/s as done in the previous section. The used grids are shown in figure 4.17. The particle simulations were done for the duration of one cardiac cycle, similar to the case in section 4.3.

The cumulative plots for the particle simulations on the two different grids are shown in figure 4.18. There is a small difference in the percentage of particles visiting the aneurysm. In fact,

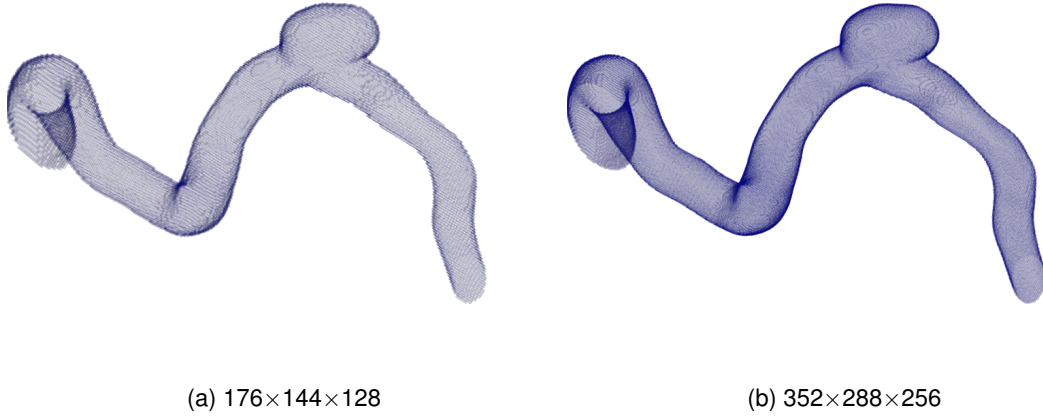


Figure 4.17: Two different resolutions of the Portugal geometry, with respectively 25 and 50 grid cells per diameter of the inflow vessel.

84.8% and 81% of the particles visited the aneurysm in the coarse and fine grid respectively. Moreover, fewer particles reach the aneurysm neck in the coarse grid, a result that was already established in section 4.2. The effect of the grid resolution on the residence time of particles inside the aneurysm is also small. For the  $176 \times 144 \times 128$  resolution, the residence time is slightly larger: 0.0285 s against 0.0275 s for the finer resolution. It appears that grid resolution has a rather small influence on both measures based on the particle simulation. This confirms that using 25-50 grid cells across the diameter of the inflow vessel appears adequate. Additionally, some further coarsening of the grid might be considered for accurately determining cumulative visitation rates and residence times under cheaper computational costs.

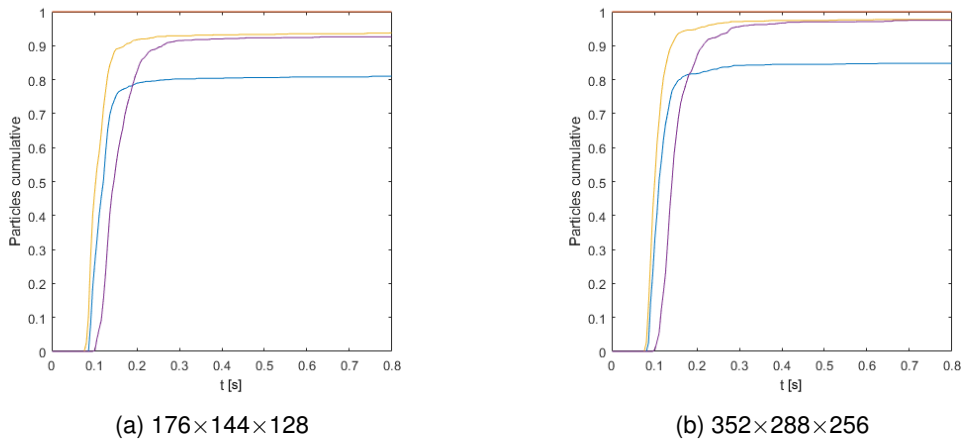


Figure 4.18: Cumulative plots of particles through geometries of two resolutions of Portugal geometry.

The effect of the eCLIPs in section 4.3 was also observed in the differences between average wall shear stress and the OSI of both geometries. These two fields were determined for both grid resolutions, see figures 4.19 and 4.20. OSI and WSS have similar qualitative properties in the two grids. The higher resolution pictures reveal more detailed patterns in both OSI and WSS,

that could not be captured at the lower resolution. It can be concluded that both WSS and OSI are fairly robust against refinement of the grid, but more detailed patterns are only revealed at the higher resolution. To get a first impression of areas exposed to higher and lower stresses, the coarsest resolution, with 25 grid cells per inlet diameter gives a very useful representation.

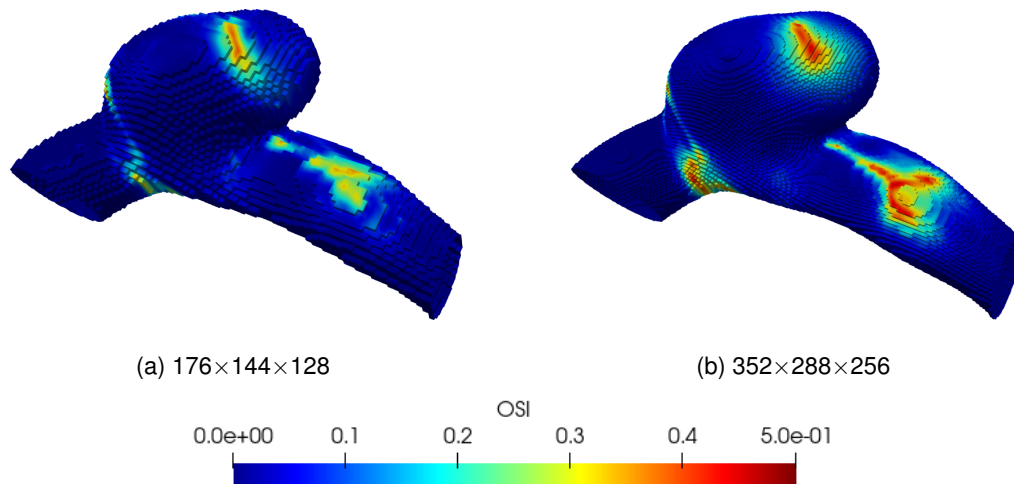


Figure 4.19: OSI for the different resolutions of the Portugal geometry.

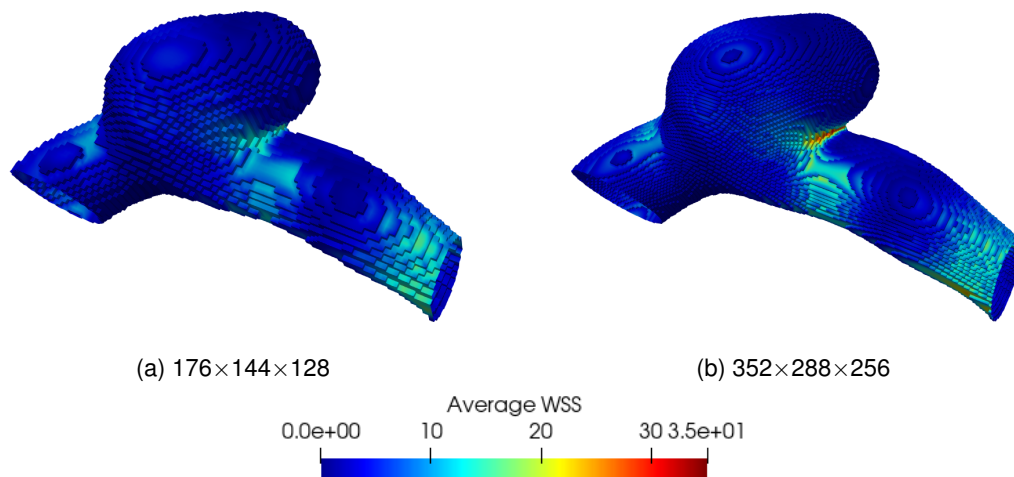


Figure 4.20: WSS averaged over the duration of one cardiac cycle for the different resolutions of the Portugal geometry.

The particles generated initially at the inflow are uniformly distributed over the inlet plane of the geometry. This will quickly adapt to the flow and give spatial variations in the particle distribution. To obtain reliable particle clouds, also the number of particles is of interest and will influence the reliability of the predictions. We look into this next.



Analysis of the variation of the bolus-based measurements has been done by a numerical experiment. Particle simulations with varying number of particles were done on the untreated geometry from section 4.3 with equal resolution, for the duration of one cardiac cycle. For each number of particles, the simulation was repeated five times, each simulation starting from a random initial distribution of particles over the entry boundary, to examine the variation of the considered measures under the same circumstances. The residence time and the cumulative visitation rates of the aneurysm section for each of the bolus simulations are shown in 4.21. It appears that generating more particles at the inlet decreases the variance of both measures within the same simulations. Maximum standard deviations of both measures are seen for  $N = 250$ , which are 2.75% for the cumulative visitation fraction, and 0.001 seconds for the mean residence time. These deviations amount to respectively 3.3% and 5% of the mean observed values for the two measures considered. This uncertainty is decreased even further when simulating more particles. Additionally, this uncertainty can be approximated by the difference between the minimum and maximum values observed for each measure. For simulations with 1000 particles or more, the difference between maximum and minimum values for cumulative visitation rate and residence time are 4.4% and 0.0019 s respectively. That means that, for simulation of 1000 particles the cumulative visitation rate equals  $84.8 \pm 2.2$  %, and residence time equals  $0.0211 \pm 0.00095$  s for the untreated Portugal geometry. The values found in the previous section, which are also based on a bolus simulation with 1000 particles, respectively 83% and 0.021 s, lie within this interval. These measures equal 58.2% and 0.028 s respectively for the geometry with eCLIPs. Differences between these measures for the treated and untreated Portugal geometry are greater than the uncertainties determined by the simulations here. We can conclude that these differences are the effect of alteration of flow induced by the eCLIPs, and not by variance of this method.

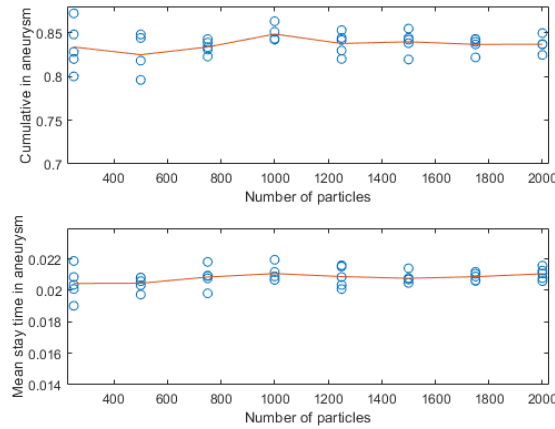


Figure 4.21: Variance in cumulative visitation fraction and residence time in the aneurysm for the  $352 \times 288 \times 256$  resolution of the Portugal geometry, for a varying number of particles. Blue circles represent individual simulation outcomes, orange line represents the mean from these simulations.

Division of the underlying geometry is done manually. Each vessel geometry is divided into topologically characteristic sections. The crucial part is defining the aneurysm section in the structure. The effect of defining the aneurysm slightly different is assessed next. Two alternative partitions were considered, where separating planes have the same normal as the reference partition used in section 4.3, but are 0.5 mm above or below respectively. The reference and alternative partitions are shown in figure 4.22. For all three partitions the cumulative and instantaneous visitation rates of the aneurysm sac were determined, based on the same particle simulation. These are shown in figure 4.23. From these figures, it is seen that separating the aneurysm slightly too



close to the parent vessel has a much larger impact than placing it a little further away from the remaining structure. This is also reflected by the residence times, which equal 0.0185 s, 0.0207 s and 0.0325 s for the partitions with slightly higher, original and slightly lower separating planes respectively. From this, we can conclude that defining the plane separating the aneurysm from the remaining parts of the geometry slightly too high has less severe consequences than defining it too low.

Additionally, variation of the location of this separating plane provides more details on the dispersion of the bolus inside and near the aneurysm sac. From the cumulative visitation rates of the three different planes considered in this section, shown in figure 4.23, we see that 83% of particles visited the aneurysm section with the original partition, whereas 80.8% of particles did when the plane was located 0.5 mm higher. This means that the majority of particles visiting the aneurysm sac went deeper than 0.5 mm. Considering these planes at multiple heights, provides more details on the flow dynamics inside the aneurysm sac. Moreover, 98% of particles visited the aneurysm section when the plane was located 0.5 mm below the original partition, implying that almost all particles pass the aneurysm opening at a very close distance. Determining the cumulative and instantaneous visitation rates for a variation of partitions can be done under negligible computational costs. Variation of the plane separating the aneurysm section from the remaining vessel geometry gives more details on the dispersion of the bolus. Additional research on, for example, the effect of treatment on this dispersion of the particle cloud is highly recommended.



Figure 4.22: Portugal geometry with three different partitions: blue: original partition, orange: 0.5 mm under original partition and yellow: 0.5 mm above original partition.

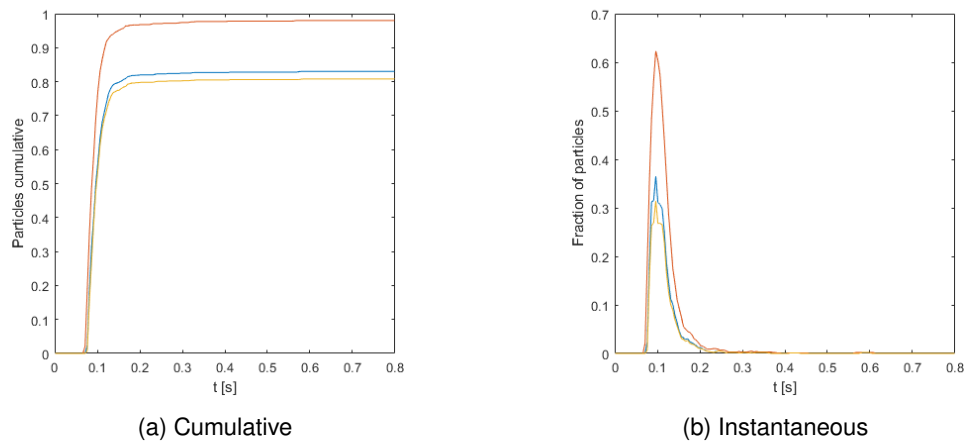


Figure 4.23: Visitation of the aneurysm section, for the three different partitions as defined in figure 4.22 as a function of time. **Blue: original partition**, **orange: slightly below original partition** and **yellow: slightly above original separating plane**.

## 4.5 Conceptual product

In the previous sections, a number of currently available assessment parameters were described, as well as the newly proposed assessment involving the virtual bolus. Our ultimate aim is to provide the neurosurgeon with information, supporting the decision for optimal treatment. A trade-off should be made between completeness and conciseness of the information provided. On the one hand, we have seen that using a single score may lead to oversimplification of the complex process, while on the other hand, we want to inform the neurosurgeon of important features of the situation in a matter of minutes. That is why we present our ‘product’ in the form of a layered report, containing a combination of quantitative and qualitative information. The first representation of the information would be compact and clear; mostly globally averaged fields, sketching the main features of the flow inside the vessel structure. More detailed information, such as time-specific fields or other (coarser) resolutions are available as a second layer upon request.

The design of the report will contain scores and fields that should precisely characterize the effects of a possible treatment, as well as not vary too much between simulations when varying the spatial resolution. These conditions were investigated in the case study of the Portugal geometry covered in section 4.3 and the sensitivity analysis in section 4.4. Therefore, to start an iterative process toward such concise clinical reporting, we propose a standardized report which contains the following sections, where nested items are available upon request, when the neurosurgeon wishes for additional information.

### Report aneurysm

Patient A

#### 1. Geometry

Smoothed segmentation of the aneurysm section, obtained from MRI/CT data, as well as immersed boundary representation of this geometry. Also direction of blood flow is indicated.

## **2. Velocity fields**

Cross section(s) showing the magnitude of the velocity field, averaged over one cardiac cycle. The(se) cross section(s) should capture the main features of the flow inside the aneurysm sac, as well as the connecting blood vessels. This is given at a single, sufficient resolution: in principle 30 grid cells per diameter of the inflow vessel.

Optional extra information:

- Instantaneous velocity fields at the given cross-section(s).
- Coarser resolutions.

## **3. Wall shear stress**

Wall shear stress averaged over one cardiac cycle, at the proposed resolution.

Optional extra information:

- Instantaneous wall shear stress.
- Coarser resolutions.

## **4. Oscillatory shear index**

OSI at the proposed resolution.

Optional extra information:

- Coarser resolutions.

## **5. Virtual bolus**

Animation showing the dispersion of the particle cloud through the aneurysm geometry, for one or two cardiac cycles.

Cumulative divisions of particles over aneurysm geometry as a function of time.

Residence time of particles in aneurysm section.

Optional extra information:

- Instantaneous division of particles over vessel geometry as a function of time.
- Coarser resolutions.

This layered representation of information provides a complete overview of the situation, and can be quickly reviewed by the neurosurgeon. More information about, for example, the maximal wall shear stress can be added in the same format and accessed easily from the synoptic representation using an interface. In this study, we have focused on the contents of the report, rather than interface development. Designing such an interface is therefore left for further research and development, where interaction with the intended users is crucial.

In this chapter, we have shown that a report containing the features described above, can capture features of the flow of a side-wall aneurysm, as well as show qualitative and quantitative changes made by a possible treatment. As was mentioned in the introduction, bifurcation aneurysms form a persistent challenge for neurosurgeons, due to the complex flow patterns formed inside. With the report as presented in this section, we hope to inform the neurosurgeon on the situation of the patient, assisting in finding a successful treatment of the aneurysm. In the next chapter, we will present and give some interpretation of such a report for the PCOM geometry i.e., the geometry given in figure 2.4c.

## Chapter 5

# Assessment of PCOM aneurysm

In the previous chapters, we covered all the necessary steps included in the ideal pathway of treating a patient, as introduced in figure 1.1. Chapter 2 covered the necessary steps from MRI data to modelling the flow inside the vessel geometry. Since the model covered in chapter 2 can only be solved numerically, chapter 3 introduced the use of a discrete masking function and the OpenFOAM software, to calculate the flow inside the geometry on a discrete grid. This method was executed for steady and pulsatile flow on two aneurysm geometries and showed promising results in terms of convergence and accuracy. In chapter 4, the objective was to extract useful information from these data-dense velocity fields. It became clear that a few 'grading indices' to represent the many aspects of the flow can lead to oversimplification of the situation of the patient. Therefore, it was proposed to not assess the patient's situation with a single grading scale, but provide the neurosurgeon with a detailed yet concise report, that gives insight in the current situation of the aneurysm, and can also show changes of the flow inside the aneurysm, induced by a potential treatment. This has already been shown for the Portugal geometry in section 4.3. This geometry is an example of a side-wall aneurysm, which are, in general, successfully treated by neurosurgeons. The remaining piece in this study is the persistent challenge of treating bifurcation aneurysms. The report that has been introduced in chapter 4, will be presented on the flow simulations of the PCOM aneurysm considered in this study. This results in a multi-layer report, as was described in section 4.5, that can be delivered to the neurosurgeon. The structure and contents of this report will be shown in section 5.1. It includes both an overview of the main features of the dynamics, but can be consulted for more detailed information as well. Interpretation of this report, in terms of fluid dynamics is covered in section 5.2. This chapter will end with a sensitivity analysis of the metrics considered in the report, to the effects of slight variations in the anatomical configuration of the PCOM geometry.

### 5.1 Numerical decision support for PCOM

Intracranial aneurysms located on the posterior communicating artery branching from the internal carotid artery are commonly seen [19]. In this section, we present the contents and structure of the report as proposed in section 4.5, for the PCOM aneurysm considered in this study.

## 1. Geometry

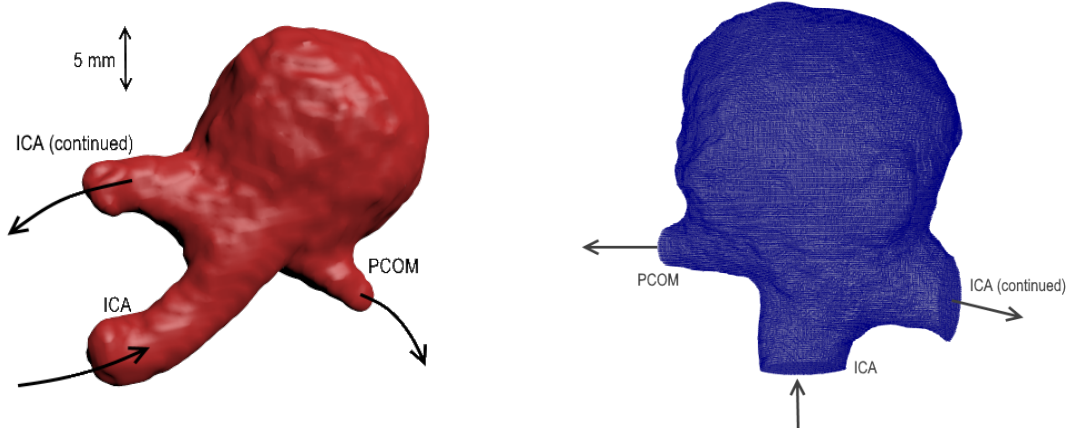


Figure 5.1: Continuous, segmented representation of the PCOM aneurysm (shown left), together with the immersed boundary representation at  $200 \times 180 \times 240$  resolution (48 grid cells per diameter of the inflow vessel). Arrows indicate the direction of blood flow through this geometry.

## 2. Velocity fields

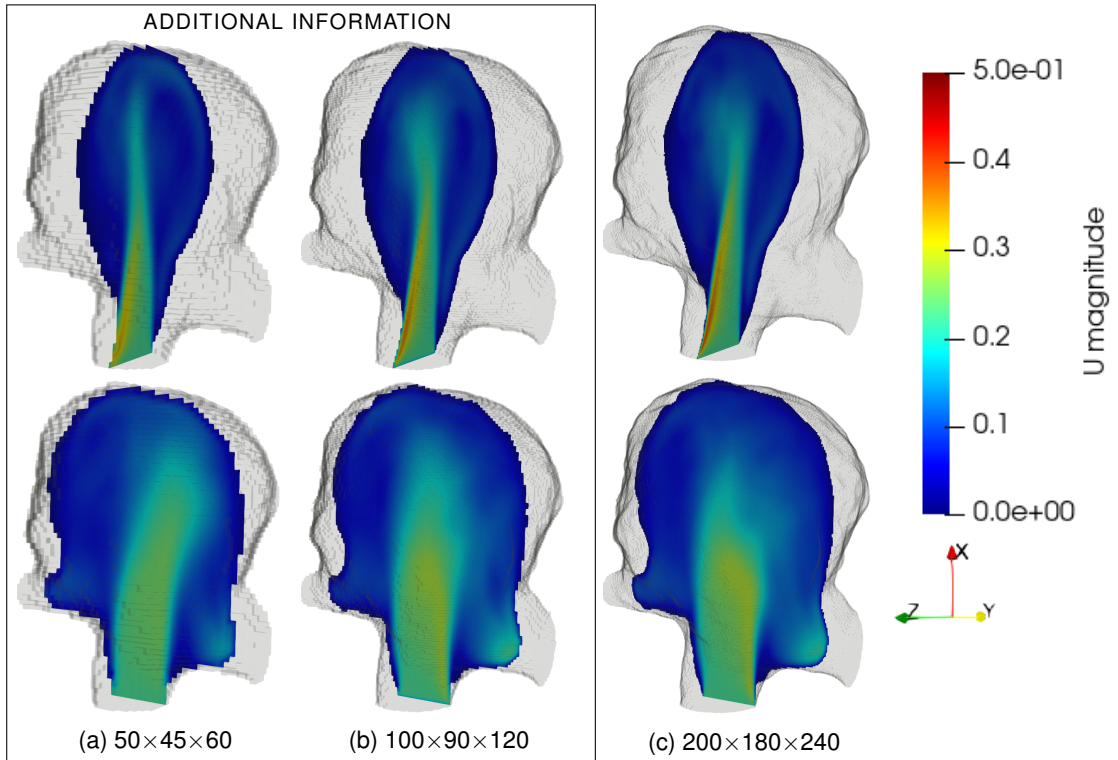


Figure 5.2: Velocity inside the PCOM aneurysm, averaged over one cardiac cycle at the three available resolutions. The average velocity field is shown at two cross sections:  $z = 0.0084$  m (top row) and  $y = 0.008$  m (bottom row).

In this report, we show two different cross-sections of the PCOM aneurysm, whereas only one cross-section was provided for the Portugal geometry. We want to give information about both the dispersion of the inflow jet in the aneurysm sac, as well as the proportion of blood flowing through the two bifurcating vessels. These features were sufficiently captured in a single cross-section for the Portugal case, but require two different cross sections in the PCOM case.

The additional part of information available upon request are the time-dependent fields. This concerns instantaneous velocity fields for both cross-sections. For the cross section  $z = 0.0084$  m, as shown in figure 5.2, instantaneous velocity fields at a number of characteristic moments in the cardiac cycle were shown in figure 3.13. For the  $200 \times 180 \times 240$  resolution, we show velocity fields at the same instants for the cross section  $y = 0.008$  m.

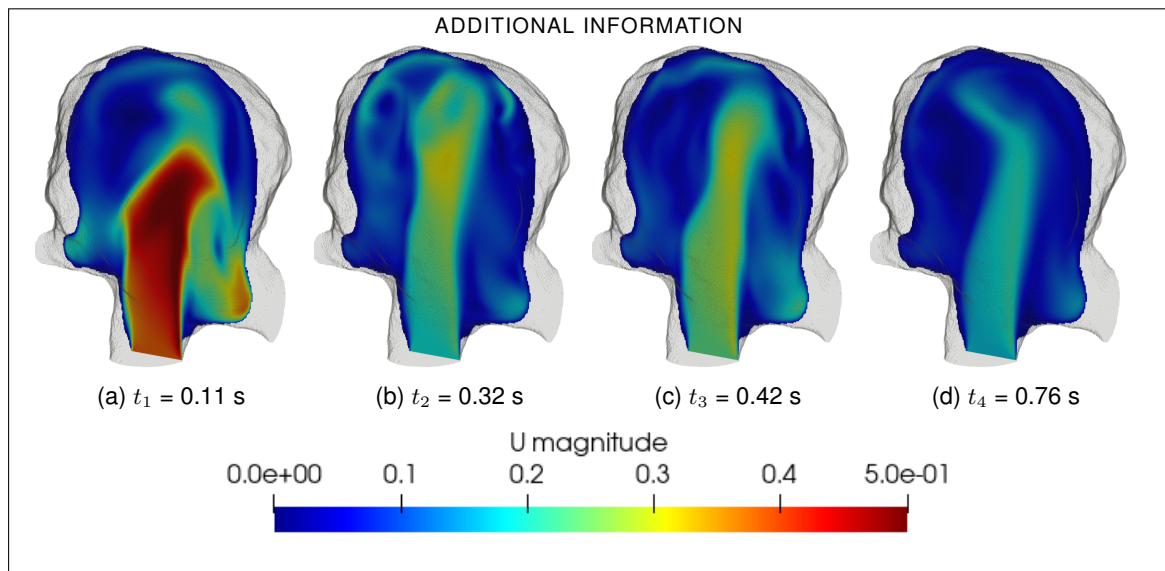


Figure 5.3: Cross sections at  $y = 0.008$  m of instantaneous velocity fields, with  $200 \times 180 \times 240$  resolution, shown at peak and end of systole and peak and end of diastole respectively.

### 3. Wall shear stress

The wall shear stress for the PCOM aneurysm is shown at both linear and logarithmic scale. The shear stress on the aneurysm dome is rather small, therefore the patterns in the shear stress are better distinguished on a log scale than on a linear scale.

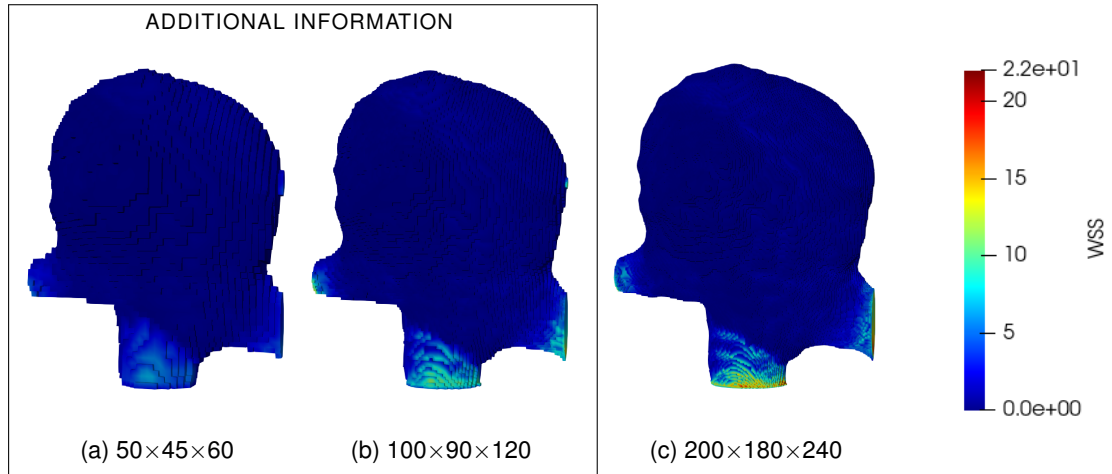


Figure 5.4: Wall shear stress averaged over one cardiac cycle on linear scale, for the three available resolutions of the PCOM geometry.

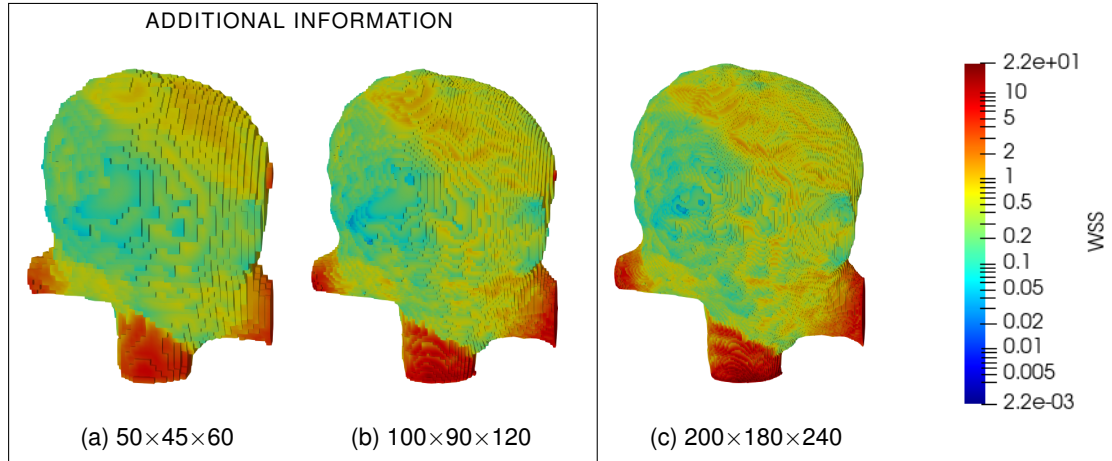


Figure 5.5: Wall shear stress averaged over one cardiac cycle on logarithmic scale, for the three available resolutions of the PCOM geometry.

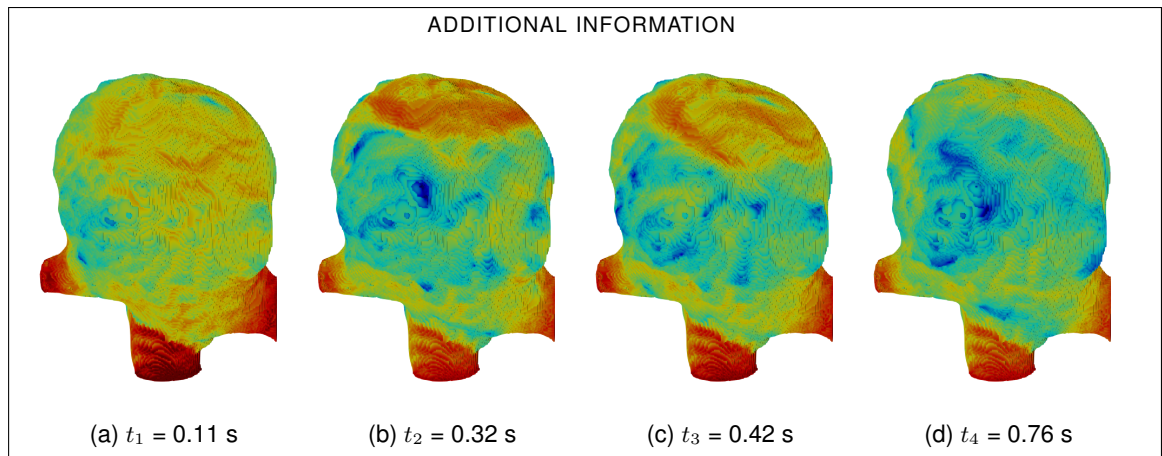


Figure 5.6: Wall shear stress at a number of characteristic moments in the cardiac cycle, for the  $200 \times 180 \times 240$  resolution of the PCOM aneurysm. Logarithmic scale is the same as in figure 5.5.



#### 4. Oscillatory shear index

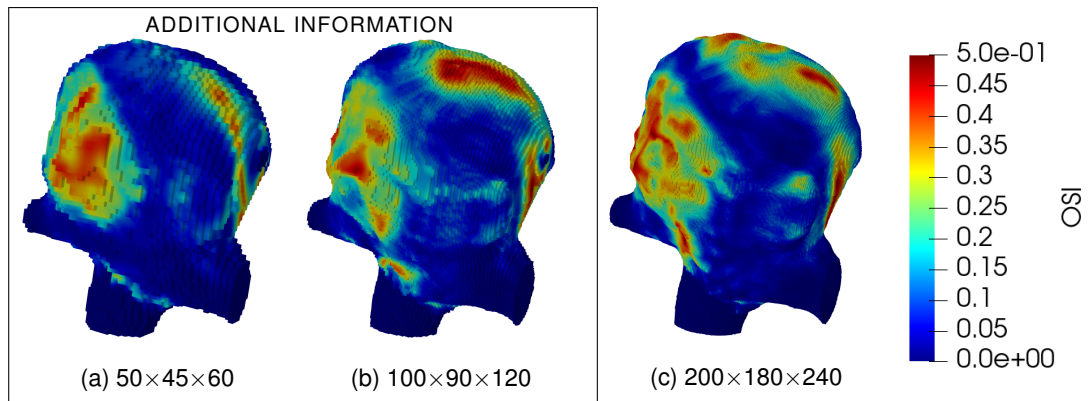


Figure 5.7: OSI for varying resolutions

#### 5. Virtual bolus

Instead of an animation, a few snapshots of the bolus through the PCOM geometry are shown in figure 5.8. The locations of particles in the PCOM geometry have been shown at  $t = \{0.05s, 0.1s, 0.15s, 0.2s\}$ , since these instants best represent the dispersion of the bolus through the aneurysm over time. The bolus simulation for the Portugal simulation was analyzed for the duration of a single cardiac cycle. We analyze the bolus in the PCOM geometry for two cardiac cycles (up until  $t = 1.6$  s), since the majority of particles is still inside the geometry after a single cardiac cycle.

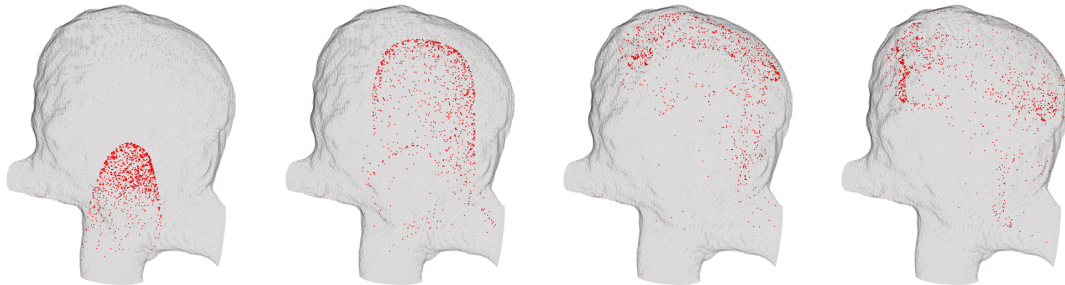
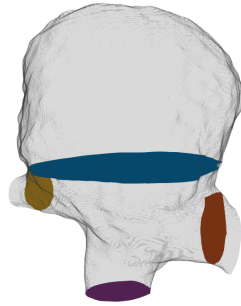


Figure 5.8: Virtual bolus at  $t = \{0.05s, 0.1s, 0.15s, 0.2s\}$  respectively.

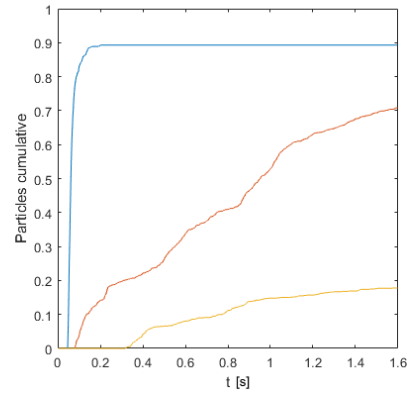
Measure	50×45×60	100×90×120	200×180×240
Cumulative fraction visiting aneurysm	87.8%	85.9%	89.3%
Residence time in aneurysm	0.78 s	0.61s	0.68 s

Table 5.1: Measures of the bolus through the PCOM aneurysm at different grid resolutions. Scores resulting from simulations with 50×45×60 and 100×90×120 resolutions are shown in gray, since they are part of the additional information.



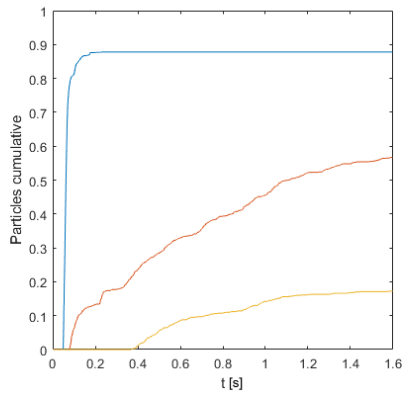


(a) Division of PCOM geometry

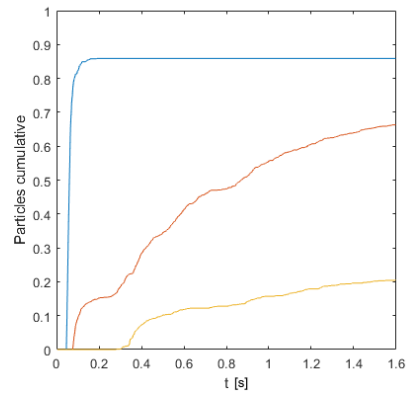


(b)  $200 \times 180 \times 240$

#### ADDITIONAL INFORMATION



(c)  $50 \times 45 \times 60$



(d)  $100 \times 90 \times 120$

Figure 5.9: Cumulative plots of particles passing the three different planes in the PCOM aneurysm, simulated for two heartbeats. The blue line corresponds to the particles that have travelled through the aneurysm, the orange and yellow lines to the particles that departed the geometry via the ICA and PCOM artery respectively.

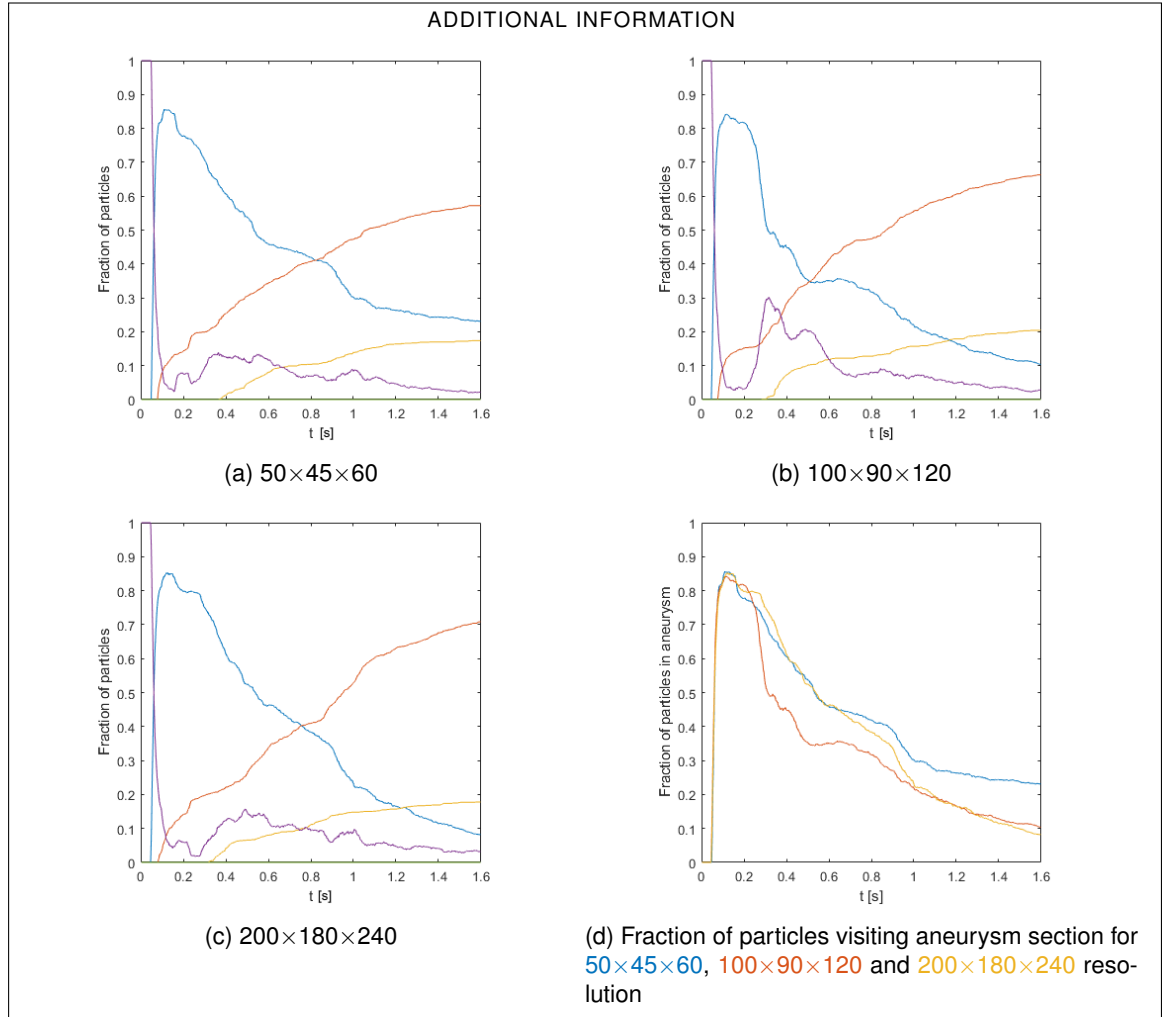


Figure 5.10: Instantaneous division of particles as a function of time for varying grid resolutions of PCOM geometry. Blue: inside the aneurysm, orange: big bifurcating vessel, yellow: small bifurcating vessel and purple: vessel connecting the aneurysm and outlets.

## 5.2 Interpretation PCOM report

In the previous section, we presented the report delivered for numerical decision support as proposed in section 4.5, for the PCOM aneurysm considered in this study. This provides the neurosurgeon with a detailed, yet concise representation of the flow characteristics, resulting from computational fluid dynamics. This report contains a number of figures and scores, whose relevance was already argued in the previous chapters. In this section we give a more detailed interpretation of the findings in the report.

### Velocity fields

Cross sections of the time averaged velocity field are shown in figure 5.2. These give a first impression of both size and coherence of the impinging jet, correlated to aneurysm rupture [15], as well as the flow velocity inside the aneurysm sac. From the cross-sections at  $z = 0.0084$  m, it can be seen that the inflow jet is stronger at the front of the inflow vessel. Moreover, the jet bends slightly to the right bifurcating vessel (ICA), implying that the mass flow through this vessel is larger than in the PCOM. The averaged velocity fields for different grid resolutions appear almost identical, both in shape and magnitude. In the cross-sections of all three resolutions, the inflow jet appears rather diffuse, implying a large area of impingement.

To see how well the flow dynamics are captured in the averaged cross-sections, we compared this average to the instantaneous velocity fields. For the cross-sections at  $y = 0.008$  m, these are shown in figure 3.13. For these cross-sections, the inflow jet in the instantaneous fields is more curved than in the averaged fields, where its shape is rather straight. Also the inflow jet is longer in some of the instantaneous fields, nearly reaching the top of the aneurysm dome at some instants. For the cross-section at  $z = 0.0084$  m, the averaged velocity field with resolution  $200 \times 180 \times 240$  was compared to the instantaneous fields shown in figure 5.3. Similar to the other cross-section, the length of the inflow jet is smaller for the averaged case compared to the most intense instants. The magnitude of the impinging jet at peak systole ( $t_1$ ) is approximately twice as large as in the averaged field. The slight curvature to the right is seen in the instantaneous fields as well. Most features observed in the averaged velocity fields are also evident in the instantaneous fields. The reverse is not true: some particular shapes and magnitudes of the inflow jet are only seen in instantaneous fields.

### Wall shear stress

In figures 5.4 and 5.5, the time-averaged wall shear stress for different resolutions of the PCOM geometry is shown. Although the wall shear stress on the aneurysm dome is relatively small, it becomes clear from the logarithmic plot that the wall shear stress takes on higher values at the top right of the aneurysm, and is relatively low in the left half of the dome. Areas under low wall shear stress are also associated with a higher rupture risk [24], or can indicate aneurysm growth [10], implying that in particular the left half of the aneurysm dome might form a problematic area. The shear stress on the connecting blood vessels is rather high compared to the aneurysm sac. The velocity inside these vessels is relatively high, compared to the velocity inside the aneurysm.

The time-averaged quantity forms a first indication of the distribution of stress over the geometry. To get a more detailed impression of locations undergoing large stresses, the wall shear stress at different moments in time was considered - for the  $200 \times 180 \times 240$  resolution these are shown in figure 5.6. At peak systole, the wall shear stress attains its maximum value. The shear stress is relatively high on almost the entire aneurysm dome. During the remaining part of the cardiac cycle, the wall shear stress in the middle section of the aneurysm decreases. The meaning of these time-dependent developments of the wall shear stress in terms of rupture risk or optimal treatment remains unclear. However, it could be possible to estimate the low shear area based on these figures; this measure is correlated to rupture risk [24, 57]. If slightly longer pieces of connecting vessel would have been left attached, the local shear stress in the parent artery could

be determined more accurately for this particular patient, giving the opportunity to better interpret the low shear area of this aneurysm.

### **Oscillatory shear index**

Besides the magnitude of the wall shear stress, also the directions of the flow relative to the wall are a good characterisation of the flow dynamics, in particular of the effect the flow may have on the cells directly lining the vessel wall. More specifically, the relevant measure is the change of direction of the wall shear stress in the course of time, which is indicated by the oscillatory shear index (OSI). The advantage of the OSI over the WSS is that this measure is not time-dependent, since it is defined as an integral over time in section 4.1. Also, for the OSI it is known that large values indicate an increased risk of rupture [60]. In figure 5.7, the OSI for the PCOM geometry at different resolutions is shown. All three figures appear qualitatively similar. Large values in the OSI appear around the same areas, for example on the left half of the aneurysm sac. If we combine this with the fact that the wall shear stress on that part is relatively low (figure 5.5) we see that, this part could be subject to an increased rupture risk. Such type of statements from CFD can be made reliably numerically. To make such statements also relevant clinically, more research into multiple patient cases is crucial.

### **Virtual bolus**

The final part of the report consists of an analysis of the particle simulations through the aneurysm geometry. For the PCOM aneurysm, these simulations have been done for the three grid resolutions considered. In figure 5.8, the bolus at a few moments in time is shown inside the geometry with resolution  $200 \times 180 \times 240$ . At  $t = 0.05$  s, the shape of the bolus is similar to the parabolic profile typically seen in Poiseuille flow. In the other three figures it appears that some particles exit the geometry via the vessel on the right, but most of them continue inside the aneurysm sac. Most of the particles collide with the top of the aneurysm dome. This means that the degree of filling of this aneurysm is rather high. During the remainder of the bolus simulation, not shown in figure 5.8, the particles move along the vortex situated inside the aneurysm sac. After two cardiac cycles, some particles remain here, implying considerable stasis inside the aneurysm.

Similar to the Portugal case in section 4.3, the PCOM aneurysm has been partitioned into a number of sections. Each outlet is a distinct section, as well as the aneurysm. The sections have been separated from each other by a plane, as shown in figure 5.9a. In the other three graphs in figure 5.9, the cumulative fractions of particles visiting these sections as a function of time is depicted for the three resolutions. The most important line in these plots is the blue one, representing the cumulative fraction of particles that have visited the aneurysm. This quantity shows only slight variation for the different resolutions considered: 86.9%, 85.9% and 89.3% for the  $50 \times 45 \times 60$ ,  $100 \times 90 \times 120$  and  $200 \times 180 \times 240$  resolutions respectively. This means most of the particles visit the aneurysm sac at some point during the particle simulation, quantifying the high degree of filling observed in figure 5.8.

From both the instantaneous and the averaged velocity fields, it could be concluded that the mass-flow through the ICA is larger than in the PCOM artery. This is further underpinned by the plots showing the cumulative division of particles in figure 5.9. The difference between the capacities of both vessels is now quantified: on average, 78% of the particles departing the aneurysm geometry do so via the ICA, and 22% depart via the PCOM artery.

The mean residence times for the particle simulations with varying resolutions, as shown in table 5.1, show some differences, on the order of 10% relative to the value obtained at the finest resolution. The mean residence time for the  $100 \times 90 \times 120$  resolution equals 0.61 s, whereas it is equal to 0.78 s for the geometry with  $50 \times 45 \times 60$  resolution. This difference is illustrated by the instantaneous distribution of particles for the different resolutions, as shown in figure 5.10. In the plot corresponding to the  $50 \times 45 \times 60$  resolution, approximately 23% of particles remains in the aneurysm sac at  $t = 1.6$  s. This increases the mean residence time relative to the other

two resolutions, where  $\pm 10\%$  of particles remains in the aneurysm after two cardiac cycles. The difference between the residence times of the  $100 \times 90 \times 120$  and  $200 \times 180 \times 240$  resolutions are also reflected in their instantaneous visitation rates. The fraction of particles in the aneurysm shows a sharp decrease around  $t = 0.3$  s for the  $100 \times 90 \times 120$  resolution, whereas for the refined grid this quantity decreases more gradually, resulting in a greater residence time. It appears that this residence time can be estimated reliably only at an appropriately high spatial resolution.

### 5.3 Sensitivity to alterations in PCOM geometry

Anterior and posterior circulations in the brain are connected via the posterior communicating artery in the circle of Willis. This part of the arterial structure appears in multiple anatomically different configurations [21], with varying ratios between the diameters of the internal carotid artery and posterior communicating artery. On one side of the spectrum, there is the ‘normal’ or ‘adult’ configuration, where the ICA has a significantly larger diameter than the PCOM. The PCOM branch could even be absent. On the other side of the spectrum, there is the ‘full fetal configuration’, where the PCOM diameter is larger than that of the ICA, and the ICA continuation can also be absent [52]. The fetal configuration has an increased chance of aneurysm development [21], as well as unsuccessful treatment of an aneurysm [56]. In [52] it is reported that this configuration is associated with abnormal shear stresses, resulting in damage to the vessel wall, making it more sensitive to aneurysm development. Here, we consider two transitional types, with varying diameter of the PCOM artery, and one full adult type, where the PCOM section is entirely absent. We will identify differences in the flow in these three configurations, in terms of the measures included in the report as proposed in section 4.5. The original PCOM geometry has been modified to match two other configurations: one configuration where the posterior communicating artery has half the diameter, and another one where this vessel is completely absent. The three different configurations considered are shown in figure 5.11, at the  $100 \times 90 \times 120$  resolution, which was the proposed resolution for this assessment in section 4.5.

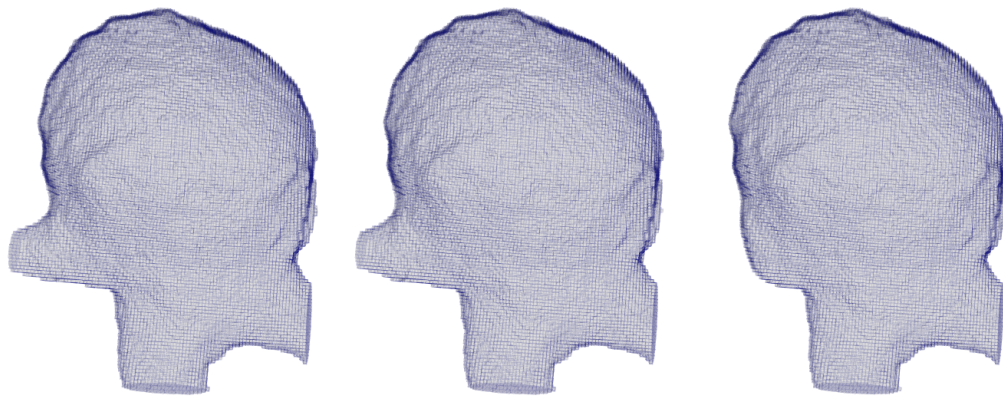


Figure 5.11: Alternative configurations of the PCOM aneurysm: original geometry, geometry where the diameter of PCOM has been halved and a geometry where the PCOM segment is absent. Respectively referred to as type 1, type 2 and type 3, all at  $100 \times 90 \times 120$  resolution (24 grid cells per diameter of the inflow vessel). Type 1 and 2 are transitional types, where type 1 is the ‘more fetal’ type. Type 3 is a full adult configuration.

The main differences in flow dynamics were first identified in terms of the averaged velocity fields,

shown in figure 5.12. The differences between the type 1 and type 2 configurations are very subtle: velocity magnitude appears almost identical. The inflow jet in the type 1 configuration is slightly more diffuse than the one in type 2. The type 3 configuration shows more convincing differences from the other two types. The inflow jet in the cross-section at  $z = 0.0084$  m appears shorter, but from the cross-section at  $y = 0.008$  m we see that this is likely the case because the jet is directed more towards the front of the aneurysm sac. Also the velocity in the ICA is slightly larger in the type 3 configuration than in the type 1 and 2 configurations.

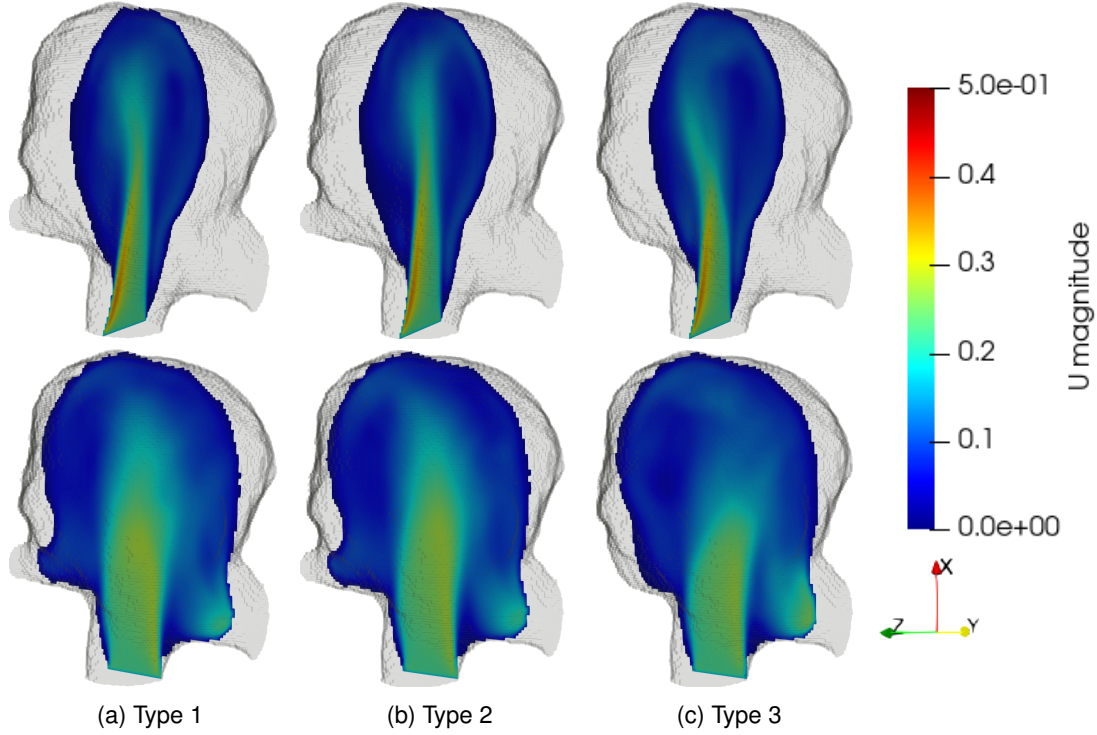


Figure 5.12: Velocity inside the three anatomical configurations of the PCOM aneurysm, averaged over one cardiac cycle. The fields are shown at two cross sections:  $z = 0.0084$  m (top row) and  $y = 0.008$  m (bottom row).

Some qualitative changes between the three different configurations were observed in the cross-sections of the averaged velocity fields. The differences are more pronounced in the instantaneous cross-sections shown in figure 5.13. Differences in the shape of the inflow jet for types 1 and 2 are seen, but their shapes remain roughly similar. For example at end systole ( $t_2$ ), the jets for type 1 and 2 are directed slightly towards the right, but for type 2 it is longer, nearly reaching the aneurysm wall. Velocity magnitudes of all three types remain in the same range at all instants considered. The type 3 configuration shows larger differences from the type 1 and type 2 configurations in the averaged velocity fields. This holds true for the instantaneous fields as well: the patterns in the field clearly differ from the other two configurations. As was seen in the averaged fields, the velocity shows larger magnitude in the ICA of the type 3 configuration than in the types 1 and 2 configurations. The differences in the instantaneous fields are more pronounced than in the averaged fields.

Differences in the velocity fields appear more subtle compared to the topological changes in the aneurysm structure. From literature we know that these different structures have significant effects on pathology and outcome of treatment [21, 56]. This illustrates that minor differences measured by CFD can result in major differences in the remodelling process of the vessel wall,

over a period of months or years. The exact relationship between the velocity fields obtained from these simulations and the remodelling process remains subject to further research.

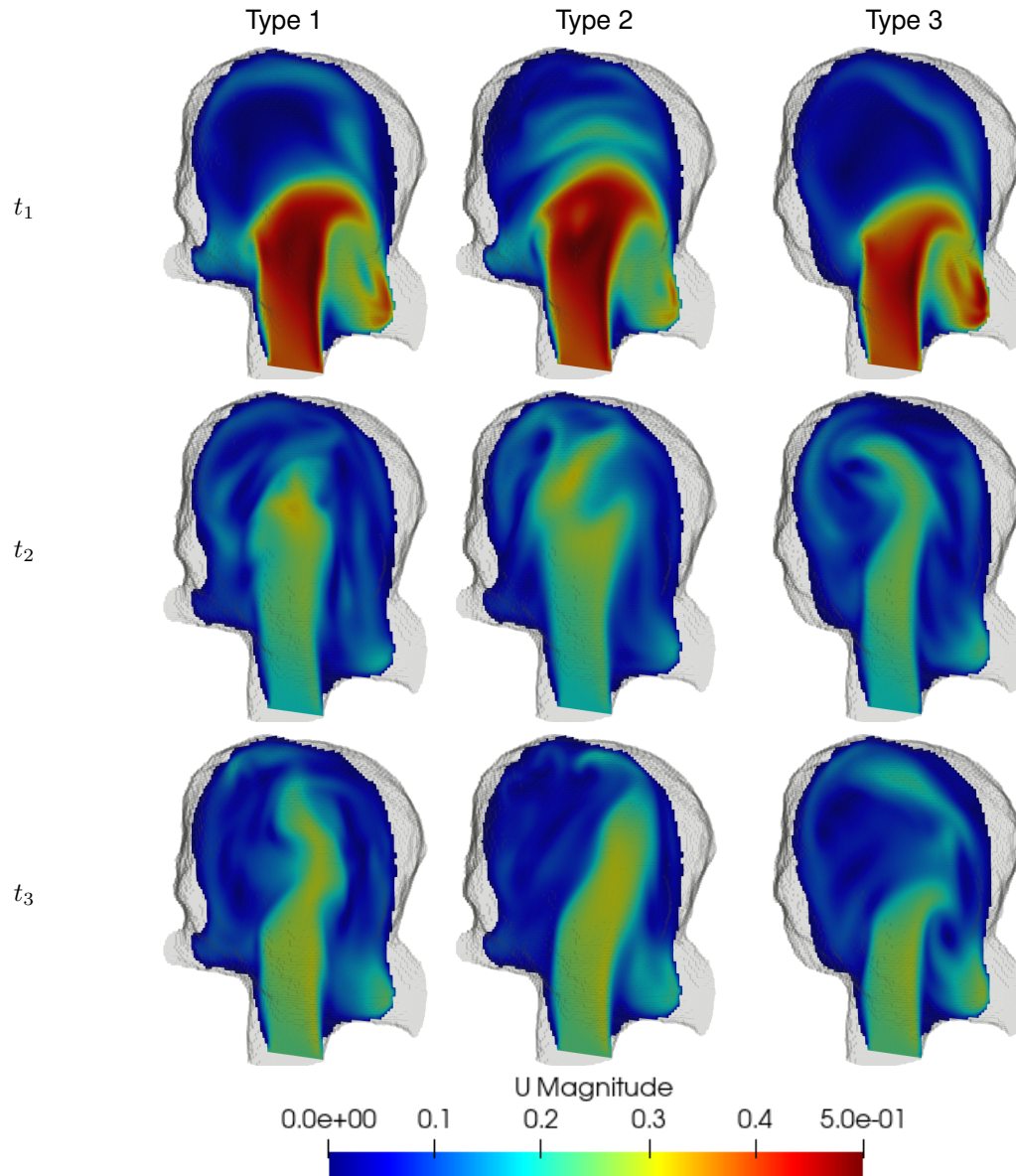


Figure 5.13: Pulsatile flow at peak systole, end systole, peak diastole and end diastole for the three different configurations of the PCOM aneurysm. (continues on next page)



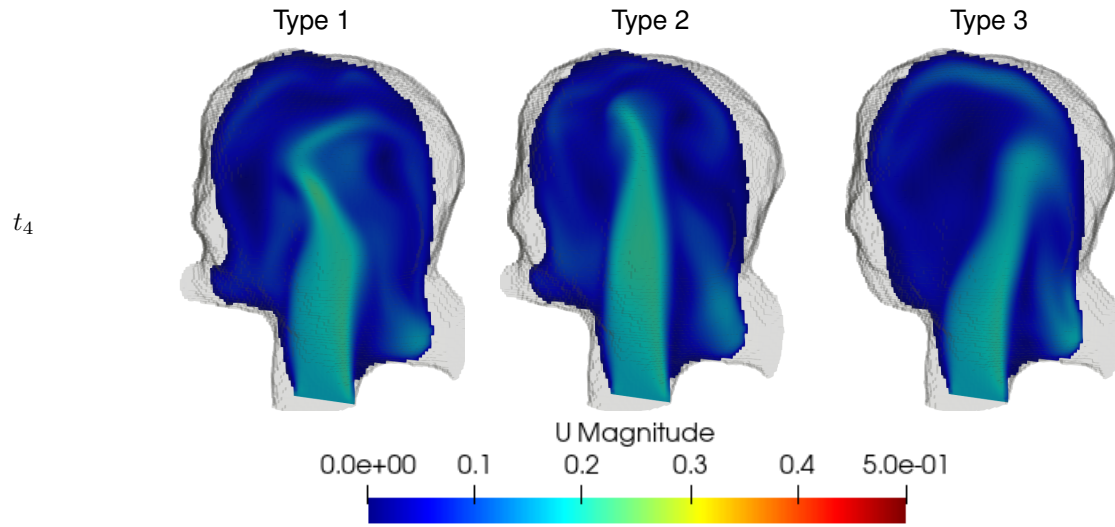


Figure 5.13: Pulsatile flow at peak systole, end systole, peak diastole and end diastole for the three different configurations of the PCOM aneurysm.

In the averaged fields of the wall shear stress, shown on linear and logarithmic scale in figure 5.14, the differences between the configurations are less evident than in the velocity fields. The shear stress around the PCOM artery decreases as its diameter is decreased. Also, the shear stress around the ICA is slightly higher for the type 3 configuration than for the type 1 and type 2 configurations. On the aneurysm dome, differences are barely observable. In the representations on linear scale it is shown that the shear stress is locally relatively low (0-3 Pa). On a logarithmic scale it becomes clear that for all three aneurysms, the WSS on the left part around the middle is relatively low, whereas at the top right part it is somewhat higher. Differences of the same order were observed for the instantaneous shear stresses, at peak and end of systole and diastole.

Compared to the Portugal geometry shown in section 4.3, the WSS on the PCOM aneurysm shows considerably different patterns. In the Portugal aneurysm, there were well-defined hot spots around the aneurysm sac, where wall shear stress attained larger values. In the PCOM configurations, the shear stress is rather uniform over the aneurysm dome, no clear hot spots can be pointed out. Moreover, the maxima the shear stress takes on in the Portugal case, are much larger than the maximum wall shear stress observed for the PCOM case. Both high and low shear stress have been associated with aneurysm rupture [55]. In [35] this is explained by different mechanisms in the vessel wall being stimulated by either high or low shear stress. This might affect the remodelling processes of both aneurysms in the long term. A mathematical model of this remodelling process involving shear stress and multiple processes in the vessel wall have been proposed in [11, 27]. Nevertheless, more research on this topic is still highly necessary.

Although the wall shear stress barely showed any differences among the anatomical configurations, this is not the case for the OSI, which is shown in figure 5.15. The type 1 configuration shows the largest area with a high OSI. The areas with large OSI for type 2 match these of the type 1 configuration, further underpinning their similarity. The OSI for the type 3 configuration attains maxima of similar order to the other two types, but in different locations. How these differences account for consequences for the patient and outcome of the treatment, requires additional research.



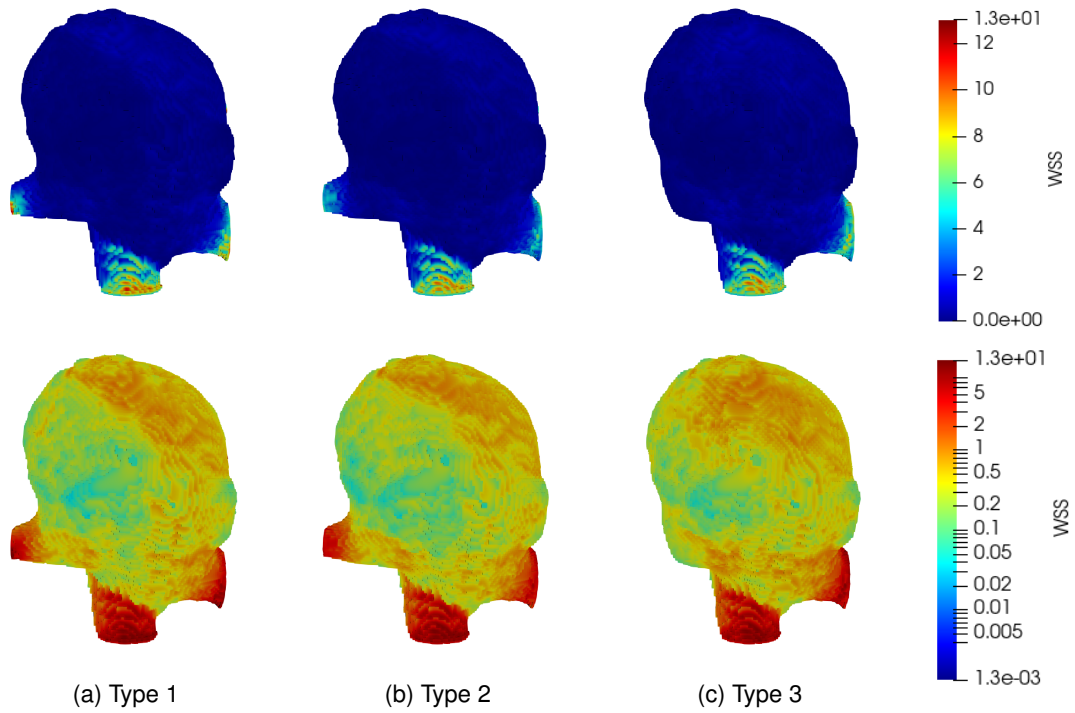


Figure 5.14: Average wall shear stress at linear scale (top row) and logarithmic scale (bottom row) for the anatomical configurations considered.

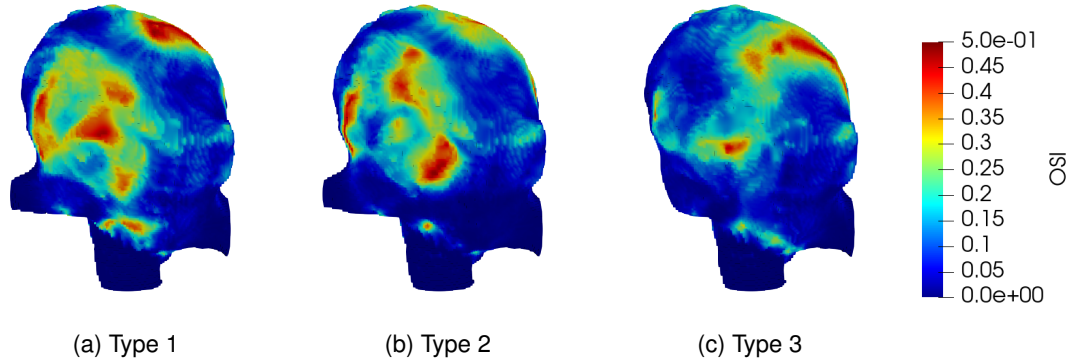


Figure 5.15: OSI for the three different configurations considered.

Finally, particle simulations have been done for all three configurations. The resulting cumulative plots, describing the dispersion of the bolus through the sections of the geometries as a function of time is shown in figure 5.16. Close similarity between the type 1 and type 2 configurations is once again confirmed by these figures: the percentage of particles visiting the aneurysm is almost equal. A difference between the two configurations can be seen in the yellow line, representing the particles exiting the geometry via the PCOM artery. At  $t = 1.6$  s, 20.5% and 14.7% have left via the PCOM vessel in type 1 and type 2 respectively. Particles exit via the PCOM slightly earlier in the type 2 configuration. Significantly fewer particles pass the aneurysm sac in the type 3 anatomy: 76% for type 3, against 86% for type 1 and 2.

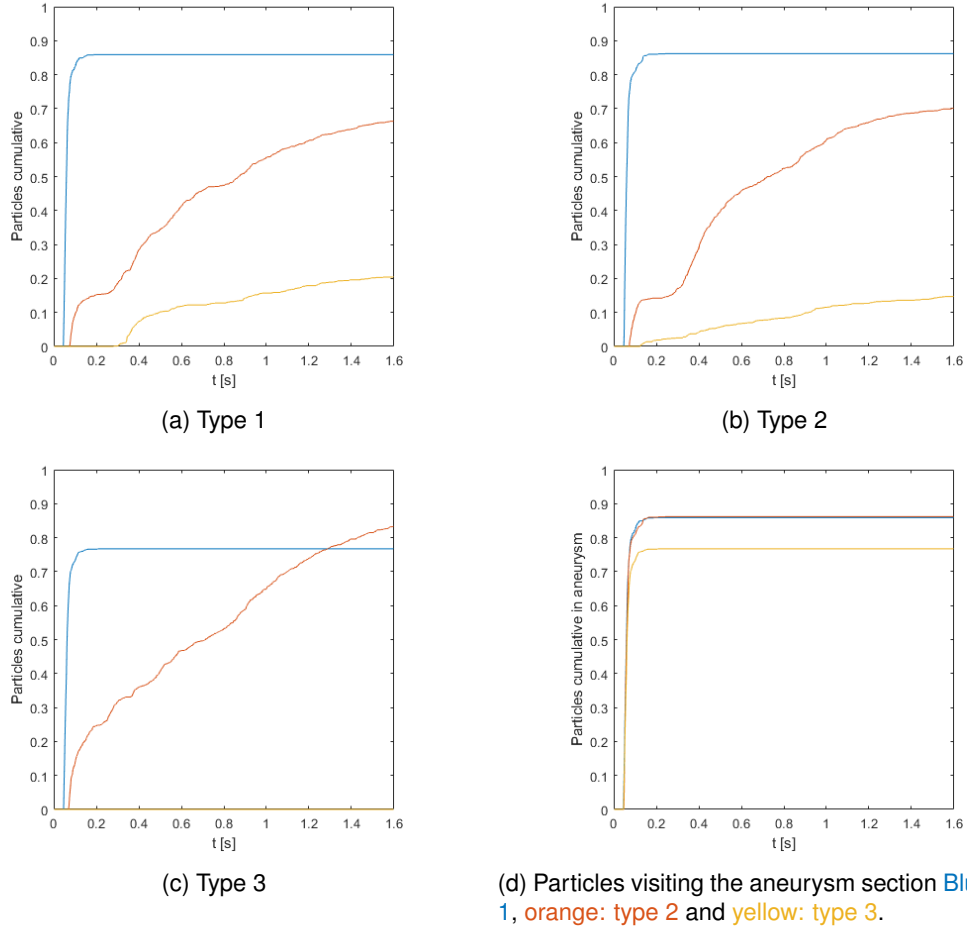


Figure 5.16: Cumulative visitation rates of particles in the virtual bolus algorithm through different configurations of the PCOM aneurysm, partitioned as in figure 5.9a. Blue: Aneurysm section, orange: continuation of ICA, yellow: PCOM artery

Besides the cumulative distribution of particles, the instantaneous dispersion of particles over the separate sections has been investigated for the three configurations. This is shown in figure 5.17. The results for type 1 and 2 are very similar. The maximum of the curve representing the particles passing the aneurysm sac is significantly lower for the type 3 configuration than for the other two, meaning fewer particles visit the aneurysm sac. This was already shown in the cumulative plots in figure 5.16. Furthermore, the mean residence time of particles inside the aneurysm has been determined. This equals 0.61 s, 0.64 s and 0.68 s for the type 1, 2 and 3 configurations respectively. As observed in section 4.4, these differences are larger than the maximal observed variation of 0.003 seconds due to the method itself. We can conclude that the variation of these reference times is a result of the variation in the geometry, rather than variation of the method.

From literature, it is known that patients with a fetal type configuration are more likely to develop intracranial aneurysms [21]. Although no full fetal type PCOM anatomies were considered here, there were considerable differences in some of the measures considered between the full adult and transitional configurations. This gives confidence in the fields and scores included in the report and their link to aneurysm growth and successful treatment options. For example, the full adult configuration showed a smaller area under high OSI, significantly fewer particles visit the aneurysm sac and the residence time was slightly higher compared to the type 1 and type 2 con-

figurations. We believe these measures are related to aneurysm development, and can be used to find an optimal treatment for a particular patient. How these differences relate to the various treatment options available, requires additional research and collaboration with medical experts. An outlook for further development of this method as well as a proposal for collaboration with the medical field is presented in the next chapter alongside the concluding remarks.

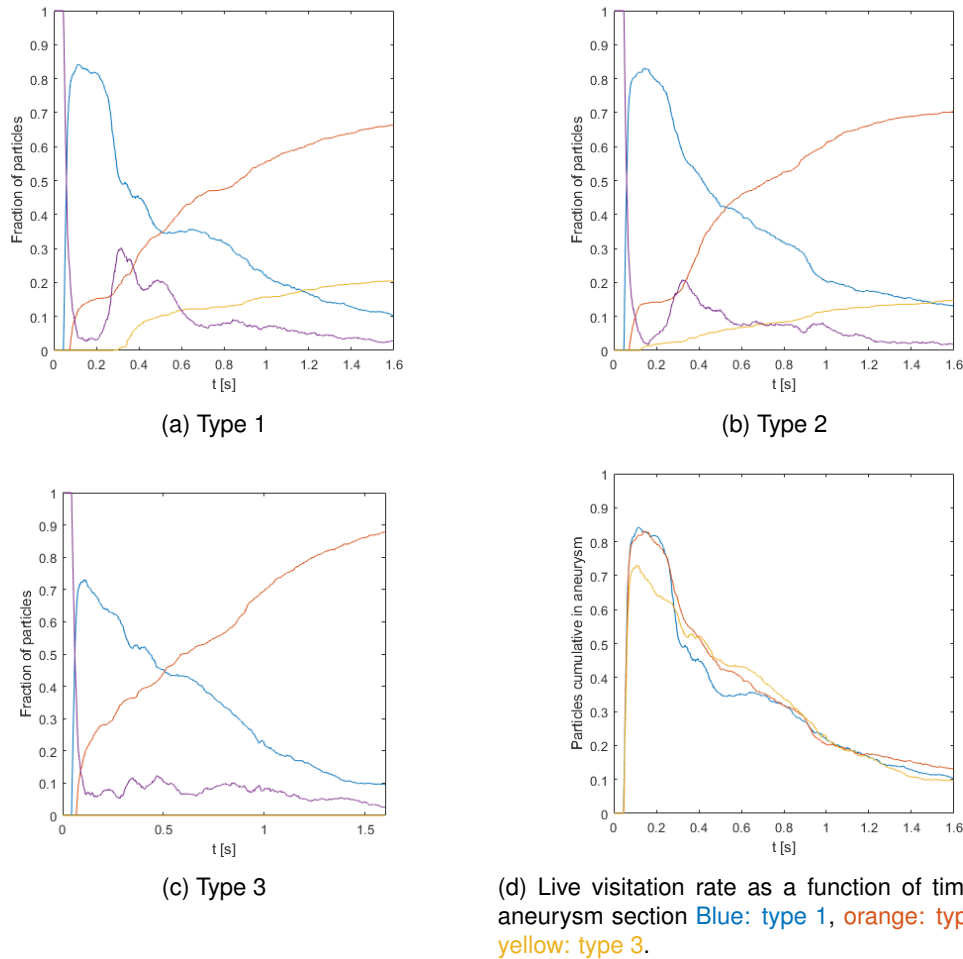


Figure 5.17: Live visitation rates of particles in the virtual bolus algorithm through different configurations of the PCOM aneurysm, partitioned as in figure 5.9a. Blue: Aneurysm section, orange: continuation of ICA, yellow: PCOM artery and purple: junction before outlets and aneurysm.

## Chapter 6

# Conclusion and outlook

In this study, we proposed a novel assessment supporting patient-specific treatment of intracranial aneurysms. This involved the use of computational fluid dynamics on patient-specific geometries. The main feature of this study was using this technique in service of clinical practice, thereby contributing to bridging the gap between mathematical modellers on the one side, and neurosurgeons on the other. This resulted in a proposal for a multi-layer assessment report, containing a variety of scores and figures, that describe the main features of the flow. The ultimate goal is that, based on the information provided by the report, the neurosurgeon can make a well-established decision for a treatment method for a particular patient. To meet this long-term goal, additional research in collaboration with medical experts is highly necessary for which the proposed assessment report can serve as point of departure.

In this chapter we first summarise the main findings from this study, and subsequently elaborate on next steps that can be taken to continue the development of our proposed workflow.

Development of computational decision support introduced many challenges. The first challenge to overcome was achieving realistic simulation of pulsatile blood flow through a patient's vessel geometry. This was accomplished by simulation of incompressible, Newtonian flow in an immersed boundary representation of the original MRI data of the aneurysm in OpenFOAM. The representation of the medical imagery as an immersed boundary is one of the key steps. In this study, this CFD-based procedure was followed for three different aneurysm geometries, two bifurcation aneurysms and one side-wall aneurysm. Flow simulations under pulsatile conditions were started from a fully developed steady state as an initial condition. Moreover, resolution properties of the underlying grid required careful consideration. Representations of the aneurysm geometry at high resolution result in very detailed descriptions of the flow, but come at high computational costs. A proper balance should be struck between resolved spatial detail on the one hand and feasibility of the simulations on the other hand. The information included in the assessment report appears to be fairly robust against grid coarsening at appropriate resolution. We suggest that resolutions in the order of 20-40 grid cells per diameter of the inflow vessel form a good compromise between capturing the flow characteristics in sufficient detail, and keeping the computational costs acceptable; simulations are completed in a matter of hours.

An important element of the numerical decision support is the dispersion of a particle cloud through the flow inside the aneurysm geometry, for which an algorithm has been specifically designed in this study. This algorithm enables a virtual bolus simulation which captures the main spatial and temporal characteristics of the flow. Three different measures were defined based on this virtual bolus. Cumulative and instantaneous visitation rates of main sections of the vessel geometry form the numerical equivalent of the degree of filling used in multiple clinical grading scales. Residence time of bolus particles is also included, forming an analogue to the degree of stasis used by clinicians. In particular, cumulative visitation rate and residence time for the aneurysm section differed significantly after a flow diverter was deployed inside the 'Portugal' side-wall geometry. The effects seen in these measures reflect the purpose of a flow diverter: redirecting the main blood flow from the aneurysm sac into the parent vessel, and slowing down the flow inside the aneurysm to initiate a process of gradual thrombus formation and closure of the aneurysm sac. These effects were seen in the (averaged) velocity fields, as well as in our proposed metrics, by a decrease of the cumulative visitation rate and an increase of the residence

time, giving confidence that our introduced method may be useful for assessment of different treatment methods.

The treatment of the PCOM aneurysm, such as via the Surpass flow diverter shown in figure 3.3, is a particular timely challenge to neurosurgeons. Since the Surpass stent has a more delicate structure than the eCLIPs, virtual placement of a Surpass is more involved. For example leakage, or wires of the stent numerically puncturing the vessel wall are a current source of problems for the algorithm converting the geometry into an immersed boundary representation. Finally, because of the delicate structure of the Surpass flow diverter, the minimal resolution for capturing the flow around the individual wires is significantly higher than 30 grid cells per diameter of the inflow vessel. This will increase the computational time considerably, simulations taking several weeks are not unthinkable. We recommend looking into the possibility of modelling the flow diverter as a separate porous medium. This introduces a specified parameter for the porosity, that modifies the Navier-Stokes equations, similar to the modelling of the porosity of a forming blood clot in [42]. Such porous model can be validated against targeted high-resolution simulations for individual cases in order to arrive at reliable flow predictions at reduced costs.

Additional research considering many more treatment methods and different aneurysm geometries is required, to examine the relationship between the information included in the assessment report and the desired optimal treatment for the specific patient. This research is twofold: CFD needs to be performed on many more treated and untreated aneurysms and the results should be assessed using the workflow from this study. The second aspect of the follow-up research is more empirical and involves statistical analysis of these results, where simulations of treated cases should be compared with the 'golden standard' outcomes of these treatments in practice. This emphasises the need for close collaboration between mathematical modellers and medical experts on this topic.

A first promising feature of the proposed assessment method using CFD simulations is that it appears to generalize well for other aneurysm geometries. Besides the PCOM aneurysm we showed in section 5.1, we turn to some relevant outcomes for the other bifurcation aneurysm considered in this study: the MCA aneurysm. Time-averaged velocity fields of the MCA aneurysm are shown in figure 6.1, at a resolution of 60 grid cells per diameter of the inflow vessel ( $320 \times 304 \times 160$ ). The inflow jet is longer compared to the one seen in the PCOM aneurysm, reaching the top of the aneurysm dome, and curling downwards. We also see that the impinging jet is bent slightly towards the left bifurcating vessel. Blood flowing through the right bifurcating vessel was redirected through the aneurysm sac. Similar flow patterns were seen for lower resolutions of this geometry. Finding representative cross-sections of the velocity field is not trivial and requires some effort from the modeller's side. Further development or even automation of finding meaningful representations of the (time-averaged) field requires an iterative process involving feedback of medical experts or possibly novel machine learning efforts.

The oscillatory shear index for the MCA aneurysm is shown in figure 6.2. Similar to the Portugal geometry, this aneurysm shows a few isolated 'hotspots' where the OSI takes on larger values. The PCOM aneurysm had much larger areas with a high OSI. It is important to find out whether such elevated OSI in the PCOM aneurysm might imply an increased rupture risk compared to the MCA aneurysm.

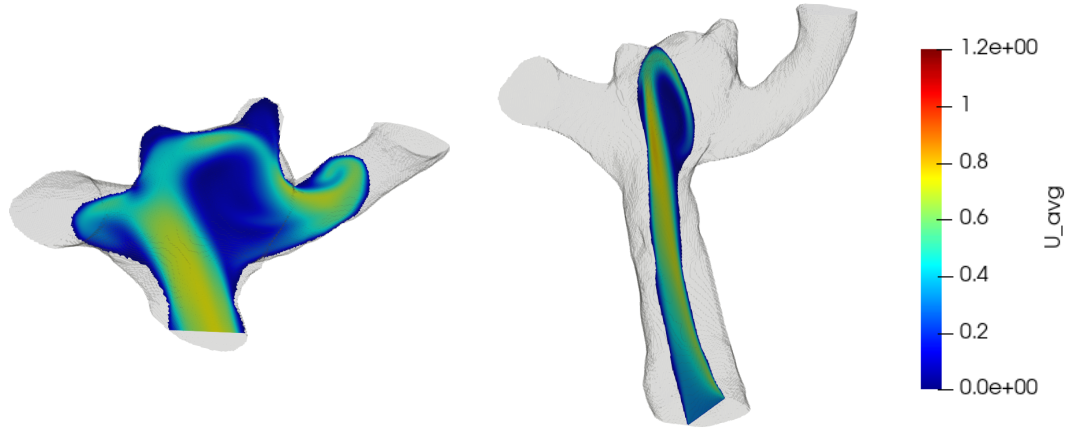


Figure 6.1: Two cross-sections of the time-averaged velocity field, showing the inflow jet and some flow characteristics inside the aneurysm sac.

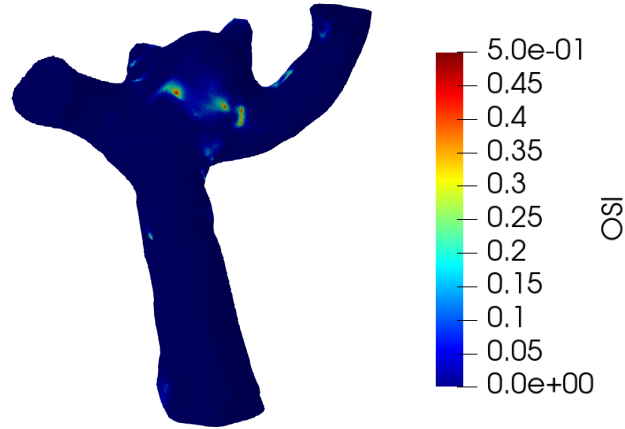
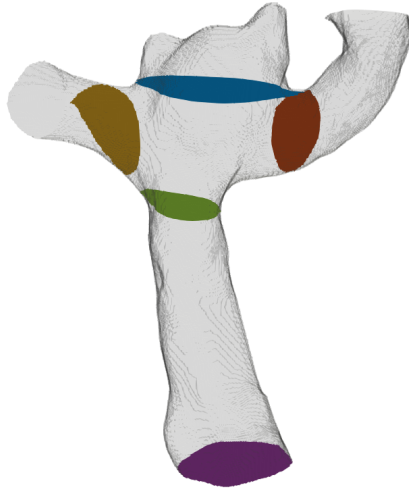


Figure 6.2: Oscillatory shear index for the MCA aneurysm

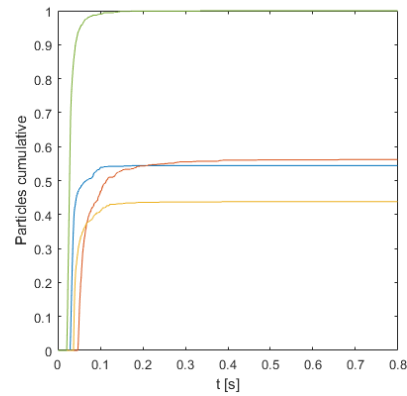
Finally, a virtual bolus has been simulated through this vessel geometry. The MCA aneurysm has been separated into five sections: inlet, junction, aneurysm, left bifurcating vessel and right bifurcating vessel, as shown in figure 6.3a. In total, 54.4% of the particles have visited the aneurysm section of this geometry, with a residence time of 0.021 seconds which is well comparable to the value for the Portugal case. Also, all particles have left the geometry at  $t = 0.8$  s, corresponding to one cardiac cycle. The right bifurcating vessel has a larger mass-flow than the left one, which is shown by the differences in both the live and cumulative visitations of both sections. Moreover, the first particles are present in the right bifurcating vessel slightly later than in the left bifurcating vessel.

Compared to the PCOM aneurysm, the measures of the virtual bolus of this aneurysm differ considerably; in the PCOM case, 89.3% of the particles visited the aneurysm section, and their residence time was 0.68 seconds. In the PCOM geometry, most particles needed two cardiac cycles before leaving the geometry, likely because the majority was delayed inside the aneurysm sac. Also the temporal evolution of the cumulative and instantaneous visitation rates of the two outlets of both geometries show clear differences. For the PCOM case, the yellow and orange lines show a gradual increase, implying the residence times of separate particles inside the PCOM geometry are spread out much more than in the MCA case. In the MCA simulation, these lines show much

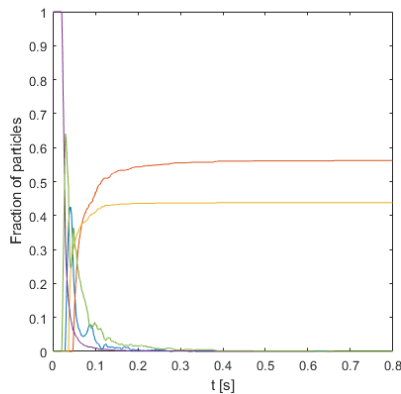
steeper increases, reminiscent of a step-function. This implies there are much smaller variations in the courses of the particles through the total vessel geometry. Consequences of these findings in terms of treatment or rupture risk remain subject to further research.



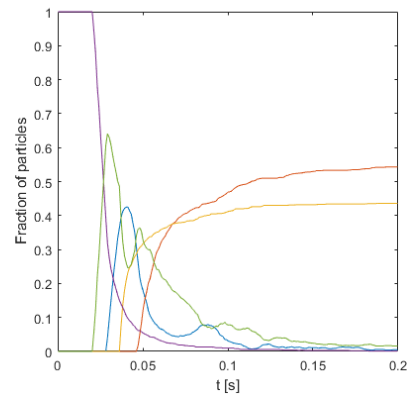
(a) Division of MCA aneurysm in separate sections.



(b) Cumulative visitation rates of the aneurysm, right bifurcating vessel, left bifurcating vessel and connecting piece of vessel. Cumulative visitation rate of inlet is trivial and has hence been omitted.



(c) Instantaneous visitation rates



(d) Zoom of first 0.2 seconds of instantaneous visitation rates

Figure 6.3: Outcomes of the different measures for the virtual bolus for the MCA aneurysm.

Using the assessment information obtained for the MCA case above, we were able to identify qualitative and quantitative differences with the flow inside the PCOM aneurysm, that would remain unnoticed if only the velocity fields in section 3.3 would have been considered. This brings us further ahead in the challenge of successful, patient specific treatment of bifurcation aneurysms. Much more research in terms of virtual treatment, as well as clinical implications of the scores and representations obtained, is necessary and requires close collaboration between clinical experts and mathematical modellers. We hope that the results presented in this thesis, illustrating what CFD can deliver, will stimulate such next steps in the research and yield important innovations to patient-specific decision support as well as optimal treatment closer.

# Bibliography

- [1] Openfoam: User guide, . URL <https://www.openfoam.com/documentation/guides/latest/doc/index.html>.
- [2] Openfoam software, version 20.06, . URL [www.openfoam.org](http://www.openfoam.org).
- [3] Aneurysm - facts, accessed on 20 October 2020. <https://www.ninds.nih.gov/Disorders/Patient-Caregiver-Education/Fact-Sheets/Cerebral-Aneurysms-Fact-Sheet>.
- [4] Surpass evolve flow diverter, accessed on 21 December 2020. <https://www.strykerneurovascular.com/uk/products/hemorrhagic/surpass-evolve-flow-diverter>.
- [5] eclips - medical devices for cerebral aneurysms, accessed on 3 November 2020. URL <https://www.evasc.com/>.
- [6] What are my treatment options?, accessed on 4 June 2020. <http://brainaneurysm.com/what-are-my-treatment-options/>.
- [7] F. Al-Mufti, K. Amuluru, C.D. Gandhi, and C.J. Prestigiacomo. Flow diversion for intracranial aneurysm management: a new standard of care. *Neurotherapeutics*, 13(3):582–589, 2016.
- [8] Y.J. Alderazi, D. Shastri, T. Kass-Hout, C.J. Prestigiacomo, and C.D. Gandhi. Flow diverters for intracranial aneurysms. *Stroke research and treatment*, 2014, 2014.
- [9] N. Bessonov, A. Sequeira, S. Simakov, Y. Vassilevskii, and V. Volpert. Methods of blood flow modelling. *Mathematical modelling of natural phenomena*, 11(1):1–25, 2016.
- [10] L. Boussel, V. Rayz, C. McCulloch, A. Martin, G. Acevedo-Bolton, M. Lawton, R. Higashida, W.S. Smith, W.L. Young, and D. Saloner. Aneurysm growth occurs at region of low wall shear stress: patient-specific correlation of hemodynamics and growth in a longitudinal study. *Stroke*, 39(11):2997–3002, 2008.
- [11] F.A. Braeu, R.C. Aydin, and C.J. Cyron. Anisotropic stiffness and tensional homeostasis induce a natural anisotropy of volumetric growth and remodeling in soft biological tissues. *Biomechanics and modeling in mechanobiology*, 18(2):327–345, 2019.
- [12] R.D. Brown Jr and J.P. Broderick. Unruptured intracranial aneurysms: epidemiology, natural history, management options, and familial screening. *The Lancet Neurology*, 13(4):393–404, 2014.
- [13] L.S. Caretto, A.D. Gosman, S.V. Patankar, and D.B. Spalding. Two calculation procedures for steady, three-dimensional flows with recirculation. In *Proceedings of the third international conference on numerical methods in fluid mechanics*, pages 60–68. Springer, 1973.
- [14] M.A. Castro, C.M. Putman, and J.R. Cebal. Computational fluid dynamics modeling of intracranial aneurysms: effects of parent artery segmentation on intra-aneurysmal hemodynamics. *American Journal of Neuroradiology*, 27(8):1703–1709, 2006.
- [15] J.R. Cebal, M.A. Castro, J.E. Burgess, R.S. Pergolizzi, M.J. Sheridan, and C.M. Putman. Characterization of cerebral aneurysms for assessing risk of rupture by using patient-specific computational hemodynamics models. *American Journal of Neuroradiology*, 26(10):2550–2559, 2005.



- [16] T.E. Darsaut, F. Bing, I. Salazkin, G. Gevry, and J. Raymond. Flow diverters failing to occlude experimental bifurcation or curved sidewall aneurysms: an in vivo study in canines. Journal of neurosurgery, 117(1):37–44, 2012.
- [17] A.M. Gambaruto, J. Janela, A. Moura, and A. Sequeira. Sensitivity of hemodynamics in a patient specific cerebral aneurysm to vascular geometry and blood rheology. Mathematical biosciences and engineering, 8(2):409–423, 2011.
- [18] L. Ghazaryan, D.J. Lopez Penha, S. Stolz, A.K. Kuczaj, and B.J. Geurts. No-slip consistent immersed boundary particle tracking to simulate impaction filtration in porous media. International journal for numerical methods in fluids, 73(7):615–636, 2013.
- [19] K. Golshani, A. Ferrell, A. Zomorodi, T.P. Smith, and G.W. Britz. A review of the management of posterior communicating artery aneurysms in the modern era. Surgical neurology international, 1, 2010.
- [20] I.Q. Grunwald, M. Kamran, R.A. Corkill, A.L. Kühn, I.S. Choi, S. Turnbull, D. Dobson, K. Fassbender, D. Watson, and M.J. Gounis. Simple measurement of aneurysm residual after treatment: the smart scale for evaluation of intracranial aneurysms treated with flow diverters. Acta neurochirurgica, 154(1):21–26, 2012.
- [21] Z. He and Y. Wan. Is fetal-type posterior cerebral artery a risk factor for intracranial aneurysm as analyzed by multislice ct angiography? Experimental and Therapeutic Medicine, 15(1): 838–846, 2018.
- [22] R.I. Issa. Solution of the implicitly discretised fluid flow equations by operator-splitting. Journal of computational physics, 62(1):40–65, 1986.
- [23] H. Jasak. Error analysis and estimation for the finite volume method with applications to fluid flows. 1996.
- [24] L.D. Jou, D.H. Lee, H. Morsi, and M.E. Mawad. Wall shear stress on ruptured and unruptured intracranial aneurysms at the internal carotid artery. American Journal of Neuroradiology, 29(9):1761–1767, 2008.
- [25] M. Kamran, J. Yarnold, I.Q. Grunwald, and J.V. Byrne. Assessment of angiographic outcomes after flow diversion treatment of intracranial aneurysms: a new grading schema. Neuroradiology, 53(7):501–508, 2011.
- [26] M. Korja, H. Lehto, and S. Juvela. Lifelong rupture risk of intracranial aneurysms depends on risk factors: a prospective finnish cohort study. Stroke, 45(7):1958–1963, 2014.
- [27] M. Kroon and G.A. Holzapfel. A model for saccular cerebral aneurysm growth by collagen fibre remodelling. Journal of theoretical biology, 247(4):775–787, 2007.
- [28] W. Kroon, W. Huberts, M. Bosboom, and F. Van De Vosse. A numerical method of reduced complexity for simulating vascular hemodynamics using coupled 0d lumped and 1d wave propagation models. Computational and mathematical methods in medicine, 2012, 2012.
- [29] D.N. Ku, D.P. Giddens, C.K. Zarins, and S. Glagov. Pulsatile flow and atherosclerosis in the human carotid bifurcation. positive correlation between plaque location and low oscillating shear stress. Arteriosclerosis: An Official Journal of the American Heart Association, Inc., 5(3):293–302, 1985.
- [30] A.H. Kuo, P. Nagpal, B.B. Ghoshhajra, and S.S. Hedgire. Vascular magnetic resonance angiography techniques. Cardiovascular Diagnosis and Therapy, 9(Suppl 1):S28, 2019.
- [31] S. Madhavan and E.M.C. Kemmerling. The effect of inlet and outlet boundary conditions in image-based cfd modeling of aortic flow. Biomedical engineering online, 17(1):66, 2018.

- [32] A. Mantha, C. Karmonik, G. Benndorf, C. Strother, and R. Metcalfe. Hemodynamics in a cerebral artery before and after the formation of an aneurysm. American Journal of Neuroradiology, 27(5):1113–1118, 2006.
- [33] M.D. Mazur, P. Taussky, L.M. Shah, B. Winegar, and M.S. Park. Inter-rater reliability of published flow diversion occlusion scales. Journal of neurointerventional surgery, 8(12): 1294–1298, 2016.
- [34] H. Meng, Z. Wang, Y. Hoi, L. Gao, E. Metaxa, D.D. Swartz, and J. Kolega. Complex hemodynamics at the apex of an arterial bifurcation induces vascular remodeling resembling cerebral aneurysm initiation. Stroke, 38(6):1924–1931, 2007.
- [35] H. Meng, V.M. Tutino, J. Xiang, and A. Siddiqui. High wss or low wss? complex interactions of hemodynamics with intracranial aneurysm initiation, growth, and rupture: toward a unifying hypothesis. American Journal of Neuroradiology, 35(7):1254–1262, 2014.
- [36] J. Mikhal. Modeling and simulation of flow in cerebral aneurysms. PhD thesis, University of Twente, Enschede, 2012.
- [37] R. Mittal and G. Iaccarino. Immersed boundary methods. Annu. Rev. Fluid Mech., 37: 239–261, 2005.
- [38] A.J. Molyneux, R.S.C. Kerr, L.M. Yu, M. Clarke, M. Sneade, J.A. Yarnold, P. Sandercock, International Subarachnoid Aneurysm Trial (ISAT) Collaborative Group, et al. International subarachnoid aneurysm trial (isat) of neurosurgical clipping versus endovascular coiling in 2143 patients with ruptured intracranial aneurysms: a randomised comparison of effects on survival, dependency, seizures, rebleeding, subgroups, and aneurysm occlusion. The Lancet, 366(9488):809–817, 2005.
- [39] H.G. Morales, I. Larrabide, A.J. Geers, M.L. Aguilar, and A.F. Frangi. Newtonian and non-newtonian blood flow in coiled cerebral aneurysms. Journal of biomechanics, 46(13):2158–2164, 2013.
- [40] J. Naqvi, K.H. Yap, G. Ahmad, and J. Ghosh. Transcranial doppler ultrasound: a review of the physical principles and major applications in critical care. International journal of vascular medicine, 2013, 2013.
- [41] A.P. Narata, F.S. De Moura, I. Larrabide, C.M. Perrault, F. Patat, R. Bibi, S. Velasco, A.C. Januel, C. Cognard, R. Chapot, et al. The role of hemodynamics in intracranial bifurcation arteries after aneurysm treatment with flow-diverter stents. American Journal of Neuroradiology, 39(2):323–330, 2018.
- [42] M.N. Ngoepe and Y. Ventikos. Computational modelling of clot development in patient-specific cerebral aneurysm cases. Journal of Thrombosis and Haemostasis, 14(2):262–272, 2016.
- [43] H. Nilsson. A look inside icofoam (and pisofoam), Last visited on 21-10-2020. [https://pingpong.chalmers.se/public/pp/public\\_courses/course08331/published/1519801239304/resourceId/4037559/content/UploadedResources/aLookInsideIcoFoam-1.pdf](https://pingpong.chalmers.se/public/pp/public_courses/course08331/published/1519801239304/resourceId/4037559/content/UploadedResources/aLookInsideIcoFoam-1.pdf).
- [44] C.J. O'Kelly, T. Krings, D. Fiorella, and T.R. Marotta. A novel grading scale for the angiographic assessment of intracranial aneurysms treated using flow diverting stents. Interventional Neuroradiology, 16(2):133–137, 2010.
- [45] G.M. Ong. Analysis of flow in stented aneurysm. Master's thesis, University of Twente, 2018.

- [46] E. Oubel, J.R. Cebal, M. De Craene, R. Blanc, J. Blasco, J Macho, C.M. Putman, and A.F. Frangi. Wall motion estimation in intracranial aneurysms. Physiological measurement, 31(9):1119, 2010.
- [47] M.S. Park, M.D. Mazur, K. Moon, M.J. Nanaszko, J.R.W. Kestle, L.M. Shah, B. Winegar, F.C. Albuquerque, P. Taussky, and C.G. McDougall. An outcomes-based grading scale for the evaluation of cerebral aneurysms treated with flow diversion. Journal of neurointerventional surgery, 9(11):1060–1063, 2017.
- [48] D.L. Penn, R.J. Komotar, and E.S. Connolly. Hemodynamic mechanisms underlying cerebral aneurysm pathogenesis. Journal of Clinical Neuroscience, 18(11):1435–1438, 2011.
- [49] D.M.S. Raper, C.J. Chen, J. Kumar, M.Y. Kalani, and M.S. Park. Predicting outcomes for cerebral aneurysms treated with flow diversion: A comparison between 4 grading scales. World neurosurgery, 128:e209–e216, 2019.
- [50] D. Rempfer. On boundary conditions for incompressible navier-stokes problems. 2006.
- [51] D. Roy, Ge. Milot, and J. Raymond. Endovascular treatment of unruptured aneurysms. Stroke, 32(9):1998–2004, 2001.
- [52] M.S. Scher. Developmental origins of cerebrovascular disease i: prenatal cerebrovascular development—classic findings in the context of advances in genetic and fetal surveillance evaluations. Journal of Child Neurology, 27(1):121–131, 2012.
- [53] K. Schneider. Immersed boundary methods for numerical simulation of confined fluid and plasma turbulence in complex geometries: a review. arXiv preprint arXiv:1508.04593, 2015.
- [54] M. Shapiro, T. Becske, D. Sahlein, J. Babb, and P.K. Nelson. Stent-supported aneurysm coiling: a literature survey of treatment and follow-up. American journal of neuroradiology, 33(1):159–163, 2012.
- [55] B. Staarmann, M. Smith, and C.J. Prestigiacomo. Shear stress and aneurysms: a review. Neurosurgical focus, 47(1):E2, 2019.
- [56] A.C.O. Tsang, A.M.Y Fung, F.C.P. Tsang, G.K.K. Leung, R. Lee, and W.M. Lui. Failure of flow diverter treatment of intracranial aneurysms related to the fetal-type posterior communicating artery. Neurointervention, 10(2):60, 2015.
- [57] A.E. Vanrossomme, O.F. Eker, J.P. Thiran, G.P. Courbebaisse, and K.Z. Boudjeltia. Intracranial aneurysms: Wall motion analysis for prediction of rupture. American journal of neuroradiology, 36(10):1796–1802, 2015.
- [58] A.W. Vreman. The projection method for the incompressible navier–stokes equations: the pressure near a no-slip wall. Journal of Computational Physics, 263:353–374, 2014.
- [59] L.N. Williams and R.D. Brown. Management of unruptured intracranial aneurysms. Neurology: Clinical Practice, 3(2):99–108, 2013.
- [60] J. Xiang, S.K. Natarajan, M. Tremmel, D. Ma, J. Mocco, L.N. Hopkins, A.H. Siddiqui, E.I. Levy, and H. Meng. Hemodynamic–morphologic discriminants for intracranial aneurysm rupture. Stroke, 42(1):144–152, 2011.
- [61] L. Zarrinkoob, K. Ambarki, A. Wåhlin, R. Birgander, A. Eklund, and J. Malm. Blood flow distribution in cerebral arteries. Journal of Cerebral Blood Flow & Metabolism, 35(4):648–654, 2015.
- [62] Y. Zhang, L. Jing, Y. Zhang, J. Liu, and X. Yang. Low wall shear stress is associated with the rupture of intracranial aneurysm with known rupture point: case report and literature review. BMC neurology, 16(1):231, 2016.

## Appendix A

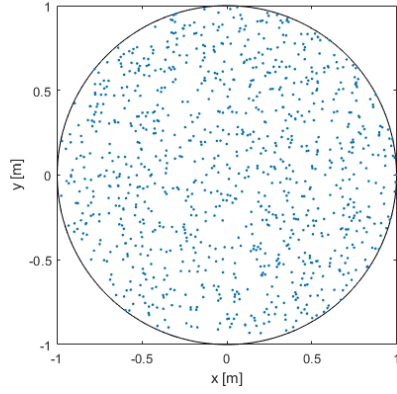
# Validation bolus algorithm analytical Poiseuille

In this test case, we validate the bolus algorithm introduced in section 3.4, for a simple geometry. We investigate the effect of placing the particles slightly from the wall, for a particle simulation through a straight pipe.

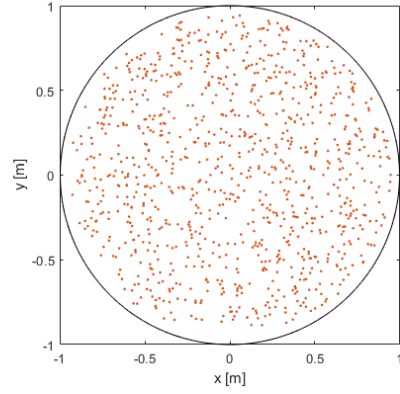
We consider a pipe with a radius of 1 m. The flow in this geometry can be solved analytically from the Navier-Stokes equations, and is known as Poiseuille flow. Flow is directed in the axial direction, and depends only on the radial coordinate:  $U_z(r) = 1 - r^2$ . Hence, the velocity profile is parabolic with a maximum velocity of 1 m/s, occurring at the exact middle of the pipe, as seen in figure A.1c. For this analysis,  $N$  randomly generated, uniformly distributed particles were released simultaneously on the cross-section  $z = 0$  m of the pipe, which is shown in figures A.1b and A.1a. In contrast to the particles in figure A.1a, particles in figure A.1b have not been placed at a very small distance from the wall, making the axial velocity of all particles well non-zero. At  $z = 1$  m, a reference cross section was placed. The fraction of particles passing this section as a function of time will be determined. Since the maximum velocity is 1 m/s, the first particles will arrive at the reference section at  $t = 1$  s. When the particles are released in the cross section with a constant density, the fraction of particles passing the reference plane as a function of time has an analytic solution:

$$P_{pass}(t) = \begin{cases} 0 & t < 1 \\ \min\left(\frac{1-1/t}{r_{cloud}^2}, 1\right) & t \geq 1 \end{cases} \quad (\text{A.1})$$

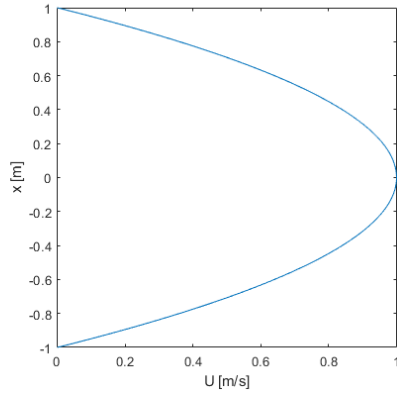
In this formula,  $r_{cloud}$  refers to the radius of the cloud of particles. This is relevant when the particles are placed at a small distance from the wall, where the axial velocity equals 0. If  $r_{cloud} = 1$ , some particles are placed on or very near the wall of the pipe as well. We can see that  $\lim_{t \rightarrow \infty} P_{pass}(t) = 1$ . This is also shown in figure A.1d; in the case  $r_{cloud} = 0.95$  m, all particles passed the reference section at  $t = 10.3$  s, which is consistent with the minimum velocity of  $U_z(0.95) = 0.0975$  m/s. Meanwhile, the blue line corresponding to the case  $r_{cloud} = 1$  m, shows asymptotic behaviour approaching the value of 1. This confirms accurate capturing of the particle motion with our improved algorithm. In order to keep the computing time within reasonable bounds, it appears that one may best avoid placing particles very close to the walls initially.



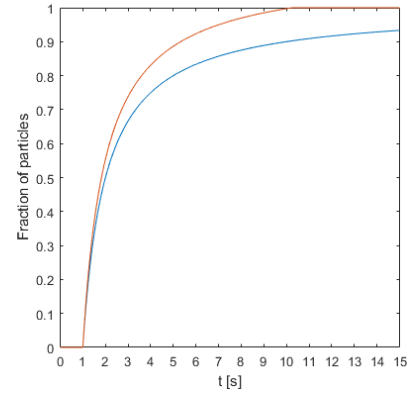
(a) Initial cloud,  $r_{cloud} = 1\text{m}$



(b) Initial cloud,  $r_{cloud} = 0.95\text{m}$



(c) Velocity profile on cross-section  $z = 0$



(d) Fractions of particles passing reference plane

Figure A.1: Particle simulation for analytical Poiseuille flow. (a) and (b) show initial particle clouds at  $z = 0$ . (c) shows the velocity profile over the line  $y = 0$  of the cross-section  $z = 0$ . Fractions of particles passing the reference section at  $z = 1$  for the cases where  $r_{cloud} = 1\text{ m}$  and  $r_{cloud} = 0.95\text{ m}$  are shown in (d).

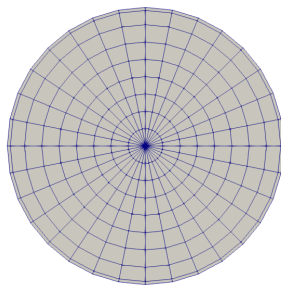
## Appendix B

# Validation bolus algorithm numerical Poiseuille

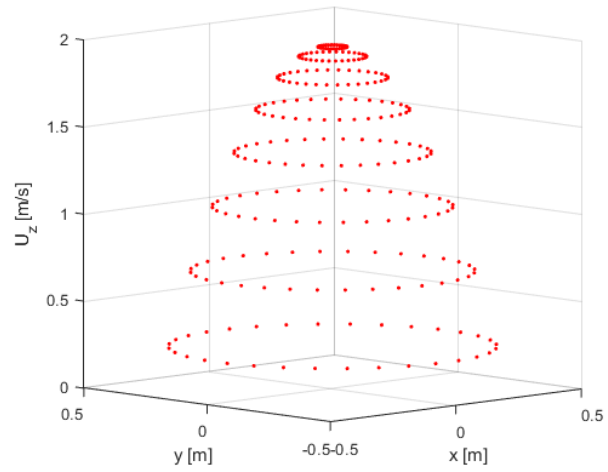
In this section, we investigate the bolus algorithm on the velocity fields resulting from simulation in OpenFOAM in a cylindrical pipe. More specifically, the differences between the two different interpolation methods, piecewise constant and trilinear interpolation, considered in section 3.4 are examined.

Previous analysis of Poiseuille flow, demonstrated in appendix A, was based on the analytical solution. For assessment of the aneurysms, only numerically obtained flow fields will be used. For comparison, the particle simulations for Poiseuille flow have been repeated using velocity fields resulting from two different discretizations, as shown in figures B.1a and B.1c. These two different grids illustrate the differences between the two interpolation methods considered for obtaining the local velocities of the particles. The geometry of the numerical cases differed slightly from the analytical case: the pipe considered here has a radius of 0.5 m, hence the maximum velocity attained at the center of the pipe equals 2 m/s. For consistency, the reference section was placed at  $z = 2$  m. The two discretizations show two big differences: their resolutions and treatment of the center of the pipe. The first discretization divides the domain in both circumferential and radial direction. All cell wedges unite at the center, forming a singularity. This is avoided in the second discretization, where a square was placed around the center. The remaining 'shell' of the cylinder has been partitioned in radial and circumferential directions. Furthermore, the first discretization has a lower resolution than the second one. The resulting velocity fields are depicted in figures B.1b and B.1d. The velocity field of the first discretization shows equal velocities at each 'ring' of cells, while the second grid shows variation. In the first discretization, the cell centres at each ring have the same radial coordinate and therefore equal velocity. In the second discretization, the radial coordinates vary slightly, hence the velocity shows variation.

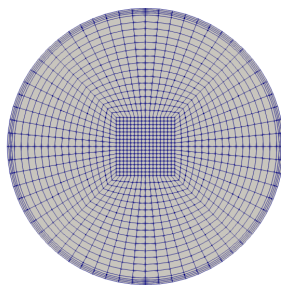
Simulations with a cloud of randomly generated, uniformly distributed particles were done using both trilinear and piecewise constant interpolation to obtain the local velocity. In all simulations,  $r_{cloud} = r = 0.5$  m. The fraction of points passing the reference section as a function of time for both grids and both interpolation methods are seen in figure B.2. Major differences occur between the piecewise constant and tri-linear interpolation simulations of the two discretizations. Since in grid 1, the particles in each ring of cells have equal velocities, the plot corresponding to piecewise constant interpolation has a staircase-like appearance. In grid 2, these steps are spread out, because of variation of the velocities. Moreover, all particles in the piecewise constant interpolation method pass the reference section in grid 1, against 95% in grid 2 within time  $t = 15$  s. A smaller difference is observed for trilinear interpolation of the velocity field between the two underlying grids. The shapes of the curves are alike, and for both grids, 97% of the particles has passed the reference section at  $t = 15$  s. For both grids, it is also shown that trilinear interpolation is more similar to the analytical simulation of particles than piecewise constant interpolation, which follows by comparing these outcomes with figure A.1d. We conclude that particle simulations using trilinear interpolation are more robust against both underlying grid structure as well as resolution.



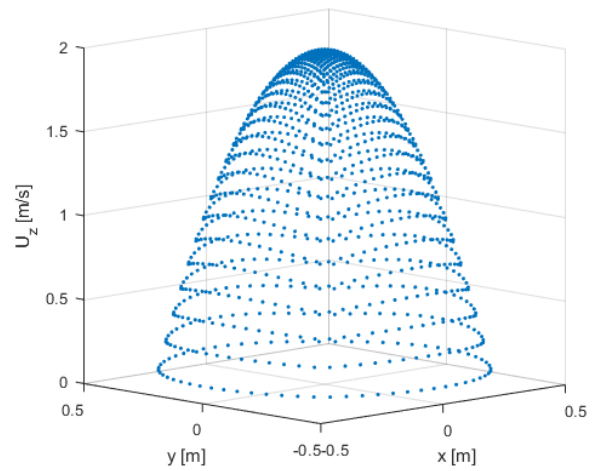
(a) Discretization grid 1



(b) Velocity field grid 1

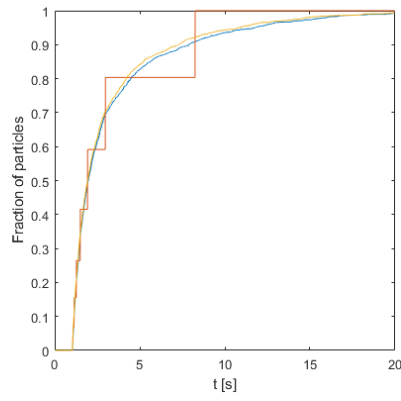


(c) Discretization grid 2

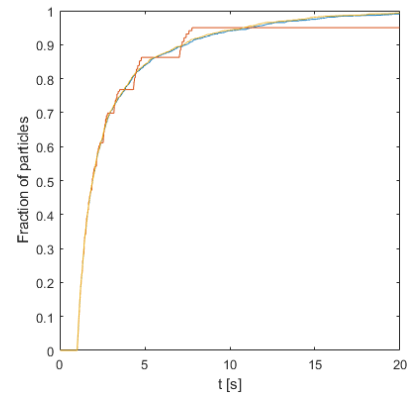


(d) Velocity field grid 2

Figure B.1: Two different discretizations and their fully developed velocities at the centers of the grid cells in a cross section of the pipe.



(a) Grid 1



(b) Grid 2

Figure B.2: Cumulative fractions of particles for the two grids shown in Figure B.1 and different interpolation methods. **Blue: trilinear interpolation**, **orange: piecewise constant interpolation** and **yellow: analytical case**.